Summary of HQ01e magnetic measurements

Version 0c, 11/28/2011 9:57 AM

X. Wang, S. Caspi, D. W. Cheng, D. R. Dietderich, H. Felice, P. Ferracin,
A. Godeke, A. R. Hafalia, J. M. Joseph, J. Lizarazo, M. Marchevsky, and G.L. Sabbi
Lawrence Berkeley National Laboratory
One Cyclotron Road
Berkeley, CA 94720

A. Ghosh, J. Schmalzle and P. Wanderer
Brookhaven National Laboratory
Upton, NY 11973, USA

G. Ambrosio, R. Bossert, G. Chlachidze, J. DiMarco and A. V. Zlobin
Fermi national Accelerator Laboratory
Batavia, IL 60510, USA

A. Milanese and E. Todesco
CERN, CH-1211 Geneva, Switzerland

Abstract

The magnetic measurements of HQ01e, a 1 m long LARP high-gradient quadrupole model, were performed at 4.4 K and above 40 K at the magnet test facility of LBNL in July 2011. The 120 mm aperture cos2θ Nb_3Sn magnet was designed with accelerator magnet features including alignment and field quality. Conductor-limited gradient was 195 T/m at 4.4 K. During the measurement, a ramp rate of 10 A/s was used and measurements at the nominal current of 14.2 kA (82% of short-sample limit with a gradient of 160 T/m) were performed using the 250 mm long printed-circuit board rotating probe developed by FNAL. At 14.2 kA, 2.7 units of b_6 and 0.7 units of b_{10} were measured. Large persistent current contribution and strong dynamic effects were observed.

We analyzed the allowed and non-allowed harmonics obtained during the measurements above 40 K and at the nominal current. Significant change of the skew sextupole occurred between 50 K and 95 K. The allowed multipole and the low-order non-allowed multipoles at the straight section were explained through the rigid displacement of coil blocks with an amplitude less than 100 μm. We also attempted to correlate the coil asymmetry (a_3 and b_3) with the measured coil pole azimuthal strain.

The dynamic multipole measured at the magnetic straight section varied linearly with the ramp rate of magnet current ranging from 10 A/s to 60 A/s. It was attributed to the inter-strand coupling currents with low crossover resistance. The crossover resistance of the cables at the inner layer of the magnet was estimated to range between 0.2 $\mu\Omega$ to 0.7 $\mu\Omega$.

DISCLAIMER

Superconducting Magnet Program report number: SMP-201111-2A

Contents

1 HQ01e magnet

HQ01 is a 1 m long high-gradient quadrupole model magnet developed by the collaboration between BNL, FNAL and LBNL within the LHC Accelerator Research Program (LARP) [Sabbi11]. Detailed magnetic design and parameters of HQ01 are reported in [Felice09, Caspi10]. The design consists of a double-layer cos2θ coil with a 120 mm aperture. Figure 1 shows the cross section of HQ01 magnet viewed from the lead end. The magnet used a keystoned Rutherford cable made of 35 Nb_3Sn strands, each 0.8 mm in diameter. The strands were fabricated using RRP process. The bare cable has a nominal width of 15 mm without any additional material for crossover resistance control. Nominal cable pitch length is 102 mm. Note that for both HQ01d and HQ01e magnets, the cable for coil 5 and 7 was made of RRP 108/127 strand and that for coil 8 and 9 was made of RRP 54/61 strand. The short-sample limit (SSL) at 4.4 K was determined as 17.3 kA, corresponding to a gradient of 195 T/m. Parameters of the superconducting cable used in HQ01d/e magnets are given in Table 1.

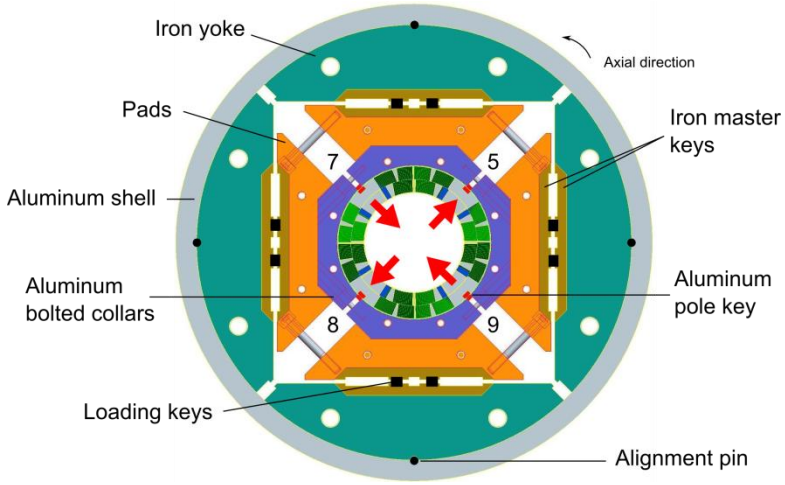

Figure 1 HQ01e cross section viewed from the lead end. The red arrows point to the field direction. Z-axis (axial direction) points from the return to lead end. Axial direction points to the anti-clockwise direction. A normal quadrupole is generated in this case.

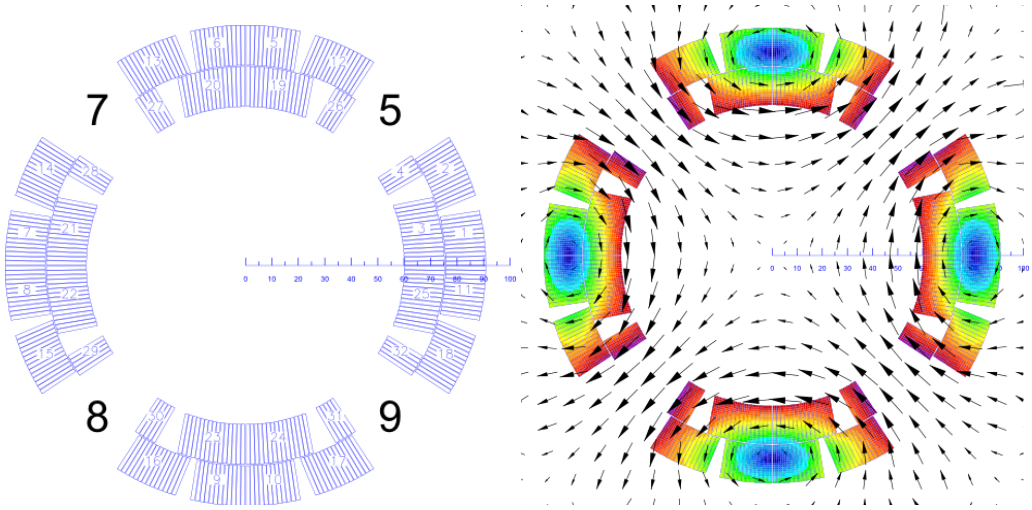

Figure 2 HQ01 magnet. Left: coil blocks. Right: flux lines and flux densities in the coil at 20A.

Table 1 Parameters of the superconducting cables used in HQ01d/e.

Coils in HQ01d/e	8 and 9	5 and 7	
Strand diameter	0.8	0.8	mm
Sub-element number	54/61	108/127	
Sub-element physical diameter	70	50	μm
Cu/Non-Cu ratio	1.06	1.17	
Twist pitch	14 ± 2	14 ± 2	mm
Strand number per cable	35	35	
Cable pitch	102 ± 2	102 ± 2	mm
Bare cable width	15.15	15.15	mm
Keystone angle	0.75	0.75	degree
J_c (12 T, 4.2 K)	3050	2952	A/mm^2

One of the design goals for HQ is to demonstrate accelerator magnet quality, e.g., alignment and field quality. Mechanically, this was achieved by aligning the coil subassembly with respect to the structure subassembly through 4 iron master keys. Within the coil subassembly, 4 Aluminum pole keys, embedded in the outer layer island of each coil, were introduced for coil alignment and field quality. The keys were then clamped by bolted Aluminum collars which in turn were engaged to the iron pads. Four alignment pins were used to align the yoke and Aluminum shell. It was confirmed that the 4 Al pole keys were fully engaged since the assembly of HQ01c [Ferracin11].

In addition to mechanical consideration, the geometry of the Aluminum collar, iron pads and yoke and their positions relative to coil were also optimized to minimize the iron saturation effect on the field harmonics with a reference radius of 40 mm and at 120 T/m [Felice09, Caspi10]. Compensation of the persistent current effect at low field and the field quality at the coil ends will be addressed in future programs.

To increase the preload and reduce its spread from HQ01d, shims of different thickness were introduced in HQ01e during the assembly [Ferracin11]. This may change the field harmonics in HQ01e from HQ01d.

2 Measurement overview

The measurement plan, as part of the magnet test plan, was discussed between the LARP collaboration (BNL, FNAL and LBNL) and CERN [HQ01e_mm_plan]. The main features included:

1. 80% of I_{ss} (14 kA at 4.4 K) was the peak current for magnetic measurement.
2. 10 A/s ramp rate was preferred for all measurements.
3. Precycle with a peak current of 10 kA was used to set the magnet to a known and repeatable state.
4. The 250 mm probe was used primarily and rotating at the center of the magnetic straight section which had about the same length as the probe.
5. Bore field scan at different temperatures were performed during the magnet cooldown and warmup.

More specifically, the following tests were performed.

1. Magnetization measurements. It included a precycle, 20 minute during at the injection level (~ 10.5 T/m), ramp with a peak current up to 14.2 kA. Measurement was performed twice to check the reproducibility.
2. Stair-step measurements to study the DC field error. Again with a precycle, followed by current holding for ~ 3 minutes at even values up to 14 kA.
3. Loop measurements with different ramp rates ranging from 20 A/s to 60 A/s to study the dynamic effect.

The magnet cold test at 4.4 K took 2 weeks with several test goals [Martchevsky11]. The dedicated magnetic measurements (defined as the major test during a test day) took about 5 days. Since it was the first time to perform such extensive magnetic measurements involving extended duration at high current at the magnet test facility, the test system and operation optimized for quench performance study was challenged and nine unexpected system extractions occurred. As a result, the effective measurement time with useful data output was less and the test plan had to be modified during the test. All the magnetic measurements performed were listed in the section 13.

Before the magnetic measurement, two ramp rate quenches, 300 A/s and 100 A/s, were performed, followed by a training quench with a ramp rate of 20 A/s. The quench current was ~ 14.7 kA, based on which the peak current for magnetic measurement was determined to be 14 kA. Due to the accuracy of the power supply system, the actual peak current reached during the magnetic measurement was 14.2 kA, 82% of short-sample limit (I_{ss}), and 96% of maximum quench current of HQ01e (limited effective margin).

3 Experimental setup

HQ01e was vertically positioned in the cryostat with the lead end on the top. Current leads from the header were located close to the pointer "Aluminum shell" in Figure 1. The field direction is illustrated by the red arrows in Figure 1. The 2.3 m long anticryostat with an inner diameter of 49 mm was inserted into the magnet bore before cooldown. The anticryostat was not long enough to allow the measurement at the return end of the magnet. A heater was embedded in the vacuum jacket of the anticryostat to keep its bore temperature above 273 K during the test.

The rotating probe was developed by FNAL. Two coils, one 100 mm long and the other 250 mm long, were installed in the probe. The distance between the coil centers is ~ 250 mm. The radial coils were made of traces on a printed circuit board and more details about this novel design can be found in [DiMarco07]. The radius of the outermost trace is ~ 21.55 mm. Each coil has three voltage outputs, i.e., unbucked (UB), dipole-bucked (DB) and dipole-quadrupole-bucked (DQB) signals, which were amplified by onboard amplifiers inside the probe during the measurement.

The probe was driven by a DC motor through a harmonic drive with a ratio of 100:1. The DC motor has a maximum rotation speed of 3000 rpm. As a result, the probe rotated at a speed of ~ 0.5 Hz. In every revolution, a chain of 4096 quadrature pulses and one index pulse were generated by an incremental encoder mounted at the end of the probe. The probe movement along the bore direction (z) was controlled by a step motor with a resolution of ~ 2 μm [Joseph08].

The following signals were acquired during the measurement, 1) rotating coil voltages, 2) encoder indexes, 3) magnet current, 4) probe temperature and 5) vertical location of the probe. The induced voltages from the rotating coil were connected to the data acquisition system through slip rings. Data was acquired by a hybrid system composed of a dynamic signal acquisition card (National Instruments DSA 4472B), two fast digital integrators (Metrolab FDI 2056), and other auxiliary cards [Hybrid_system]. All three coil voltage signals and the encoder signals were simultaneously acquired by the DSA card. Only the UB and DQB signals were acquired by the FDI cards. The DSA and FDI cards have amplifiers at their input end. The nominal gains used at each amplifier stage are listed in Table 2.

Table 2 Nominal gains for the voltage signals.

Amplifier	UB	DB	DQB
PCB probe	10	10	1000
DSA	1	1	1
FDI	100	n/a	50

The sampling of the DSA card was driven by its internal clock at a frequency of 102.4 kHz. The quadrature signal from the encoder triggered the FDI cards. The same quadrature signal triggered an NI 6221 card acquiring magnet current and probe temperature, synchronizing measurements of field and current. A platinum temperature sensor was attached at the bottom of the probe to monitor the bore temperature. The PXI-based data acquisition system was controlled by a LabWindows/CVI program.

4 Data reduction

The 2D complex bore field at z= $x + iy$ is expanded as

$B_y + iB_x = \sum_{n=1}^{\infty} C_n \left(\frac{x+iy}{R_{ref}}\right)^{n-1}$,

where C_n is the complex multipole coefficients defined at the reference radius R_{ref}. The normalized coefficients c_n reported here is defined as $c_n = b_n + ia_n = 10^4 C_n/B_2$, where B_2 is the main field of the quadrupole magnet with zero main skew component ($A_2 = 0$). Here we use R_{ref} = 40 mm, 80% of the bore radius, for the measurements performed at the magnetic straight section. The reference radius for the reduction of the scan data was 21.55 mm, the outermost trace radius of the PCB probe, as the 2D field distribution was no longer true in the end region. The flux data as a function of angular position used to generate the C_n is a running sum of the flux increments over angular steps of the probe indicated by the encoder quadrature signal [Bottura01]. For the DSA voltage data, the flux increment is obtained by numerically integrating the recorded voltage over the time interval defined by two consecutive quadrature signals from the encoder with the same polarity. For the FDI cards, the flux increments are readily available as the instrument output. Before the normalization, flux drift due to the transport current and voltage associated with the electronics was removed [Bottura01]. The probe centering correction was done based on the first 10 orders of multipole coefficients, assuming the dipole components shown in the recorded UB signal were only due to the probe offset in a quadrupole field.

The angle between the probe and the encoder, e.g., the zero index, was not recorded. As a result, the sign for the odd harmonics is undetermined due to the π/2 ambiguity associated with a quadrupole magnet. The z axis points from the return to lead end.

The reported magnet current for each rotation was an average over the 4096 acquired magnet current data.

5 Measurement above 40 K

Longitudinal scans along the magnet bore (z scan) using the 100 mm PCB probe were performed at different temperatures above 40 K during the cooldown and warmup (see appendix).

At each temperature, the measurement was performed at certain locations along the bore. At each location, 10 measurements were made and the averaged value was reported. The maximum and minimum values of the 10 measurements at each location defined the error bars shown in data plots. At each temperature, the scan of all locations was followed by an identical scan with a reversed current direction but with the same magnitude to reduce the contribution from the residual magnetization of the iron parts in the magnet.

The probe scanned several positions along the bore, moving from the lowest reachable position (towards the return end of the magnet) to the lead end of the magnet and then went back to the lowest position (HQ01e was tested vertically). A schematic showing the relative position of the probe along the magnet bore is shown in Figure 3.

A constant current was applied to the magnet while the probe rotated at certain locations along the bore in the anti-cryostat. The current was measured using a precision shunt (50 mV/100 A) in series with the magnet and a digital multimeter (Keithley 2700). To avoid the possible overheating of the coil during the measurement, power supply voltage (constant current mode), temperatures at certain locations of the magnet (shell, top, bottom), and stress of the coils were monitored continuously. No significant change of these values was observed during the measurement.

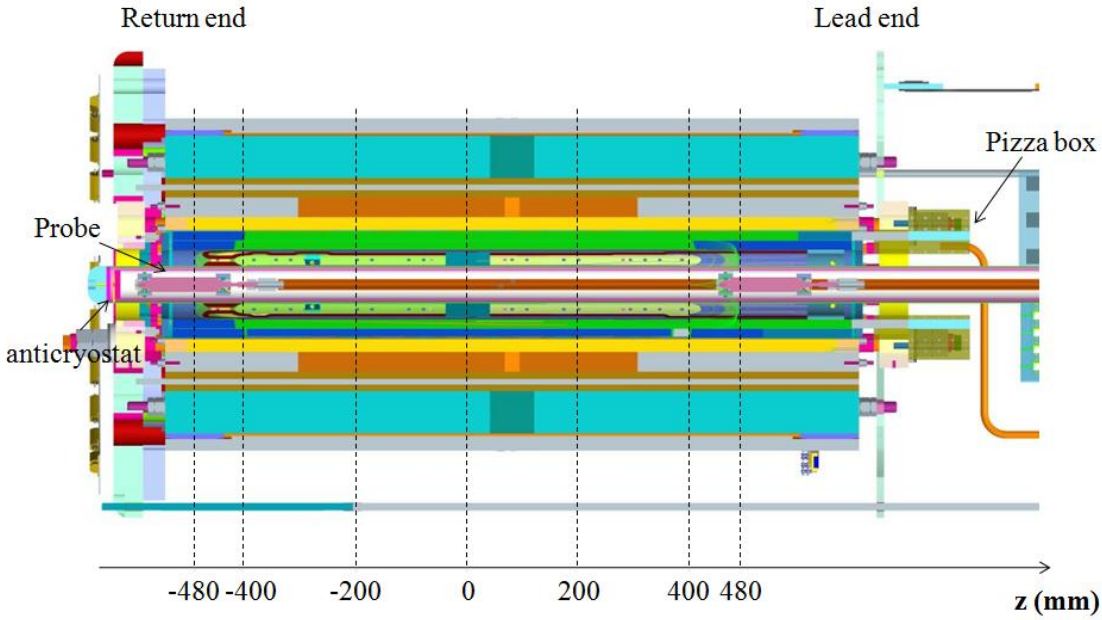

Figure 3 Schematic of the HQ01e coils and the probe position (in scale). Coil end-to-end length is ~ 960 mm. The same coordinate was used for the z-scan. The 100 mm tangential coil instead of the PCB probe was modeled here. The actual magnet was tested vertically (rotating anti-clockwise for 90 degrees).

5.1 Room-temperature measurement before magnet cooldown

In this section, we present the measured harmonics of the assembled magnet at 295 K after loading but before cooldown using the 100 mm probe. Harmonics from the opposite current polarities were averaged. The magnetic straight section is identified based on the measured harmonics profile along the bore. Harmonics from three locations along the straight section were averaged to represent the field quality of the straight section. We try to understand the observed field error by analyzing the systematic error of b_6 (allowed harmonics) and a_3, b_3 (non-allowed harmonics) and reconstructing the possible coil block displacement through the inverse analysis. The random error was neglected due to the limited measurement resolution.

5.1.1 Averaged harmonics along the bore

Before the magnet cooldown, room-temperature measurements were performed along the magnet bore with +/- 15 A. The reference radius was chosen to be 21.55 mm, the radius of the outer most trace of the PCB probe as the scan covered the coil end where 2D field assumption no longer held. The effect of the residual magnetization of the iron parts of the magnet is observed between the difference of the harmonics of positive and negative current as shown in the plots for both the allowed and non-allowed harmonics.

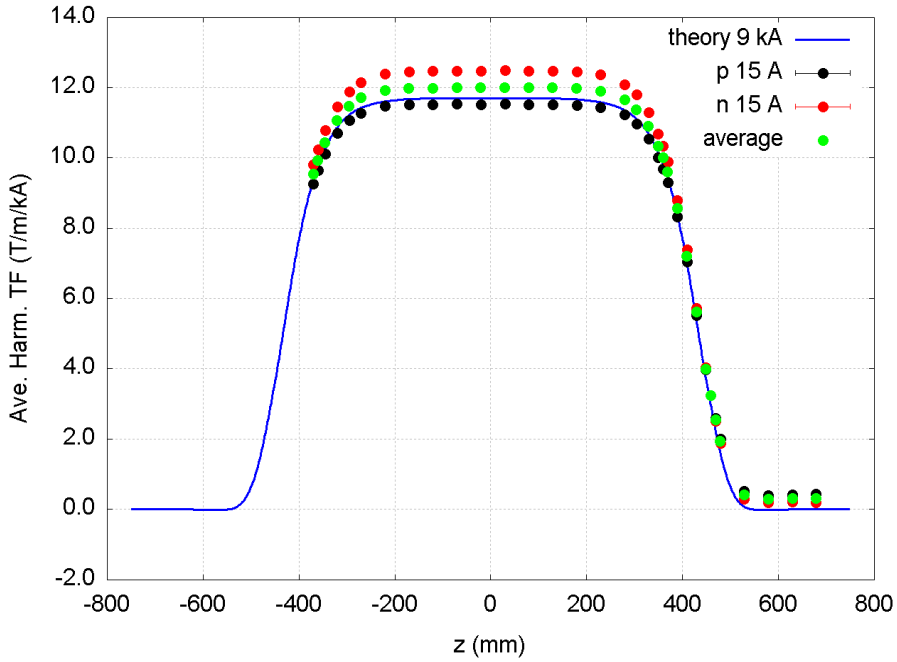

Figure 4 B_2 transfer fucntion measured at +/- 15 A at 295 K, 100 mm probe.

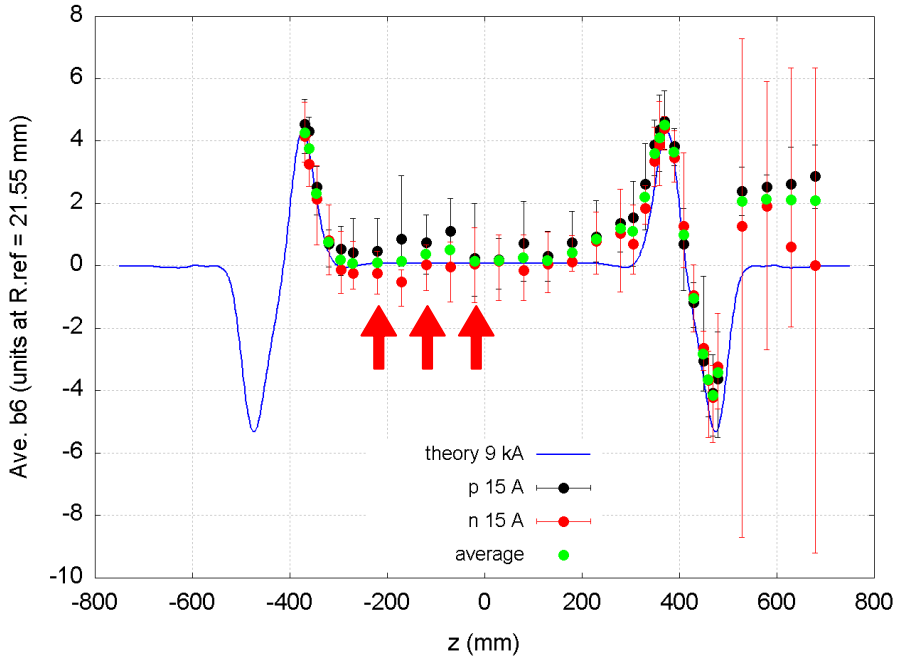

Figure 5 b_6 measured at +/- 15 A at 295 K, 100 mm probe, R.ref = 21.55 mm.

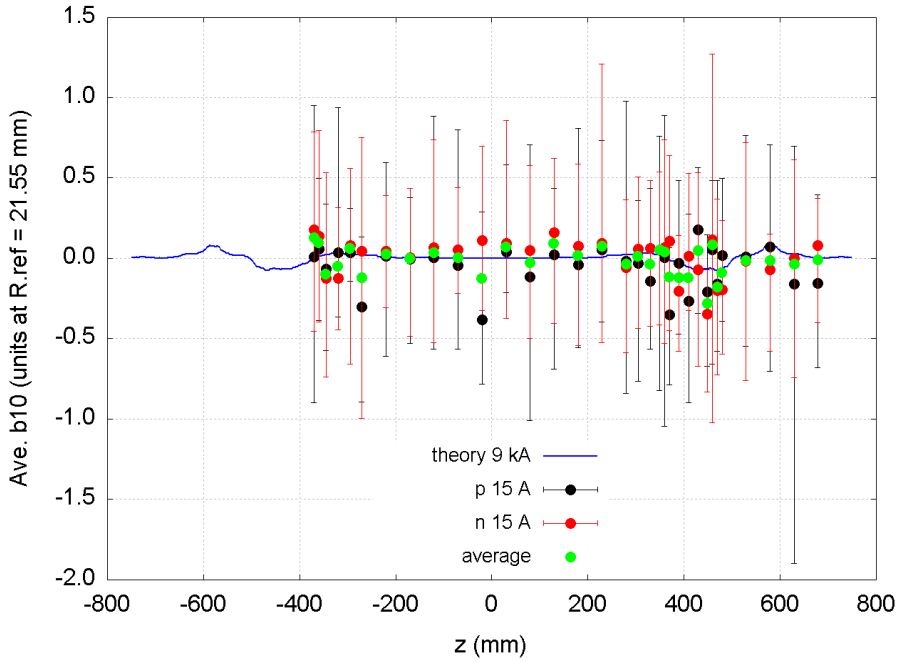

Figure 6 b_{10} measured at +/- 15 A at 295 K, 100 mm probe, R.ref = 21.55 mm.

The averaged b_3, comparing to its counterparts measured with +15 A and –15 A, is shown in Figure 7. Note that b_3 is not the average between the b_3 from two currents but rather the average between b_3 from + 15 A and a_3 from –15A. More details about this are discussed in section 14.

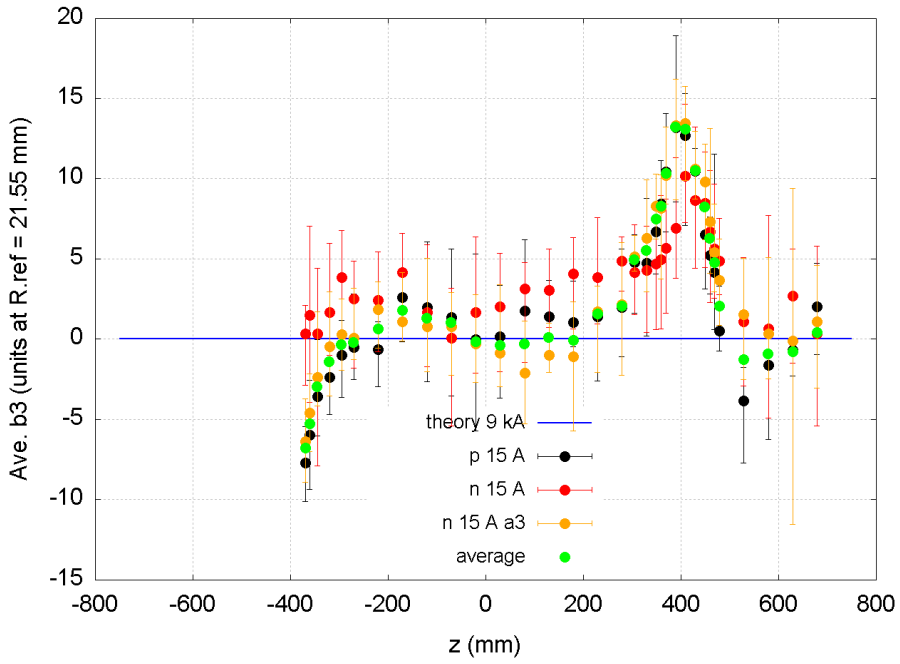

Figure 7 b_3 measured at +/- 15 A, 100 mm probe, R.ref = 21.55 mm. The polarity of the harmonics was reversed to be consistent with the measurements performed at lower temperatures.

The measured allowed harmonics generally agree with the 3D calculation except for b_{10}, the signal noise ratio was not high enough to reveal the details due to the small probe size and the low field signal. Nevertheless, the averaged b_{10} was within -0.3 to 0.1 units at a reference radius of 21.55 mm.

5.1.2 Harmonics of the magnetic straight section

One may determine the magnetic straight section based on Figure 4 and Figure 5 to be between z = -250 mm and 50 mm. In this section, the magnetic field distributes on a 2D plane perpendicular to the bore axis. For this section, we scale the multipole coefficients from a reference radius of 21.55 mm to 40 mm (2/3 of the magnet bore radius).

Three locations, z = -220 mm, -120 mm and 20 mm, were selected, with the interval of 100 mm, same as the probe length (the red arrows in Figure 5). The harmonics averaged between +/- 15 A measurements at three locations are listed in Table 3.

Table 3 Multipoles in unit averaged between +/- 15 A at three locations of the straight section. R.ref = 40 mm.

	-220 mm	-120 mm	-20 mm	average	σ	σ/√N
b3	1.21	2.46	-0.29	1.12	1.38	0.79
b4	-0.85	0.11	0.34	-0.13	0.63	0.36
b5	-1.49	1.09	-0.84	-0.41	1.35	0.78
b6	1.27	4.39	1.65	2.44	1.70	0.98
b7	-3.52	-2.74	0.96	-1.77	2.39	1.38
b8	2.31	4.73	2.88	3.31	1.27	0.73
b9	2.84	3.19	8.04	4.69	2.91	1.68
b10	3.88	5.06	-17.83	-2.96	12.89	7.44

a3	-6.14	-3.41	-4.06	-4.54	1.42	0.82
a4	0.28	0.59	1.38	0.75	0.57	0.33
a5	-1.45	-0.59	-2.64	-1.56	1.03	0.60
a6	-0.28	1.06	-2.37	-0.53	1.73	1.00
a7	-2.23	0.17	0.87	-0.40	1.63	0.94
a8	-4.62	2.82	-1.22	-1.00	3.72	2.15
a9	5.94	-1.72	4.59	2.94	4.09	2.36
a10	19.73	14.19	1.85	11.93	9.15	5.28

One sees that the measured harmonics feature large standard deviation, i.e., large variation between the three locations, especially for harmonics with the order higher than 5. The variation could be resulted from at least two sources, one is the actual coil block variation (intrinsic) between the three locations; the other is due to the small signal/noise ratio of the measurements due to the small size of the probe and the low magnetic field with the limited current. We tend to think the latter is the dominant cause here because the standard deviation tends to: 1) increase with the harmonics order and 2) decrease with higher magnet current for the low-order harmonics.

Thus for the room-temperature data, we focus on the systematic error (averaged harmonics) and neglecting the random error (standard deviation). We try to explain the observed harmonics with possible coil block movements. For the systematic error, we look at b_6 for the allowed harmonics. For the non-allowed harmonics, we check b_3 and a_3 because of their relevant magnitude (> 1 unit) and low standard deviation (< 1 unit).

Since the 295 K measurement was performed after the room-temperature loading, it is useful to first look at the strain gauge results from the end of loading for a possible baseline of coil geometry. Strain gauges were mounted to the inner layer island surface of each coil to measure the azimuthal and axial strain (coordinate defined in Figure 1). Table 4 shows the measured azimuthal strain and the azimuthal stress (with the Poisson effect considered) at the end of room-temperature loading of HQ01e.

Table 4 Measured coil azimuthal strain and processed azimuthal stress at the end of room-temperature loading of HQ01e.

	Coil 9	Coil 8	Coil 7	Coil 5	Average
Azimuthal strain (1E-6)	-436	-398	-456	-496	-446
Azimuthal stress (MPa)	-55	-58	-65	-69	-62

The negative strain at all four coil poles indicated that they were all under compression. The ratio of coil pole strains suggested both the top-bottom and left-right asymmetries occurred in HQ01e after loading and the top-bottom asymmetry was more pronounced than the left-right asymmetry (see section 17 for details). The top-bottom and left-right are defined in the coordinate system shown in Figure 1. This asymmetry induces normal and skew sextupole, consistent with the relevant values of the measured b_3 and a_3.

Following the example in [Redaelli00], the inverse analysis is performed based on the sensitivity matrix for the allowed and non-allowed harmonics as a response to the small rigid displacement of coil blocks that falls into three modes: the change in the coil radius, positioning and

inclination angles. The sensitivity matrix was calculated using ROXIE for the allowed and non-allowed harmonics as shown in section 16.

5.1.3 Inverse analysis for the allowed harmonics

The average -446 micro strain translates into -27 μm decrease of the coil inner radius from its nominal value of 60 mm, assuming all coils were pushed toward the bore while maintaining their shape (a scaled deformation without considering the bending). With all coil radii reducing from their nominal value by -27 μm, the new coil geometry still maintains the quadrupole symmetry (only yielding the allowed harmonics) and gives a b6 of -1.90 units instead of -1.63 unit of the nominal geometry, which is insignificant. The discrepancy between the measured and the expected harmonics are listed in Table 5. The expected values are given by ROXIE with the cable aligned with the outer radius of the layer at 15 A.

Table 5 The measured and expected b6, b3 and a3 at 295 K, 15 A, 100 mm probe, R.ref = 40 mm.

Multipole	Nominal	295 K, 15 A	$\Delta b=b_{meas}-b_{comp}$
b6	-1.90	2.44	4.34
b3	0.00	1.12	1.12
a3	0.00	-4.54	-4.54

We propose two cases to explain the discrepancy of the allowed b_6 harmonics. The first is the error of coil block position with respect to its nominal position, which can be corrected by accurate monitoring and positioning of the coil block during fabrication. The second case assumes the nominal coil block position and attributes the discrepancy to the block displacement during the loading.

For the first case, a rigid radial movement of block 4 for 256 μm is identified based on the sensitivity of the harmonics on the rigid block movement (red arrow in Figure 8). Such large displacement may also push the block 2, which will increase b_6 too. The radial shift of block 4 away from the bore was observed from the cross section of coil 2 (Figure 9).

For the second case, we consider three modes of rigid block displacement (section 16). For the radial block displacement, only block 1 and 3 are considered because the loading compress the coils yielding a smaller coil block radius (brown arrow in Figure 8). From the harmonics sensitivity (Table 44), one sees that only decreasing r1 and/or r3 induces an increasing b6. These two mid-plane coil blocks are also close to the location of the shims, which may justify that loading reduces their radii.

When the coil is pushed toward the bore, the positioning angle of the coil blocks may decrease, i.e., the blocks move toward the mid-plane (black arrow in Figure 8). This is because the Titanium pole island has a higher Young's modulus than that of the coil block. The decreasing positioning angle will induce an increase of b_6 according to the harmonics sensitivity matrix.

The third case is the block tilting, especially in block 3 when loading is applied close to the mid-plane inducing smaller inclination angle in block 3 (green arrow in Figure 8).

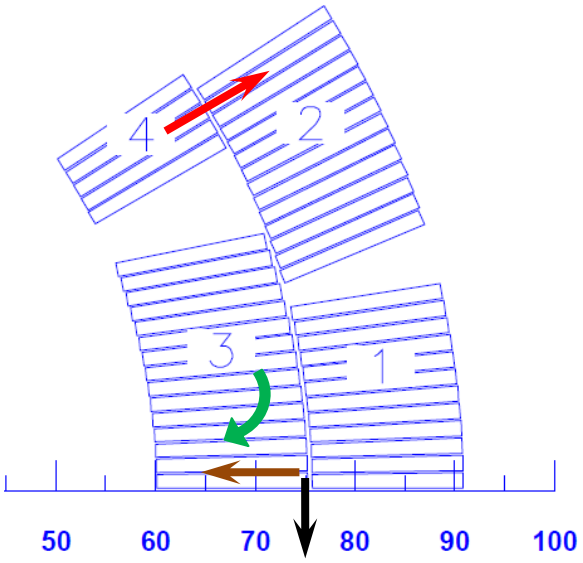

Figure 8 Qualitative representation of two rigid block displacement to explain the measured b6.

The corresponding displacement for each individual movement to induce the observed b6 change is listed in Table 6.

Table 6 Two cases to explain the discrepancy between the measured and expected the allowed b6 (the polarity of the numbers indicate the direction of the displacement).

Case	Displacement during fabrication	Displacement due to the loading		
Mode	Radial	Radial	Positioning angle	Inclination angle
Coil blocks	4	1 and 3	1 and 3	3
Displacement	256 μm	-280 μm	-0.09 degree [1]	-1.27 degree [2]
Arrow color	red	brown	black	green

We note that the actual displacement due to the loading may not be rigid as assumed in the calculation. For example, the radii change in block 1 and 3 can be less as one moving away from the mid-plane. A combination of two or more modes can appear and thus the actual displacement can be less than those listed in Table 6 for each individual displacement mode.

[1] The positioning angle change corresponds to an azimuthal displacement toward the mid-plane of 110 um.
[2] The inclination angle change corresponds to an open angle of 2.54 degrees with the mid-plane as the angel bisector or 0.66 mm of gap between the bottom left corner of the block 3 and its counterpart of the neighboring coil.

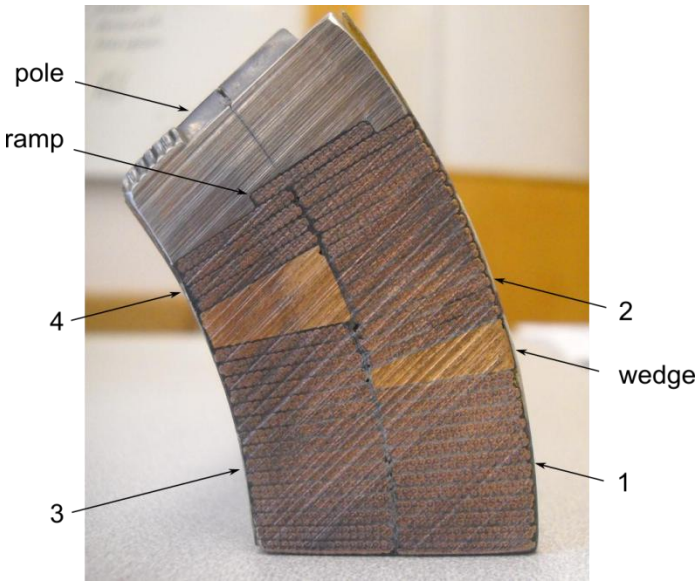

Figure 9 Cross section of the straight section of coil 2 (close to the return end). Numbers refer to the coil block. Block 4 shifted toward the outer layer.

5.1.4 Inverse analysis for the non-allowed harmonics

The non-allowed harmonics can be induced by a certain asymmetry of the coil geometry. We try to correlate the measured harmonics to the possible coil block displacement due to the loading (assuming the same displacement during the fabrication, if any, appears in all four coils and thus only induces the allowed harmonics).

Here we propose two scenarios of block displacement to explain the measured a_3 and b_3. The first scenario assumes the coil maintains the arc shape during the loading. Thus, the negative stress indicates the overall decrease of the radius of the coil and relative slide between the coils at the mid-plane to allow for the different change of the coil radius. The second scenario assumes that the neighboring coils do not slide against each other and coils become convex or concave to comply with the load [Ferracin11a, Ferracin11b].

5.1.4.1 Scenario 1

As shown in section 16.4, each of the 7 orthogonal asymmetry configurations for coil blocks induces a certain group of non-allowed harmonics. The inverse analysis of two non-allowed harmonics can be decomposed into two separate problems with each block displacement vector leading to only one harmonics due to the linear dependence of harmonics to the block displacement. The vector sum of the displacement of each block gives the measured non-allowed harmonics.

For the first scenario, we choose the radial displacement of a block as the positioning and inclination angles will maintain in this case. The radial displacement of block 3 is chosen as it has the largest impact on a_3 and b_3 (Table 49).

The sensitivity is calculated as Δharmonics/Δr in unit/mm (see the sensitivity matrix). The discrepancy between the measured and nominal multipoles then gives the expected displacement. The radial displacement Δr is then applied to each block based on the direction of the

displacement determined by the symmetry configuration (+/-1 in Table 7). The sum of the Δr of each block derived from each harmonics is then summed up for the total Δr of each block (Table 7). Large radial displacement of 40 – 70 μm was observed for the calculated values.

Table 7 Change of r in different symmetry configurations.

	Δ	symmetry	Block #								Sensitivity	Δr
	(unit)		3	19	20	21	22	23	24	25	(unit/mm)	(μm)
a3	-4.54	2	1	1	1	1	-1	-1	-1	-1	78	-58.2
b3	1.12	3	1	1	-1	-1	-1	-1	1	1	-78	-14.4

Table 8 Total radial displacement of each block.

	symmetry	Block #							
		3	19	20	21	22	23	24	25
a3	2	-58.2	-58.2	-58.2	-58.2	58.2	58.2	58.2	58.2
b3	3	-14.4	-14.4	14.4	14.4	14.4	14.4	-14.4	-14.4
	∑ Δr (μm)	-72.6	-72.6	-43.8	-43.8	72.6	72.6	43.8	43.8

Figure 10 illustrates qualitatively the displacement in block 3 and other associated blocks for quadrupolar symmetry. Assuming the initial radius for the inner layer is 59.8984 mm, we have the maximum radius of 59.971 mm in block 22 and 23 given the displacement for each block in Table 8. This corresponds to at least -29 μm less than the nominal value 60 mm to be consistent with the overall negative stress seen at the pole island. Based on the final radii for each block in block group 3, ROXIE gives a_3 = -4.56 units and b_3 = 1.13 units, close to the measured discrepancy. We point out that even though the final radius of each block was used in the ROXIE calculation, the calculated a_3 and b_3 values are sensitive to the displacement but not the initial radius. For example, a calculation with the initial radius of 60 mm for the inner layer and the same displacement as shown in Table 8 gives a_3 = -4.54 units and b_3 = 1.12 units.

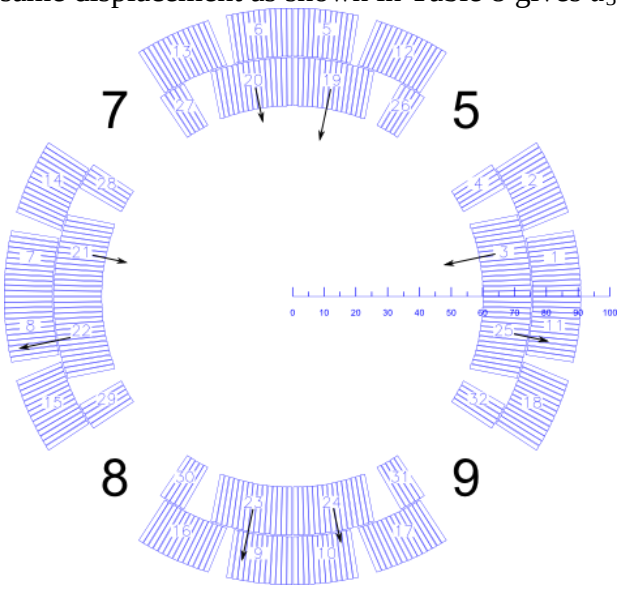

Figure 10 Qualitative radial displacement of block 3 group for the observed b_3 and a_3 in HQ01e at 295 K, 15 A. Measured with 100 mm probe, R.ref = 40 mm.

From Figure 10, one sees that the top two coils, 5 and 7, moves toward the bore inducing higher compression at the inner layer island surface. Large relative displacement (116 μm) occurs at the mid-plane between the top and bottom coils as given by the calculation.

The analysis assumes that the block 3 group was moved only because they induce the harmonics change in the most economic way. It does not necessarily mean that block 3 is the only block that moves. In fact, the sensitivity of the other three block groups (1, 2 and 4) has the same sign as that of block 3, indicating the other block groups can move in the same direction as block 3 to induce the observed harmonics. In this case, the displacement for each block and the relative sliding at the coil interface will decrease as more blocks contribute to the change of the harmonics.

5.1.4.2 Scenario 2

For the second scenario, we focus on the block 2 or 4 as they are away from the mid-plane and may be less affected by the collar during the loading. So when a coil becomes convex or concave, these two blocks displace most. The radial displacement and inclination angle are the two major sources for the observed a_3 and b_3. Block 2 is used as a representative as it has similar or larger sensitivity than block 4 and both blocks affect a_3 and b_3 in the same direction (polarity) as shown by the sensitivity matrix. The radial displacement of the block 2 group shows a similar pattern as seen in scenario 1 (Table 9). Compared to Table 8, larger displacement of block 2 group is observed because block 2 group induces less harmonics with the same displacement.

Table 9 Total radial displacement of each block in the block 2 group.

	symmetry	Block #							
		2	12	13	14	15	16	17	18
a3	2	-173.3	-173.3	-173.3	-173.3	173.3	173.3	173.3	173.3
b3	3	-42.7	-42.7	42.7	42.7	42.7	42.7	-42.7	-42.7
	∑ Δr (μm)	-216.0	-216.0	-130.5	-130.5	216.0	216.0	130.5	130.5

Table 10 shows the inclination angle change in the block 2 group to induce the observed a_3 and b_3. The tilting in coil 5, for example, indicates the coil becomes more convex in the inner layer leading to a higher compression strain (Figure 11). Based on the tilting in the block 2 group, ROXIE gives a_3 = -4.52 units and b_3 = 1.12 units.

Table 10 Inclination angle change of each block in the block 2 group.

	symmetry	Block #							
		2	12	13	14	15	16	17	18
a3	2	-258.0	-258.0	-258.0	-258.0	258.0	258.0	258.0	258.0
b3	3	-63.6	-63.6	63.6	63.6	63.6	63.6	-63.6	-63.6
	∑ Δr (μm)	-321.6	-321.6	-194.3	-194.3	321.6	321.6	194.3	194.3
	Δα (deg)	-2.4008	-2.4008	-1.4506	-1.4506	2.4008	2.4008	1.4506	1.4506
	α (deg)	20.1770	20.1770	21.1272	21.1272	24.9786	24.9786	24.0284	24.0284

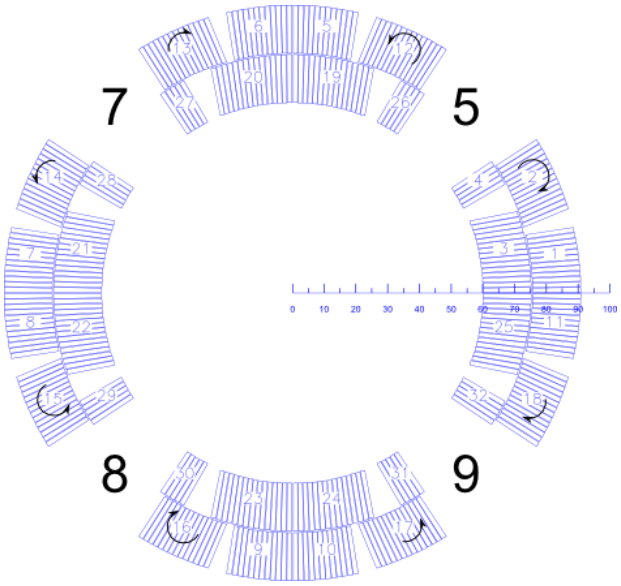

Figure 11 Qualitative radial displacement of block 2 group for the observed b3 and a3 in HQ01e at 295 K, 15 A. Measured with 100 mm probe, R.ref = 40 mm.

We note that for both scenarios, the displacement in each coil is consistent qualitatively with the measured strain in terms of amplitude. Both scenarios can happen at the same time [Ferracin11a, Ferracin11b], which may reduce the large displacement seen in each individual scenario.

5.2 Probe position calibration and position for 4.4 K measurements

By aligning the measured and calculated main field profiles (Figure 4), the relative position (offset) of the probe at its lowest position with respect to the magnet geometric center (z = 0 in Figure 3) was determined. The same offset also aligned the measured and calculated profiles of b_6.

Based on the scanned profile of the B_2 and b_6 along the bore, the magnetic straight section was determined to be within the range of [-175 mm, 25 mm] along the z-axis. This range was for the center of the 100 mm probe and was subject to the z scan step as the spatial resolution. Considering the length of the probe, the corresponding magnetic straight section length ranged from -225 mm to 75 mm, in total 300 mm. The center of the magnetic straight section was at z = -75 mm, where the probe rotated during the following measurement in HQ01e at 4.4 K. We note that the estimation of the magnetic straight section was subject to the step size of the probe during the z scan, which was typically 25 mm for the 100 mm probe. Accordingly, the uncertainty of the estimated range was ±25 mm.

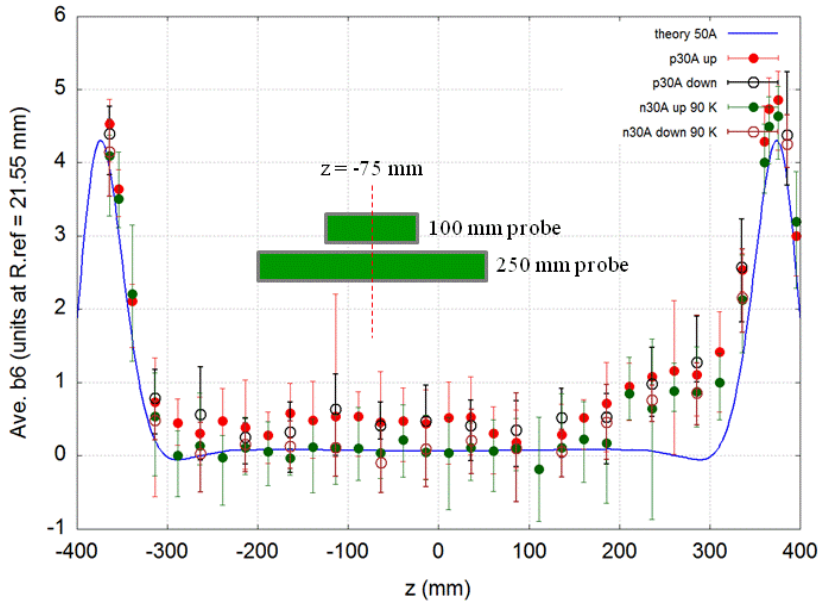

Figure 12 Probe position during the measurement.

The multipole coefficients were normalized to the main field measured at the same probe position when the probe position was fixed at the magnetic center. For the *z* scan measurement, the coefficients were normalized to the maximum main field along the bore.

5.3 Temperature dependence of multipole profiles during the magnet warm-up

Here we present the observation made when the magnet warmed up by natural convection and conduction. Neither magnet current nor cryogen was absent during the warmup. As a result, a more uniform temperature profile along the length of the magnet compared to cooldown was expected. The temperature was averaged between the readings from the thermometers attached to the bottom, shell and top of the magnet. The averaged temperature was expected to be more accurate and close to the actual magnet temperature at higher temperature as the temperature over the entire magnet structure became more uniform during the warmup. Nevertheless, the uncertainty was ± 10 K.

The multipoles presented here were again averaged from the measurements obtained with +/- current polarities (section 14). The temperature increased < 2 K based on the sensors attached to the magnet shell, top and bottom during the scan at 50 K and was less than 1 K at higher measurement temperature due to the increased heat capacity of the magnet and structure. No significant increase in coil azimuthal strain was observed before and after the measurement. Thus, the measurement at each temperature can be considered isothermal.

No significant change in the main field was observed from 50 K to 285 K measured during the warmup (Figure 13). Multipole profiles of b_3 and a_3 of different temperatures from 50 K to 285 K measured during the warmup are shown in Figure 14 and Figure 15, respectively.

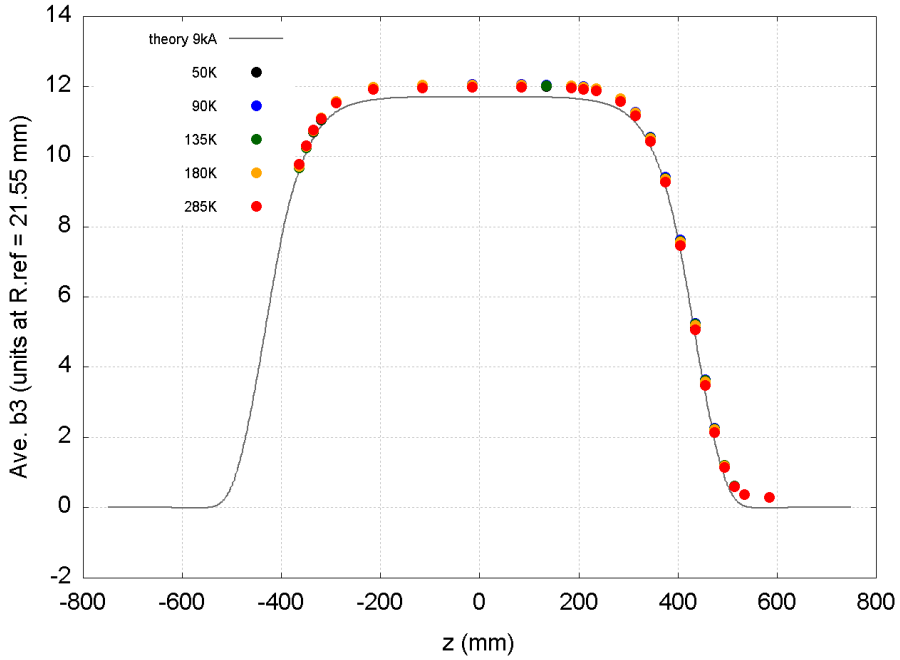

Figure 13 Measured B_2 transfer function along the bore using the 100 mm probe (averaged from the +/- current).

A decrease of ~ 8 units in a_3 was observed when the magnet temperature increased from 50 K to 285 K over the range of -400 mm and 400 mm (Figure 15) with a reference radius of 21.55 mm. Of the 8 units change, 6 units occurred from 50 K to 90 K and the remaining 2 units between 90 K and 285 K. The [-400, 400] mm range was close to the mechanical straight section of the magnet (Figure 3). For z > 400 mm, no significant change in a_3 was observed based on the reduced data. This may be because the probe entered the end region where 3D field distribution appears and the data reduction based on the assumption of a 2D field distribution may not be effective enough to reveal the actual geometry change of the coil. The data presented here does not necessarily indicate that the end region was not sensitive to the thermal contraction/expansion of the Aluminum shell.

While a clear change was observed in a_3, no obvious change was observed for b_3 from 50 K to 285 K except a reduction of ~ 2 units between [0, 200] mm (Figure 15).

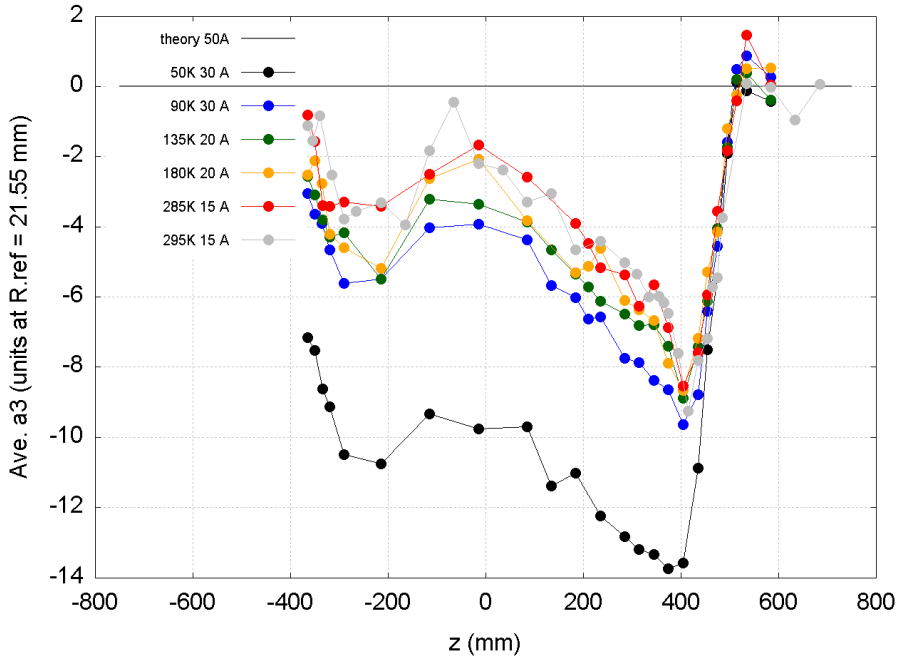

Figure 14 Temperature dependence of a_3 along the bore averaged from the measurements with +/- current. 100 mm probe, R.ref = 21.55 mm.

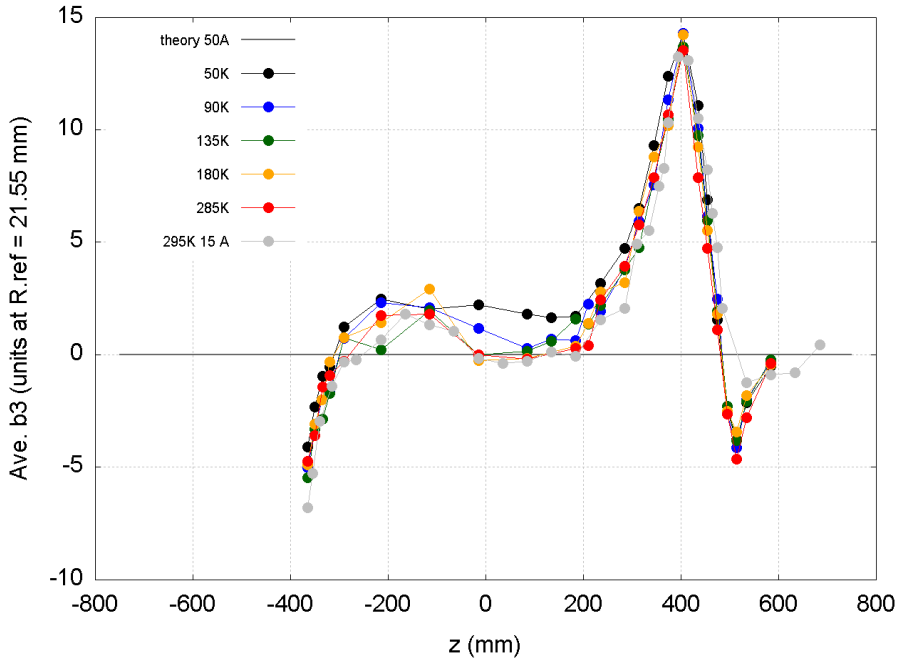

Figure 15 Temperature dependence of b_3 along the bore averaged from the measurements with +/- current. 100 mm probe, R.ref = 21.55 mm.

Now we focus on the behavior of magnetic straight section by studying the harmonics at the following three locations: z = -215 mm, -115 mm and -15 mm with a reference radius of 40 mm (2/3 magnet bore). The harmonics at different temperatures are listed in Table 37 – Table 41. High standard deviation of the harmonics up to a few units, especially for the higher orders (> 4), were observed. Since the signal/noise ratio becomes worse as the multipole amplitude decreases

with the order, we will mainly study the low-order harmonics. The harmonics averaged over three locations are plotted against temperature (Figure 17 and Figure 17). Again, the most significant change due to the temperature was seen in a_3.

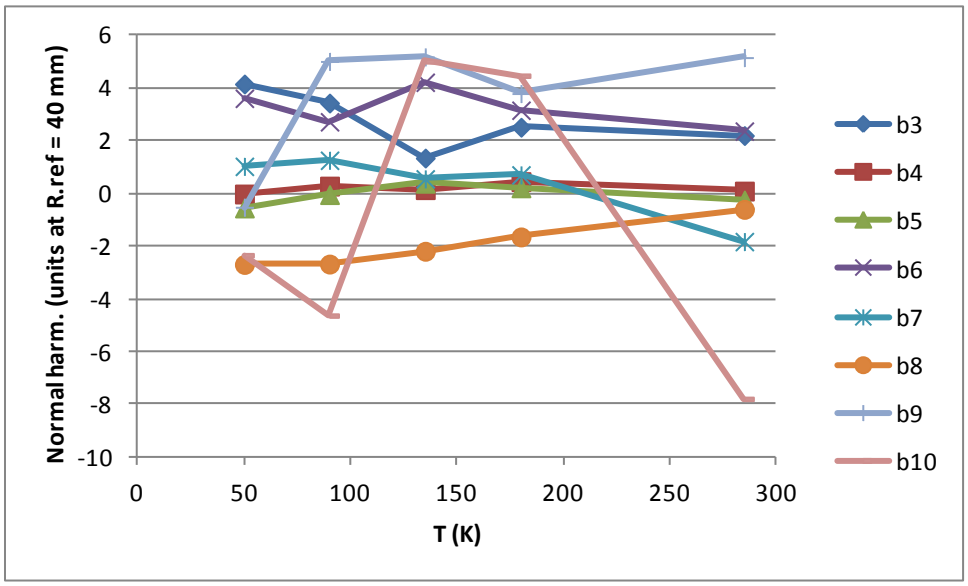

Figure 16 Temperature dependence of normal harmonics averaged at three locations along the magnetic straight section. Measured using the 100 mm probe, R.ref = 40 mm.

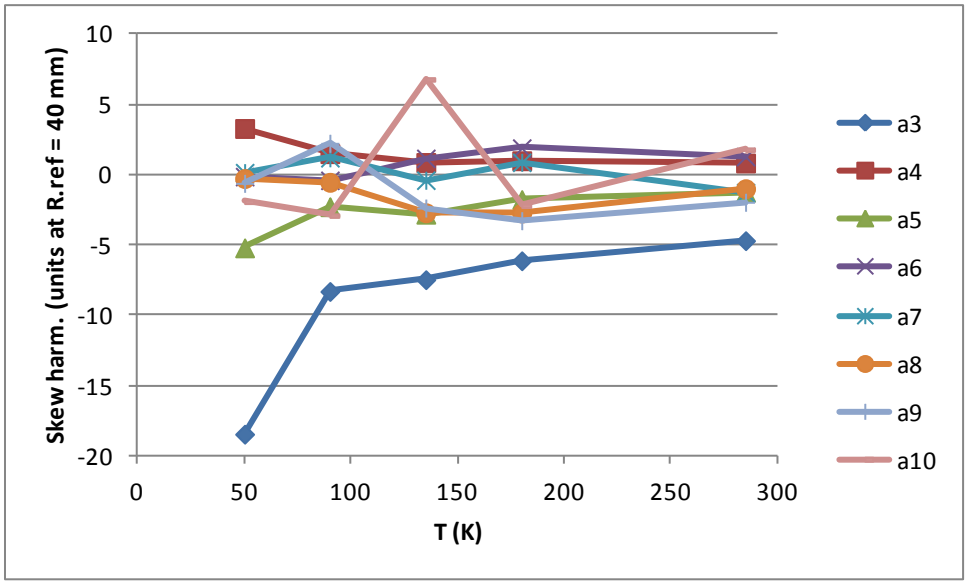

Figure 17 Temperature dependence of skew harmonics averaged at three locations along the magnetic straight section. Measured using the 100 mm probe, R.ref = 40 mm.

The change of a_3 between 50 K and 90 K was ~ 10 units, corresponding to 110 – 150 μm radial displacement of coil block 3 group and 250 μm of relative displacement at the mid-plane between the top (5 and 7) and bottom coils (8 and 9). Compared to the top-bottom asymmetry, the left-right asymmetry was less changed (Δb_3 ~ 2 units) from 50 K to 285 K. The different behavior of a_3 and b_3 indicates the anisotropic coil geometry change during the warmup. We note

that above ~ 18 K, the magnet current flew in the Cu matrix and thus the top/bottom asymmetry due to the different conductor filament size in superconducting state may be negligible. Again, this was measured with a current less than 30 A with limited signal/noise ratio.

5.4 Main field angle along the bore

The temperature dependence of the main field angle [Bottura01] along the bore was shown in Figure 18. At each temperature, the main field angle varies less than 0.7% for z < 400 mm. For z > 400 mm, the probe entered the end region and for z > 480 mm, the probe left the coil region (Figure 3).

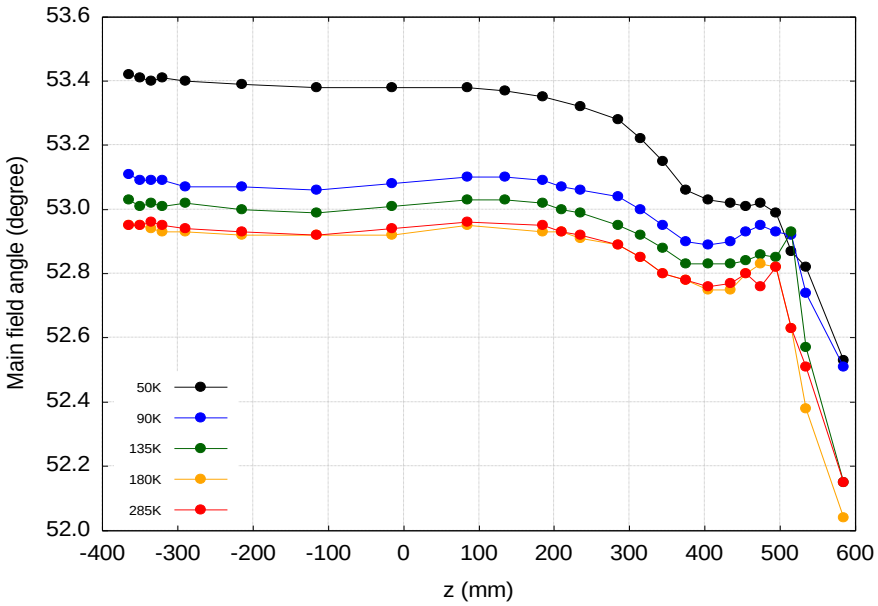

Figure 18 Temperature dependence of the main field angle along the bore.

The main field angles over the straight section (z = -215 mm, -115 mm, and -15 mm) were uniform with a standard deviation of less than 0.01 degrees. Figure 19 shows the temperature dependence of the averaged main field angle (normalized to the value at 50 K) in the straight section. Overall, the angle decreased about 1% from 50 K to 280 K during the warmup. About 60% of the decrease occurred between 50 K and 95 K, consistent with the behavior of the skew sextupole. The main field angle stayed about constant above 180 K.

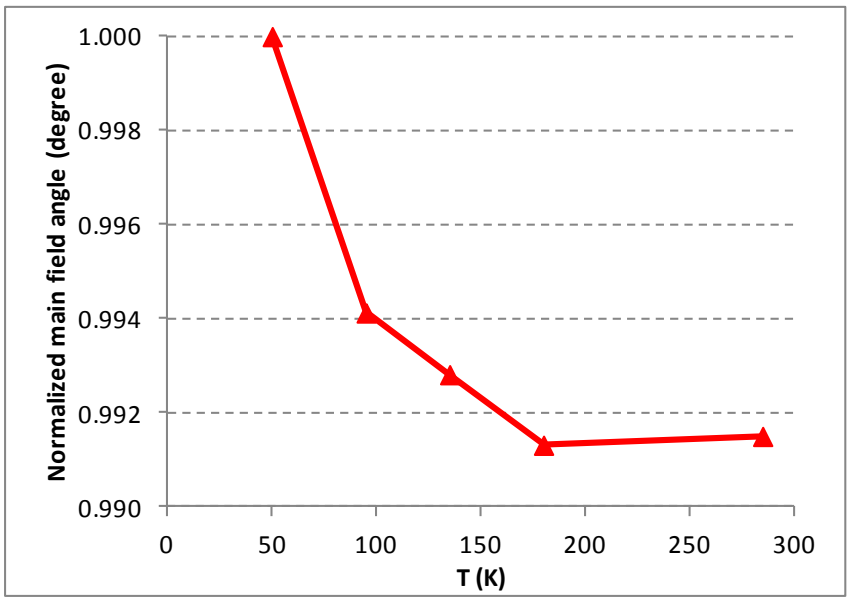

Figure 19 Temperature dependence of the averaged main field angle (normalized to the value at 50 K) at the straight section.

5.5 Multipoles of the magnetic straight section before and after the cold test

We compare the multipoles measured at 295 K before the cooldown and those measured at ~285 K during the warmup. Both measurements were performed with +/- 15 A and the multipoles were averaged from two current polarities. The normal and skew harmonics averaged from the three locations at the magnetic straight section, z = -220/-215 mm, -120/-115 mm and -20/-15 mm, were plotted in Figure 20 and Figure 21.

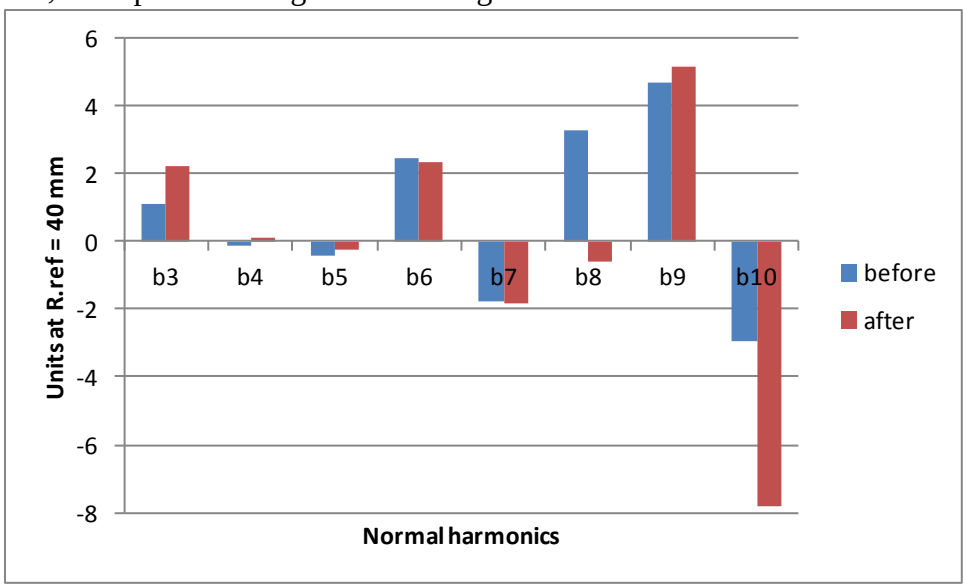

Figure 20 Normal harmonics before (295 K) and after the test (285 K). Averaged from +/- 15 A measurements with the 100 mm probe, R.ref = 40 mm.

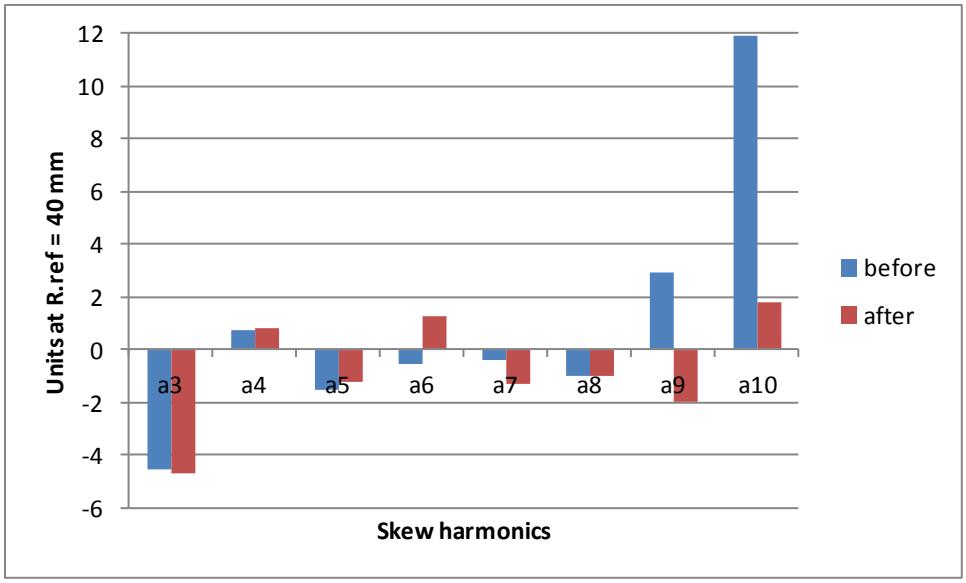

Figure 21 Skew harmonics before (295 K) and after the test (285 K). Averaged from +/- 15 A measurements with the 100 mm probe, R.ref = 40 mm.

In general, good agreement were found between the normal harmonics with orders lower than 8 and skew harmonics with order lower than 6. The normal sextupole almost doubled after the cold test while the skew sextupole remained the same. This may indicate the left-right asymmetry enhanced between two measurements while the top-bottom asymmetry remained at the same degree. On the other hand, the allowed b6 remained the same. For high-order harmonics, e.g., order > 8, the signal noise ratio may not be high enough to yield reliable data comparison.

Table 11 compared the azimuthal strain at the coil poles before and the after the cold test. The distance to symmetry (section 17), was also included for both measurements. We see both the left-right and top-bottom asymmetries enhanced after the test according to their larger distances to the symmetry. However, compared to the top-bottom asymmetry, the larger distance to the left-right symmetry was in contrast to the observed lower b_3 (compared to a_3) after the test. The error in strain gauge reading of coil 8 cannot be excluded [Ferracin11b].

Table 11 Measured coil pole azimuthal strain before and after the cold test at room temperature.

Azimuthal strain (1E-6)	Coil 9	Coil 8	Coil 7	Coil 5	Distance to symmetry	
					Left-right	Top-bottom
Before	-436	-398	-456	-496	0.12	0.19
After	-460	-341	-443	-465	0.30	0.26

Relevant a_3 can still be induced with a relative uniform loading in terms of azimuthal coil stress. It became higher during the cooldown but became negligible at nominal current.

6 Magnetization measurement at 4.4 K

6.1 5 kA Feasibility test

CERN suggested the magnet ramping rate be fixed at 10 A/s for the magnetization measurement as the same ramp rate is used at LHC. The feasibility had to be confirmed first as 10 A/s was not typically used to start the ramp at the test facility at LBNL. Flux jumps during the ramping, especially when I < ~ 8 kA, can result in transient coil imbalance voltage signals with an amplitude of the order of up to a few volts. As a result, quench detection schemes based on the filtered imbalance signals with a certain threshold can still trigger, leading to the same system response as a magnet quench occurred, e.g., protection heater firing, power supply retreat, magnet current decay and energy extraction. On the other hand, at the current level where flux jumps were active (~ 50% I_{ss}), conductor margin usually is high enough to keep the magnet from quenching. This is confirmed by analyzing the data captured during these flux-jump-triggered extraction events – the coil voltage signal usually recovered and the magnet was not quenching after the transient flux jump.

These observations suggest that one may raise the quench detection threshold settings when current is low and the flux jump is active to avoid the flux-jump-induced extraction during a test, which takes time to recover. A current profile including the associated quench detection settings was setup to investigate the feasibility of 10 A/s from 50 A to 5 kA (Figure 22). The threshold of F2-OV, monitoring the magnet terminal voltage, was set to 1 V when ramping at 10 A/s and 5.6 V when ramping at 50 A/s. F2-imbalance was set to 5 V all the time. F1-imbalance, the most sensitive one to the flux jumps, was set to 1 V. Note that 1 V is the maximum level that can be set for F1-imbalance. Two tests, cycle 1 and cycle 2, were completed without any flux-jump-triggered extraction.

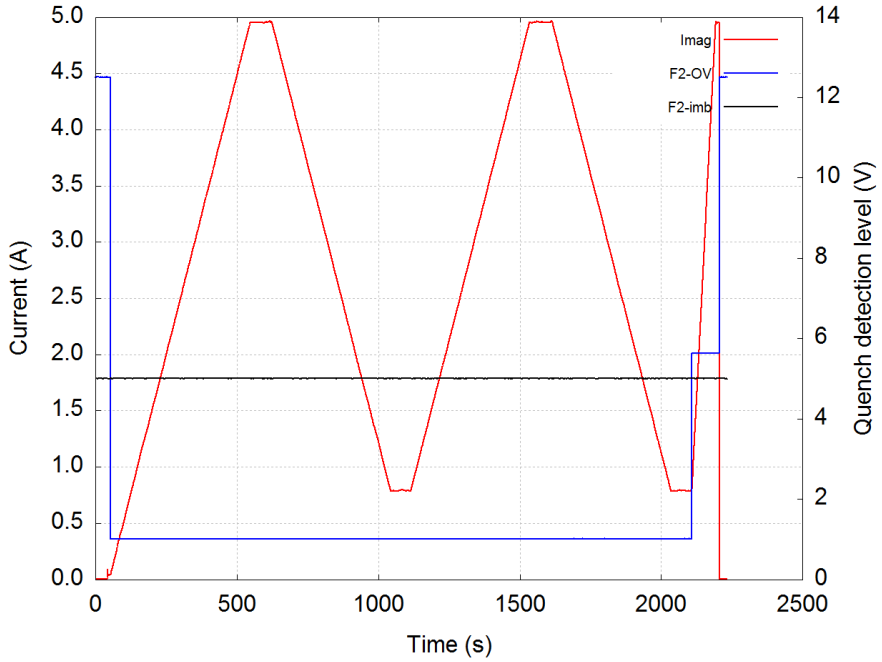

Figure 22 Current (primary y-axis) and quench detection levels (secondary y-axis) as a function of time for the 5 kA feasibility test (cycle 1 and cycle 2). F1-imb was set to 1 V all the time.

6.1.1 Comparison between DSA and FDI

In cycle 2 measurement, the hybrid DAQ system was used to check the agreement between the DSA and FDI data. In addition to the onboard amplifier in the probe, DQB signal was amplified with a gain of 10 by FDI.

Figure 23 compares the transfer function between the FDI data (points) and DSA data (lines). The data was reduced from the measurement of cycle 2. B_2 amplitude was from the UB signal as there were only two FDI cards and the DB signal was not recorded.

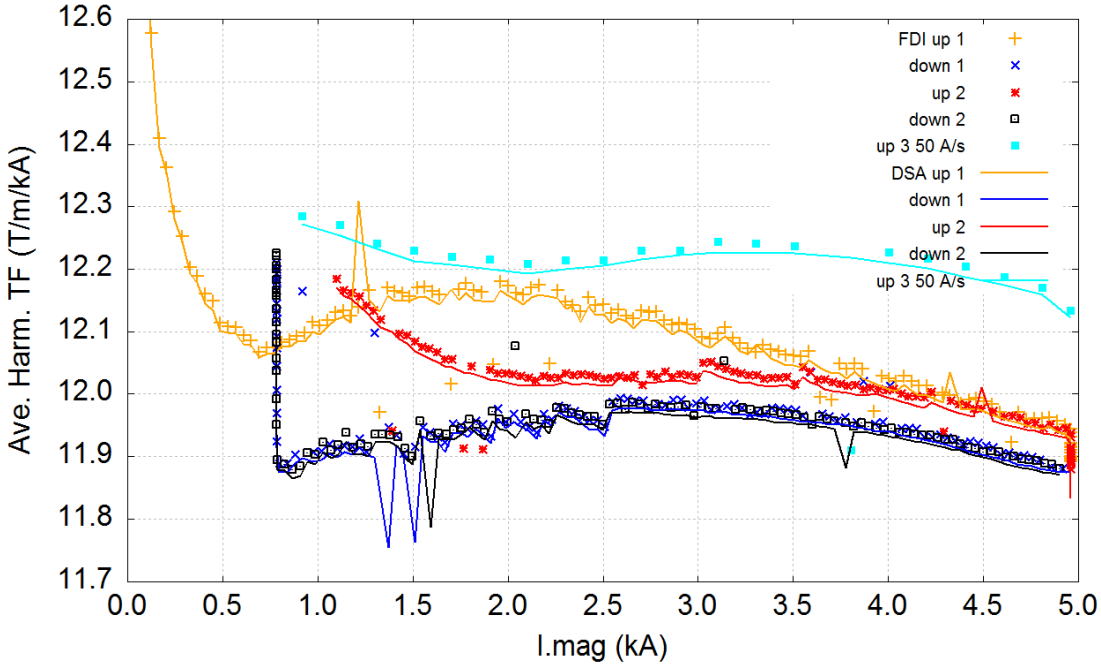

Figure 23 B_2 transfer function comparison between the DSA data and FDI data. Cycle 2. R.ref = 40 mm.

The transfer functions from both acquisition cards generally agree with each other with a few fluctuations. The FDI data was systematically higher than that of DSA for ~ 0.1%. This was related to the FDI card acquiring the UB signal and/or the gain used for this FDI card because the agreement between the multipole coefficients for the same order between the FDI card acquiring the DQB signal and the DSA was better (Figure 24). It is concluded that the FDI and DSA yielded similar harmonics results.

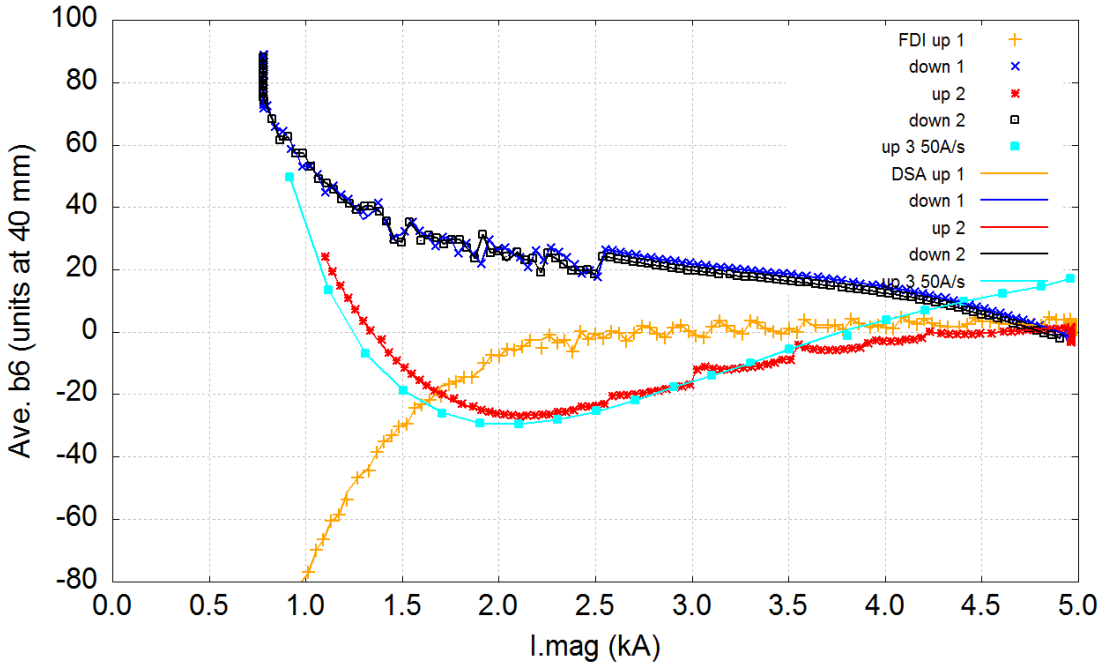

Figure 24 b6. FDI vs. DSA. Cycle 2. R.ref = 40 mm.

6.2 14 kA measurement, 250 mm probe

A current profile for the magnetization measurement up to 14 kA is shown in Figure 25. It consists of the following four stages.

1. Pre-cycle. Ramp from 50 A to 10 kA at 10 A/s. Hold for 1 minute at 10 kA. Ramp down to 800 A at -10 A/s and hold for 1 minute.
2. Measurement cycle #1. Simulated injection: ramp from 800 A to 880 A at 10 A/s and hold for 20 minutes. Ramp to 14 kA at 10 A/s and hold for 1 minute. Ramp down to 800 A at -10 A/s and hold for 1 minute. 880 A corresponds to 10.7 T/m for the injection. (10 T/m = 195 [T/m] * 80% * 760 [A] / 11850 [A])
3. Measurement cycle #2. Repeat measurement cycle #1 for data reproducibility.
4. Cleansing quench. Ramp from 800 A to 5 kA at 50 A/s. Hold at 5 kA and provoke a quench. It has been observed that after a provoked quench for HQ at 3 kA, a multipole waveform still existed, indicating that the provoked quench at 3 kA with the protection heater (with the set voltage of 300 V) was not high enough to remove the persistent current.

The current values quoted above were set values in the power supply control file. Actual current levels varied slightly due to the accuracy of the power supply and its control system. ***

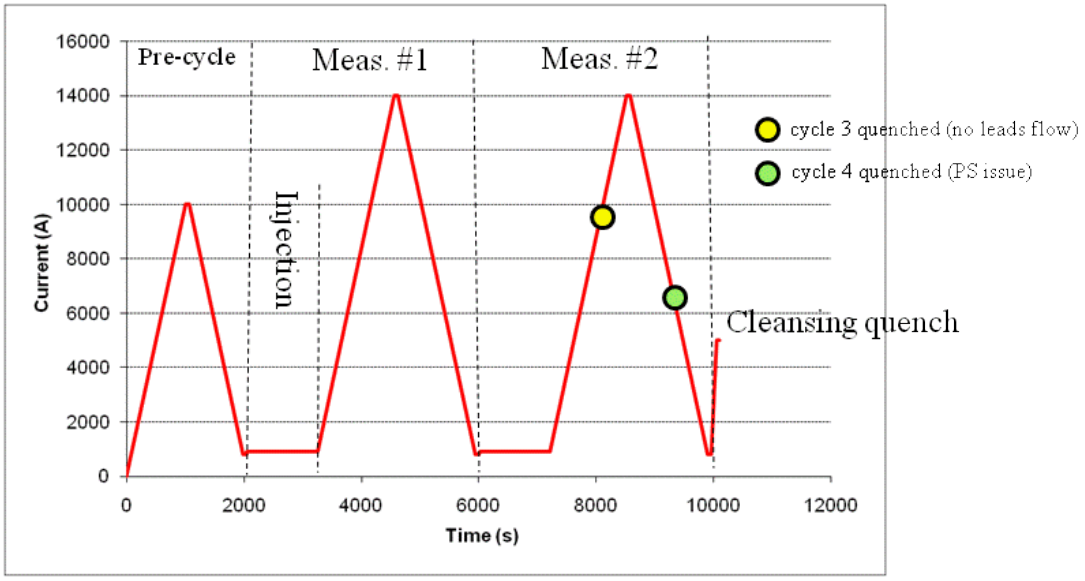

Figure 25 Current profile for the magnetization measurement.

The quench detection level decreased from their initial values with increasing magnet current (Figure 26) when it was above 10 kA. The initial values below 10 kA were found to be high enough to be insensitive to the flux jump. Meanwhile, a quench can still be detected with these settings within typically 100 ms, lead to a maximum and acceptable 10 MIITs for HQ01e. As the current was above 10 kA, flux jumps were less active and the thresholds were reduced to detect a quench as quickly as possible.

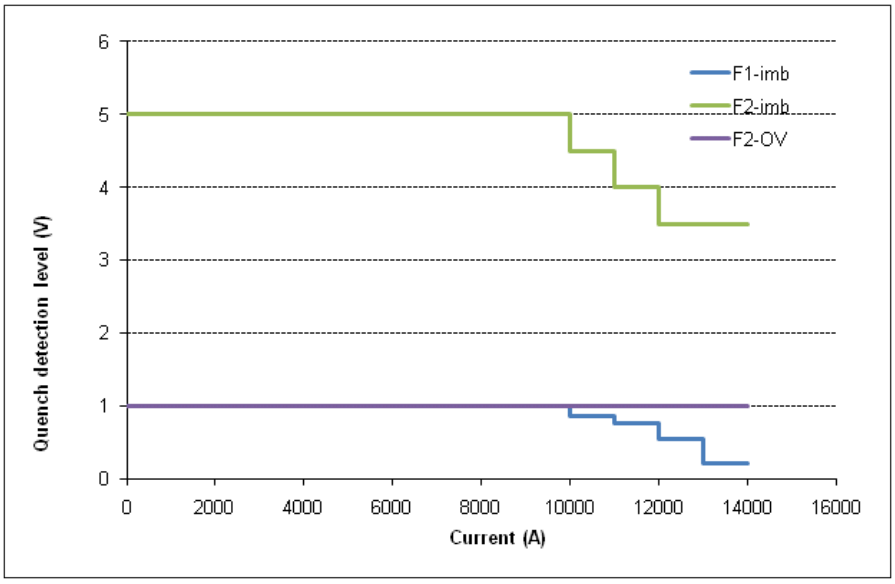

Figure 26 Quench detection level settings during the magnetization measurement.

Two measurements, cycle 3 and cycle 4, were performed but the planned profile was not completed due to the unexpected provoked quenches. Cycle 3 quenched at ~ 9 kA during the second up ramp to 14 kA due to the current leads flow failure. Then cycle 4 measurement was started and quenched at ~ 6 kA during the second down ramp to 800 A due to the power supply system issue.

6.2.1 Current dependence of multipoles

6.2.1.1 Main field transfer function

B_2 transfer functions from two measurements, cycle 3 and cycle 4 using the 250 mm probe, were compared in Figure 27. The iron components in the magnet started saturation at ~ 3 kA.

To investigate the reproducibility of the main component of the bore field (B_2) between cycle 3 and cycle 4, we define b_2 as [Bellesia04]

$$b_2 = \frac{\mathrm{TF_{meas}} - \mathrm{TF_{nom}}}{\mathrm{TF_{nom}}} 10^4,$$

where TF is the transfer function and $\mathrm{TF_{nom}}$ = 12.304 T/m/kA at the injection level. Figure 28 - Figure 30 compare the b_2 from two measurements at different current levels, respectively. At low current levels (0 – 5 kA), spikes with an amplitude of ~ 20 units were observed during the up ramp. These spikes are not completely repeatable in terms of the amplitude and the current level where they occurred. They corresponded to the rise-and-decay signals seen in the other multipoles. At high current levels (13 – 14 kA), the difference between two measurements was ~ 3 units. For current levels in between, the difference was ~ 3 units. This indicates that HQ01e met the target of 0.01% - 0.03% reproducibility, especially for high current.

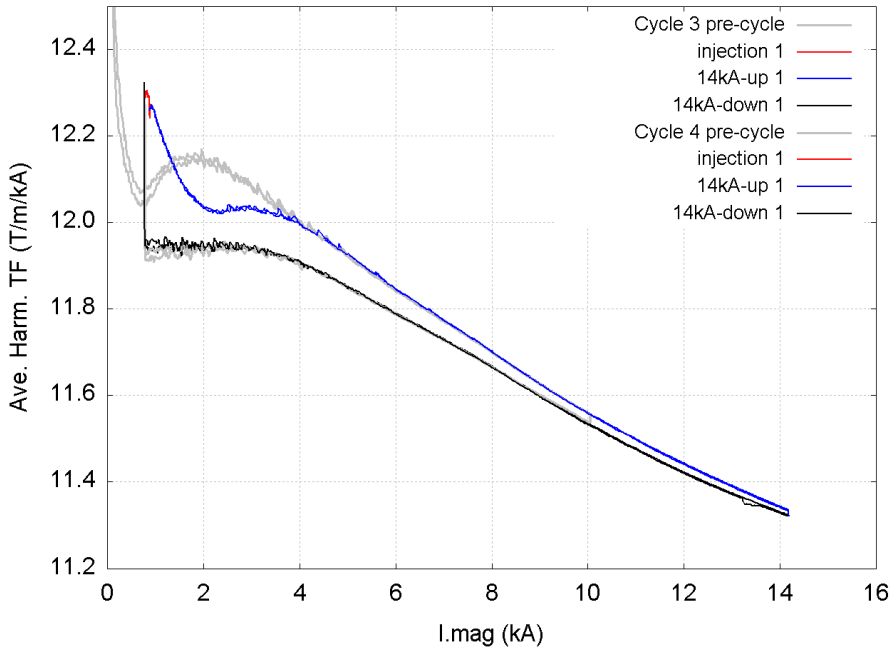

Figure 27 B_2 transfer function from measurements, cycle 3 and cycle 4.

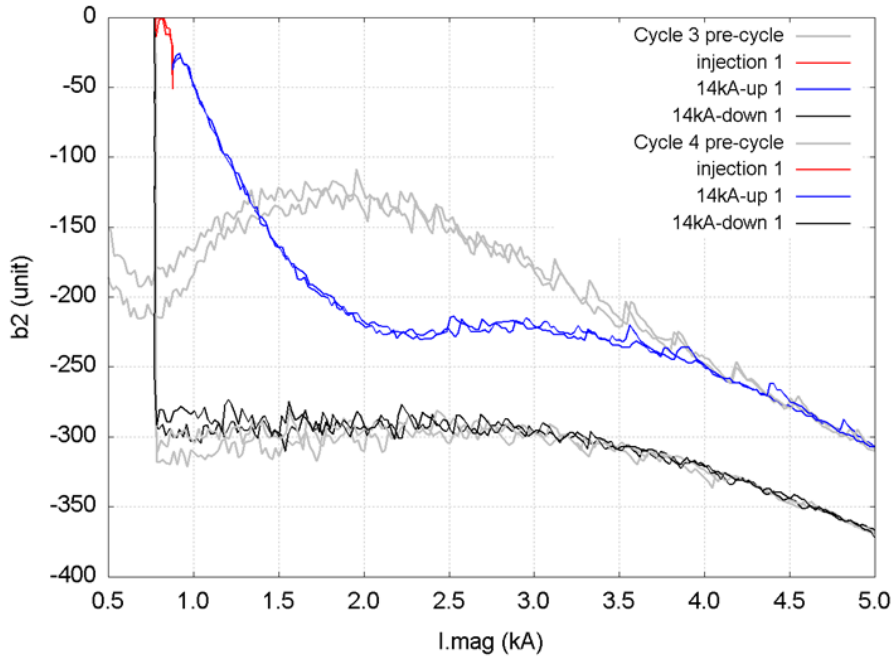

Figure 28 b_2 at low current level (0 - 5 kA).

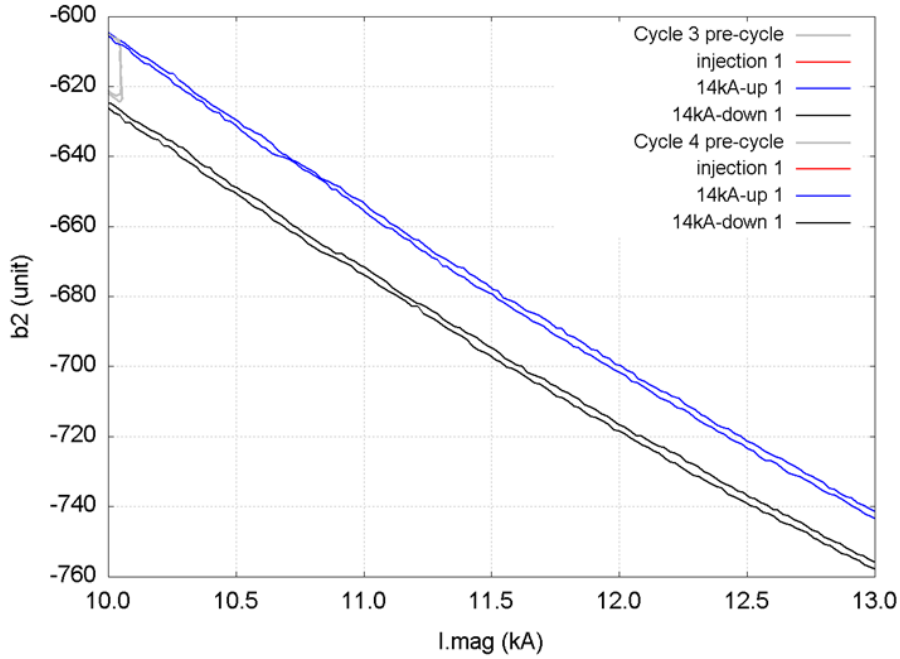

Figure 29 b_2 of cycle 3 and 4 for current between 10 and 13 kA.

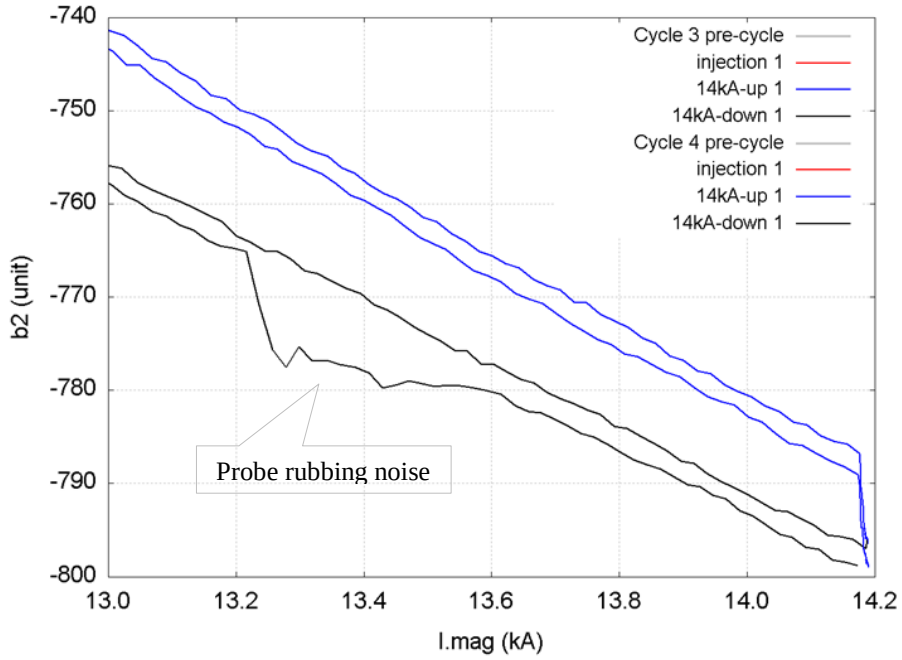

Figure 30 b_2 at high current level (13 - 14 kA). The bump during the down ramp of cycle 4 was due to the rubbing of the probe against the anticryostat.

6.2.1.2 Normal and skew sextupole

Figure 31 and Figure 32 show the current dependence of the normal and skew sextupole of two measurements, cycle 3 and cycle 4, measured with the 250 mm probe.

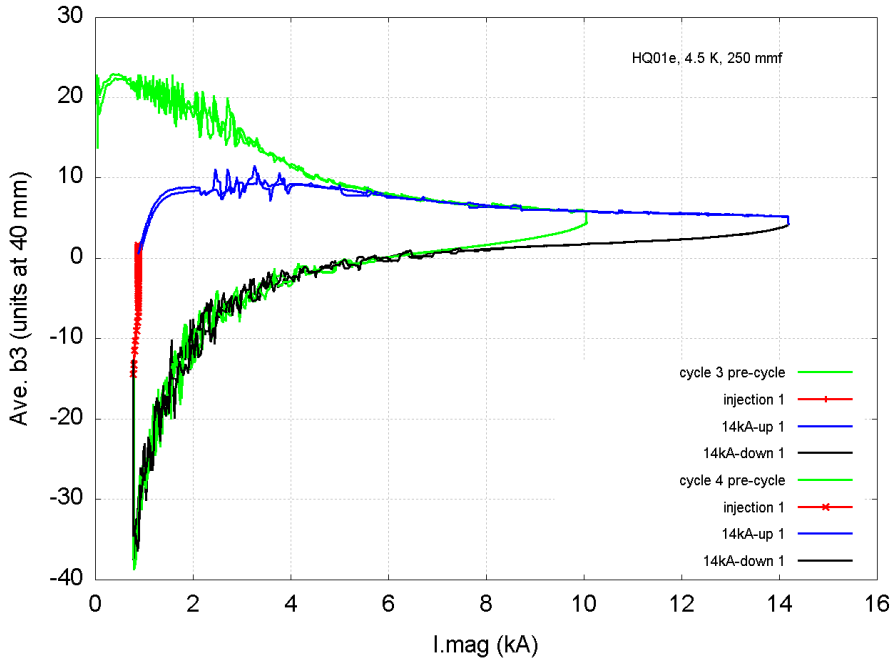

Figure 31 Current dependence of the normal sextupole coefficients from two measurements, cycle 3 and cycle 4.

The observed a_3 at low current could be partially due to the different persistent current resulted from the different conductor filament size that contributes to the top-bottom asymmetry. This

effect becomes less pronounced as the persistent current effect decreases at high current (if divide a_3 by b_3 for the same current, there seems to be a ratio of 2).

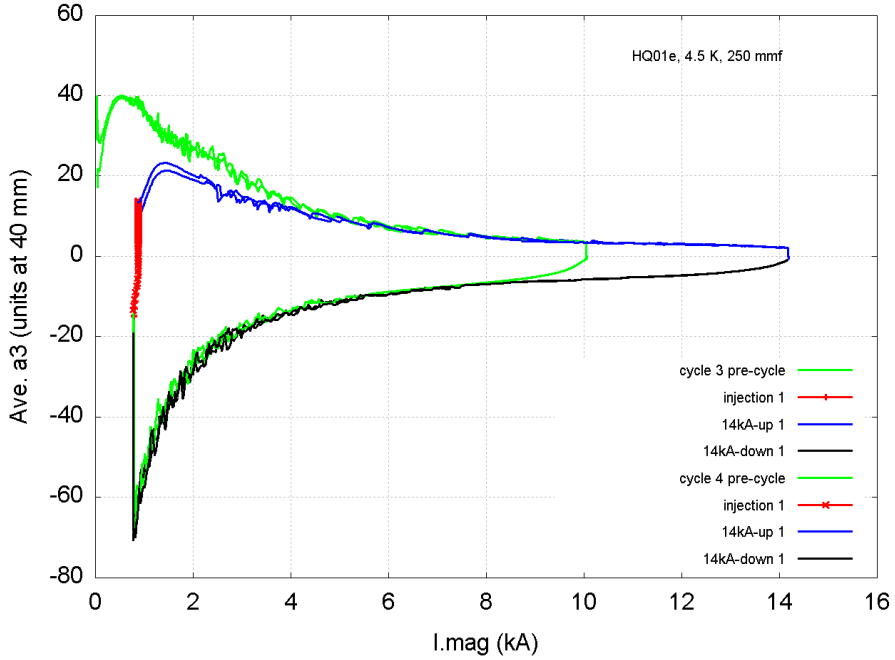

Figure 32 Current dependence of the skew sextupole coefficients from two measurements, cycle 3 and cycle 4.

6.2.1.3 Normal 12-pole

Figure 33 shows the current dependence of the b_6 coefficient of two measurements, cycle 3 and cycle 4, measured with the 250 mm probe.

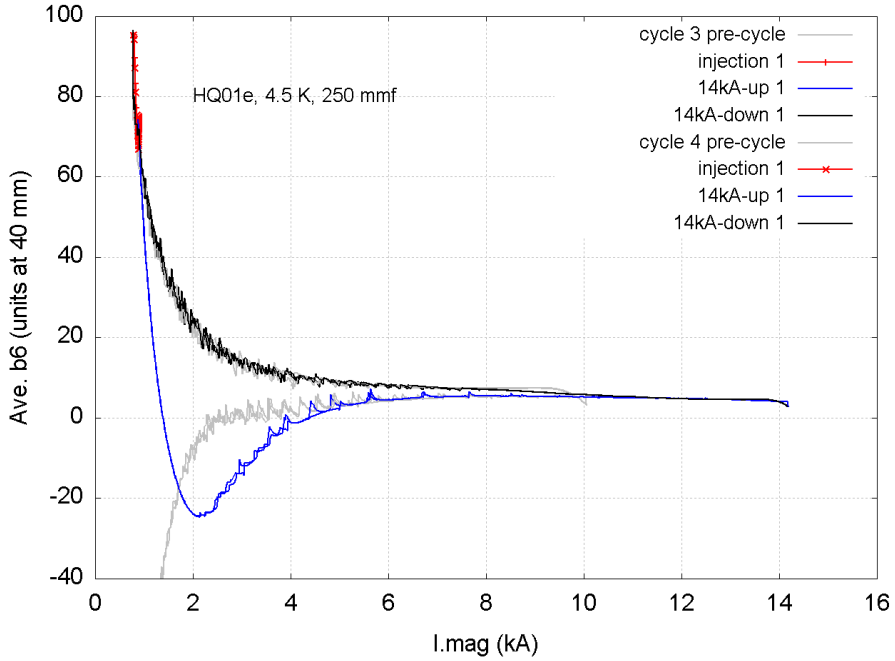

Figure 33 Current dependence of b_6, cycle 3 and cycle 4, 250 mm probe.

6.2.1.4 Normal 20-pole

Figure 34 shows the current dependence of the b_{10} coefficient of two measurements, cycle 3 and cycle 4, measured with the 250 mm probe.

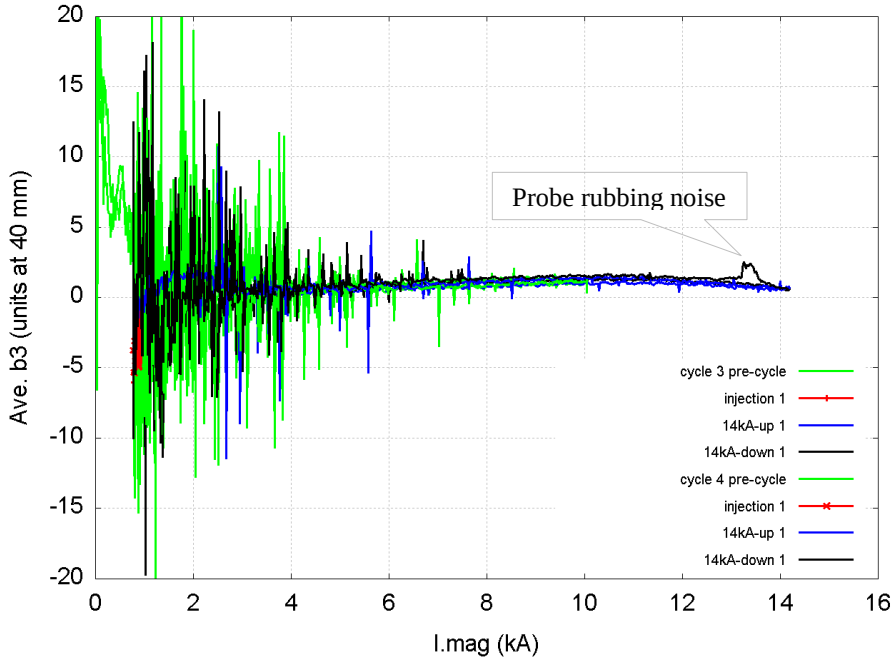

Figure 34 Current dependence of b_{10}, cycle 3 and cycle 4, 250 mm probe.

6.2.2 Multipoles at injection level

Figure 35 shows the B_2 main field during the injection at 880 A (10.7 T/m). An initial decay of ~ 7 Gauss during the first 120 s after the current stopped ramping was observed. A rectangular waveform of B_2 with a period of ~ 24 s and a 17% duty cycle was observed. The same pattern was also seen at high current. The cause is not clear. The amplitude change was ~ 2 Gauss (< 0.05%) and the resulting error in the calculation of the normalized harmonics can be neglected.

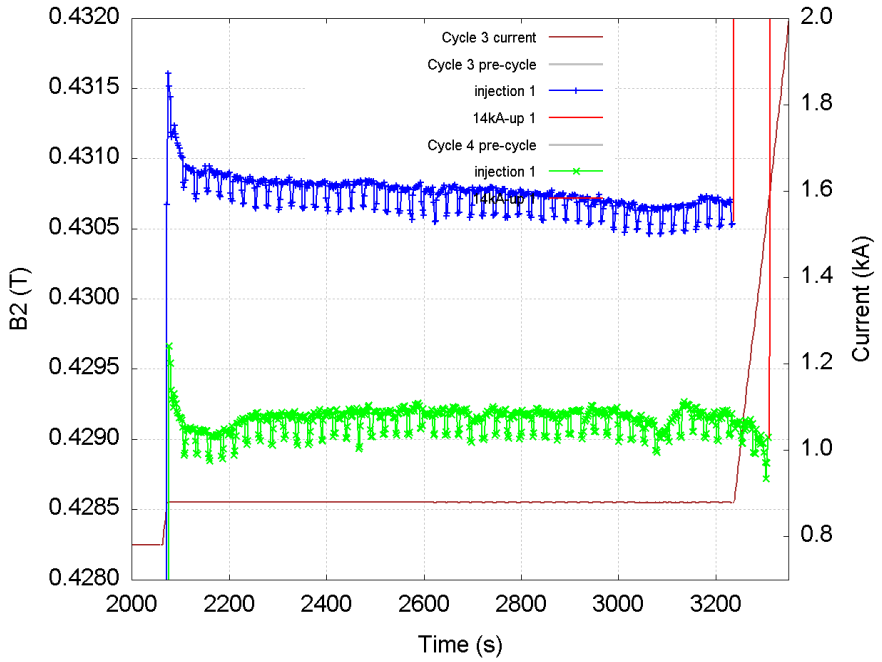

Figure 35 B_2 during the injection, cycle 3 (blue) and cycle 4 (green).

The time dependence of the 12-pole coefficient from two measurements is shown in Figure 36. The b_6 of cycle 3 was ~ 1.3 units lower than that of cycle 4.

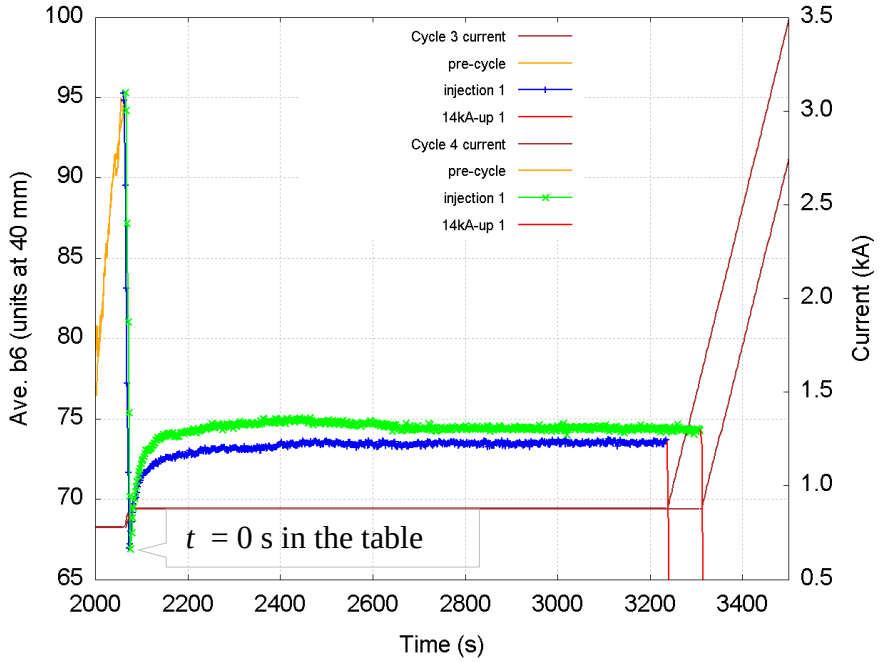

Figure 36 b_6 during the simulated injection level with I.mag = 880 A (10 T/m), cycle 3 (blue) and cycle 4 (green).

The multipole coefficients at three different timestamps at the injection level are reported in Table 12. At 0 s, the current reached 880 A and the ramping stopped, the harmonics at this time was reported. The results at 120 s and 1160 s (or 1200 s for cycle 4) were averaged over 5 measurements (10 s duration). The results from two measurements generally agreed with each other except that that a_6 of cycle 4 was about three times larger than those of cycle 3. Decay of

more than 3 units during the 20 minute injection in both measurements was observed in b_3, b_6, a_3, a_7. The coefficient b_6 in both measurements were ~ 74 units at the end of the injection. The coefficient a_5 with amplitude of ~ 17 – 18 units, without significant change over the injection, was seen in both measurements.

Table 12 Multipoles at the inject level of two measurements, cycle 3 and cycle 4.

	Cycle 3: 878 A				Cycle 4: 874 A			
	0 s	120 s	1160 s	Δ	0 s	120 s	1200 s	Δ
b3	-6.18	-2.23	-0.41	5.77	-6.68	0.08	0.72	7.39
b4	-2.32	-2.11	-1.32	1.00	-2.84	-0.52	-0.31	2.54
b5	-1.45	-1.25	-0.98	0.46	-0.30	1.20	0.63	0.93
b6	67.22	72.80	73.52	6.30	67.92	74.19	74.34	6.42
b7	-1.20	0.07	0.27	1.47	-1.02	-0.10	-0.04	0.98
b8	-0.65	0.01	-0.18	0.47	0.13	0.14	0.40	0.27
b9	-0.02	0.20	0.16	0.18	-1.10	-0.10	0.74	1.84
b10	-4.83	-4.21	-4.08	0.76	-4.88	-3.29	-2.23	2.65
a3	-3.83	7.22	10.33	14.16	-2.42	9.15	13.60	16.02
a4	-1.28	0.92	2.69	3.97	-0.20	1.43	2.12	2.33
a5	18.11	17.07	17.89	-0.22	17.40	16.71	17.03	-0.37
a6	0.95	0.45	0.94	-0.01	3.09	3.06	2.32	-0.77
a7	-5.51	-2.81	-1.80	3.71	-4.47	-1.68	-1.29	3.18
a8	-0.05	0.24	0.75	0.81	1.20	0.74	0.02	-1.18
a9	0.42	0.79	0.88	0.47	1.28	0.66	0.29	-0.98
a10	-0.50	0.14	0.39	0.90	-0.43	0.21	0.63	1.06

The decay of b_6 over time at the injection level can be fit with an exponential function with two time constants, characterizing a fast and slow decaying components, respectively [Fischer01, Sammut06]. Figure 37 shows the fitting curves based on exponential fit with single time constant, logarithm fit and exponential fit with two time constants, which has the best agreement with the measured data. The normalized change of b6 can be fit by $\Delta b_6(t)$ = 0.722133*exp(-t/28.0) + 0.152896*exp(-t/545.7), where t is in s.

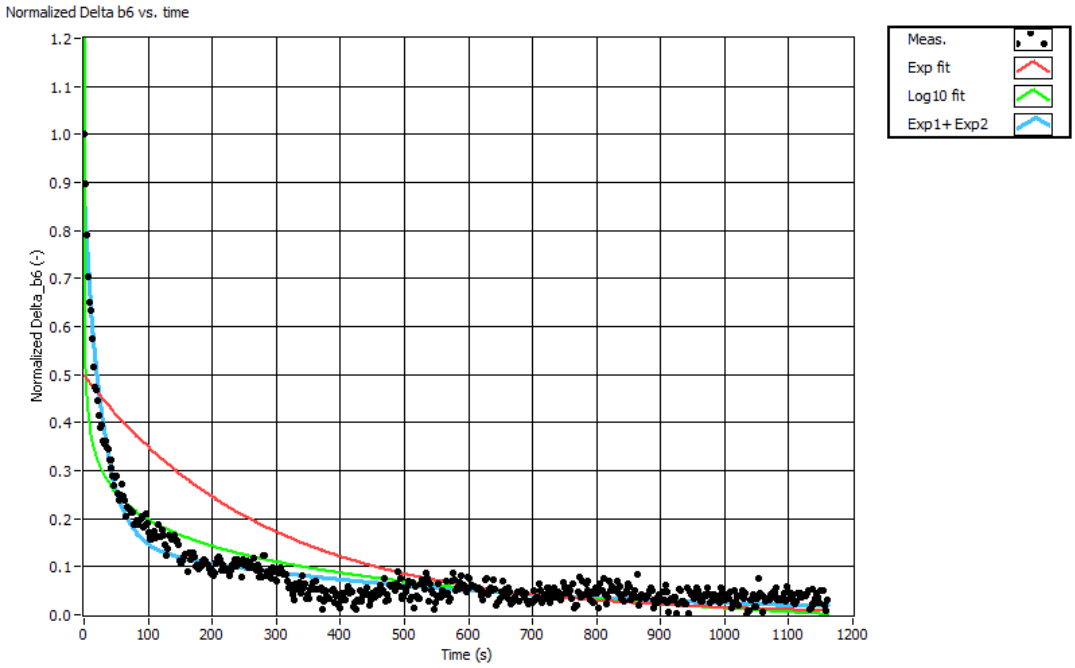

Figure 37 Decay of b_6 at the injection level, cycle 3, 250 mm probe.

6.2.3 Multipoles at nominal current

The multipoles during the up ramp at the nominal current (14.2 kA, 82% of I_{ss} at 4.4 K) are reported here. Harmonics decay was again observed at the nominal current. An example for b_6 is shown in Figure 38. The holding time was ~ 75 s at the peak current and the harmonics did not show any plateau. Thus, the harmonics at the beginning and the end of the current holding were reported without averaging over a few measurements for the magnetization measurement with continuous ramping before reaching the nominal current. Note that the power supply current increased 10 A (drifting) during the "holding" in cycle 3 and increased 12 A in cycle 4. The averaged current over the holding period was reported.

For comparison, the harmonics measured during the stair-step measurement was also included (see section 7 for more details). In this case, the holding time was ~ 280 s and a plateau of b_6 was observed (Figure 39). Magnet current drifted for ~ 58 A during the measurement. The harmonics of the last 15 measurements were averaged and reported as the mean harmonics at the end of the holding at the nominal current.

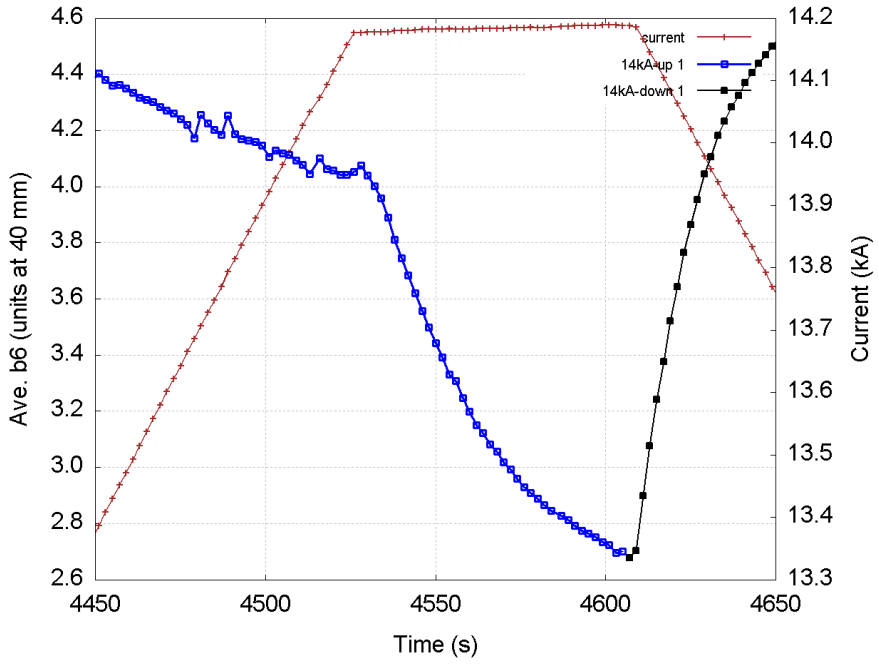

Figure 38 Decay of b_6 at 14.2 kA (cycle 3).

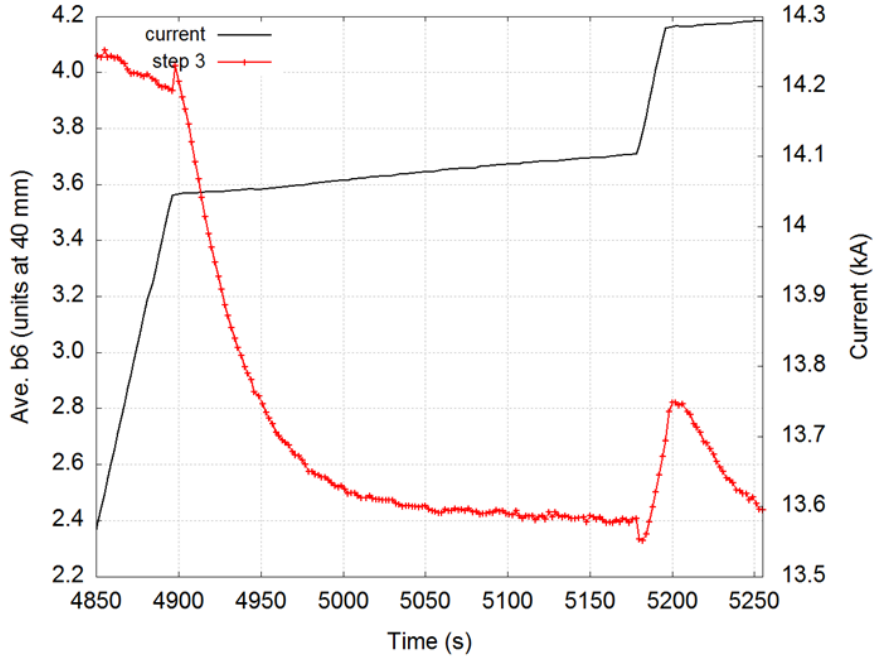

Figure 39 Decay of b_6 during a holding time of ~ 280 s (stair step measurement #3).

Table 13 summarizes the multipole coefficients of three measurements, two magnetization measurements (cycle 3 and 4) and one stair-step measurement (step 3). Good agreement was shown between three measurements. During the holding period, three harmonics had the largest change of amplitude: b_3, b_6 and a_3. A comparison to the harmonics at the injection level showed several significant changes in harmonics (even though the holding time at high current was much shorter and may not be a good comparison). For example, b_3 increased from -0.4 units to 4 units while a_3 reduced from 10 units to -0.9 units; b_6 reduced from 73 units to 2.7 units and was still

decaying at the end of the current holding; b_{10} reduced from -4 units to ~ 0.65 units. The coefficient a_4 was 2.2 units, similar to the 2.7 units at the injection level.

Table 13 Mulitpole coefficients at the beginning and end of the current holding at the nominal level 14.2 kA.

	Cycle 3: 14184 A			Cycle 4: 14183 A			Step 3: 14096 A			Cycle 3 injection 1160 s
	0 s	77 s	Δ	0 s	75 s	Δ	0 s	266 s	Δ	
b3	5.05	4.11	-0.94	5.12	4.13	-0.99	5.14	3.92	-1.21	-0.41
b4	1.21	0.95	-0.26	1.19	0.93	-0.25	1.18	0.85	-0.33	-1.32
b5	0.10	-0.05	-0.15	0.03	-0.09	-0.12	0.03	-0.11	-0.14	-0.98
b6	4.04	2.68	-1.36	4.04	2.66	-1.37	4.02	2.40	-1.62	73.52
b7	0.97	0.79	-0.19	1.03	0.88	-0.15	0.95	0.78	-0.17	0.27
b8	-0.16	-0.09	0.07	0.05	0.08	0.03	-0.18	-0.09	0.09	-0.18
b9	0.10	0.08	-0.02	0.40	0.34	-0.06	0.23	0.01	-0.22	0.16
b10	0.54	0.60	0.06	0.71	0.70	-0.01	0.59	0.54	-0.05	-4.08
a3	1.99	-0.93	-2.92	2.01	-0.90	-2.91	2.04	-1.61	-3.65	10.33
a4	2.38	2.18	-0.19	2.34	2.20	-0.14	2.28	2.13	-0.15	2.69
a5	-0.67	-0.91	-0.23	-0.72	-0.98	-0.26	-0.51	-0.84	-0.32	17.89
a6	-0.54	-0.36	0.18	-0.65	-0.48	0.17	-0.53	-0.33	0.19	0.94
a7	1.15	0.61	-0.54	0.96	0.44	-0.52	1.14	0.47	-0.67	-1.80
a8	-0.12	-0.15	-0.03	-0.26	-0.25	0.01	0.02	0.05	0.04	0.75
a9	-0.15	-0.22	-0.07	-0.01	-0.14	-0.13	-0.10	-0.16	-0.06	0.88
a10	-0.15	-0.07	0.08	0.00	0.13	0.13	-0.11	0.07	0.17	0.39

6.3 14 kA measurement, 100 mm probe

After the magnetization measurement was completed using the 250 mm probe, it was replaced with the 100 mm probe to repeat the magnetization measurement. The current profile (Figure 40) had two differences from that of the 250 mm probe (Figure 25), 1) only one measurement cycle was included to save the measurement time as no significant difference between two measurement cycles was observed in the results of 250 mm probe; 2) to partially repeat the first measurement cycle, the final ramp rate to the cleansing quench current level was 10 A/s instead of 50 A/s.

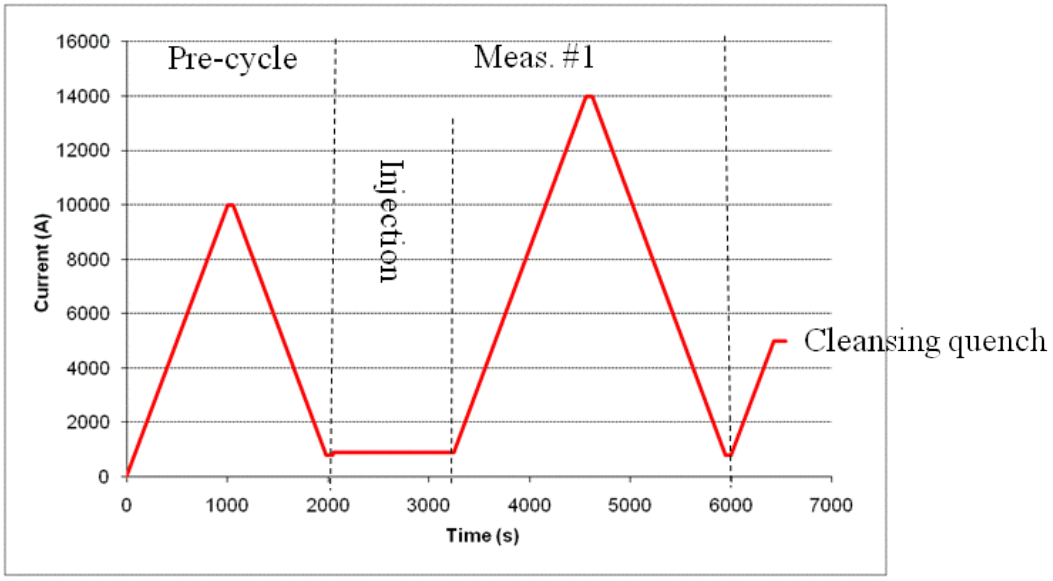

Figure 40 Current profile for the magnetization measurement using the 100 mm probe.

Two measurements, cycle 5 and cycle 6, were performed with the 100 mm probe with its center located at z = -75 mm (Figure 12). The current dependence of multipoles between the measurements from the 250 mm and 100 mm probes are similar at both the injection level and nominal current level.

Table 14 Multipoles at the inject level of two measurements, 100 mm probe, cycle 5 and cycle 6.

	Cycle 5: 881 A				Cycle 6: 876 A			
	0 s	120 s	1205 s	Δ	0 s	120 s	1204 s	Δ
b3	-4.92	-1.58	-0.45	4.46	-15.62	-8.83	-4.71	10.92
b4	1.30	0.99	0.94	-0.35	0.86	-0.64	-0.03	-0.89
b5	-2.72	-1.84	-1.71	1.00	-3.35	-1.15	-0.32	3.03
b6	67.59	71.70	72.05	4.46	62.97	70.30	71.32	8.35
b7	-0.24	0.29	0.27	0.51	-0.13	0.44	0.85	0.98
b8	0.25	0.00	0.00	-0.25	1.35	-0.16	0.76	-0.59
b9	-0.07	-0.17	0.44	0.51	-0.41	0.68	1.45	1.86
b10	-2.37	-4.60	-5.79	-3.42	-4.76	-4.26	-4.84	-0.08
a3	3.54	7.73	9.48	5.94	-5.84	7.83	10.35	16.19
a4	-4.80	-2.71	-1.95	2.85	-5.74	-1.64	-1.12	4.62
a5	18.15	16.64	16.17	-1.99	16.29	16.47	15.21	-1.08
a6	0.89	1.55	1.82	0.93	2.26	2.93	3.24	0.97
a7	-5.42	-3.46	-2.93	2.49	-8.05	-3.23	-3.33	4.72
a8	-1.97	-1.03	-0.96	1.01	-0.35	0.09	-0.19	0.16
a9	-1.49	-0.01	0.00	1.49	-0.31	0.17	0.47	0.77
a10	-1.68	-0.06	0.43	2.10	-0.64	0.72	1.45	2.10

Table 15 Multipoles at the nominal current level of two measurements, cycle 5 and cycle 6, 100 mm probe, reference radius = 40 mm.

	Cycle 5: 14169 A			Cycle 6: 14172 A		
	0 s	72 s	Δ	0 s	68 s	Δ
b3	6.39	5.25	-1.14	6.20	5.07	-0.99
b4	1.31	1.19	-0.12	1.14	0.98	-0.25
b5	0.26	-0.01	-0.28	0.26	-0.08	-0.12
b6	4.50	3.17	-1.33	4.80	3.49	-1.37
b7	0.75	0.63	-0.13	1.04	0.96	-0.15
b8	-0.33	-0.29	0.04	-0.41	-0.37	0.03
b9	-0.01	-0.11	-0.10	-1.17	-1.33	-0.06
b10	1.02	0.97	-0.05	0.98	0.91	-0.01
a3	2.18	-0.80	-2.98	2.29	-0.65	-2.91
a4	2.43	2.08	-0.35	2.41	1.94	-0.14
a5	-1.02	-1.38	-0.36	-1.24	-1.69	-0.26
a6	-0.42	-0.20	0.21	-0.71	-0.53	0.17
a7	1.58	1.05	-0.54	1.76	1.27	-0.52
a8	0.02	0.02	0.00	0.78	0.79	0.01
a9	0.28	0.13	-0.15	0.37	0.30	-0.13
a10	0.48	0.53	0.05	-0.14	-0.01	0.13

7 Stair-step measurement at 4.4 K

7.1 Current profile

To measure the multipoles at different current levels, a current profile as shown in Figure 41 was set up. It consists of the following 5 stages:

1. Precycle: 10 A/s from 50 A to 10 kA. Hold for 1 minute and ramp down to 800 A with -10 A/s. Hold for 1 minute.
2. Up ramp stair-steps: ramp with 10 A/s and hold for 4 minutes at the even current levels (kA). At 14 kA, hold for only 3 minutes.
3. Ramp up 14.3 kA and hold for 1 minute.
4. Down ramp stair-steps: ramp with -10 A/s and hold for 3 minutes at 14 kA and 4 minutes at all other even current levels (kA). Ramp down to 800 A and hold for 1 minute.
5. Cleansing quench: ramp to 5 kA and provoke a quench with 10 A/s.

The measurement was similar to the "load-line" measurement in [Bellesia04]. The 250 mm long PCB probe was used first followed by an unsuccessful attempt to repeat with the 100 mm probe.

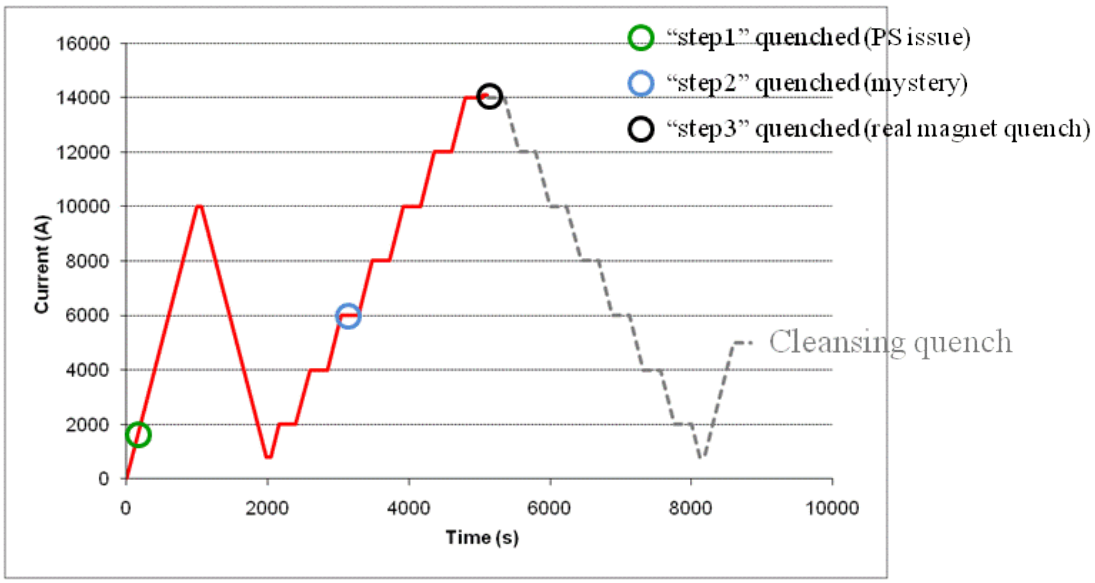

Figure 41 Current profile for the stair-step measurement using the 250 mm probe. The part with the dashed line was not performed.

Three unexpected quenches occurred. Two of them were provoked due to external issues and one was a real magnet quench. Due to the resource constraint, the down-ramp part was not attempted. Instead, a profile as shown in Figure 42 was used. The procedure was,

1. Ramp from 50 A to 9 kA with 50 A/s. Reduce to 10 A/s up to 14.3 kA and hold for 3 minutes.
2. Down ramp stair-steps: -10 A/s from 14 kA to 50 A. Hold for 3 minutes at 14 kA and 4 minutes at other even current levels (kA). There was no cleansing quench at the end of the profile.

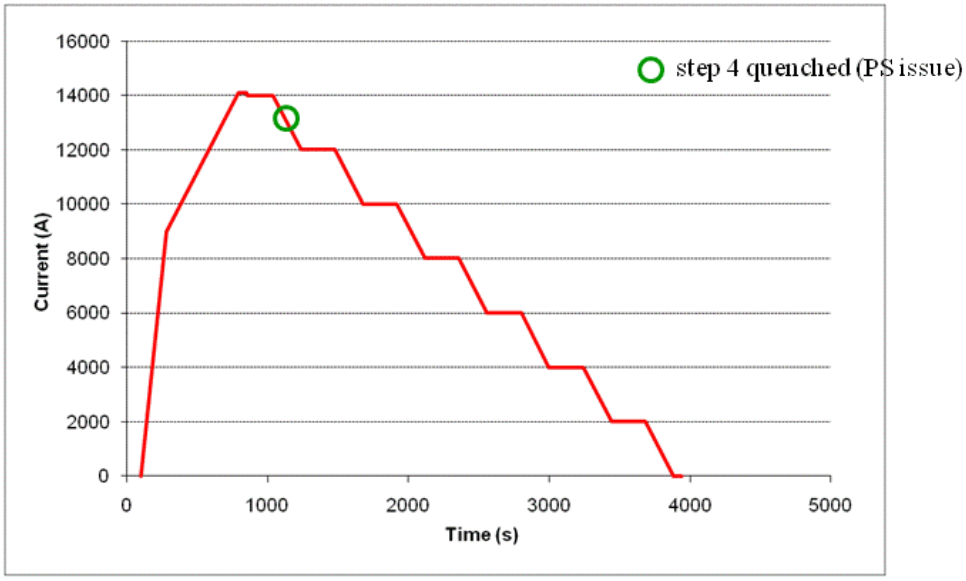

Figure 42 Current profile for the down ramp stair-step measurement using the 250 mm probe.

7.2 Comparison to the magnetization measurement

B_2 transfer function during the up- (step 3) and down-ramp (step 5) of the stair-step measurements using the 250 mm probe are shown in Figure 43. For comparison, the result from the magnetization measurement (cycle 3) is included. When the current stops ramping, B_2 of the stair-step measurement decays due to the damping of dynamic effect and the persistent current at low field. When the current ramping resumed, B_2 approached to the curve of the continuous ramping in about 200 s (10 A/s). In general, the amplitude of decay decreases with increasing current level. Taking the 12.304 T/m/kA as the nominal value for the transfer function at the injection level, the decay is about 65 units at 2 kA and 8 units at 14 kA during the up ramp.

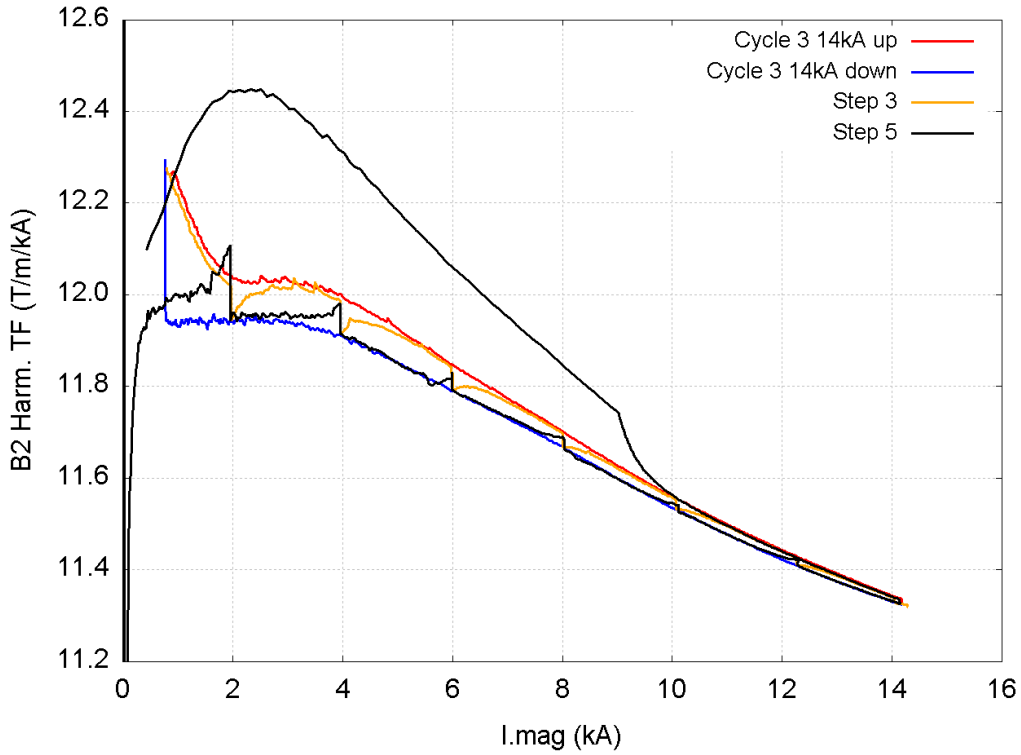

Figure 43 B_2 transfer function comparison between the stair-step measurement and the magnetization measurement (cycle 3), both measured with the 250 mm probe.

For the same current level, B_2 transfer function of the down-ramp was larger than that of the up-ramp after the decay, contrary to the case during the continuous measurement (cycle 3, red and blue lines).

The b_6 from the stair-step measurement is shown in Figure 44. For comparison, the result from the magnetization measurement (cycle 3) is included. When the current stops ramping, b6 of the stair-step measurement decays due to the damping of dynamic effect and the persistent current at low field. When the current resumes ramping, b6 approaches back to the curve of the continuous ramping in about 200 s (10 A/s). This seems to be similar to the "decay and snap-back" phenomenon observed in NbTi accelerator dipole magnets during the injection level.

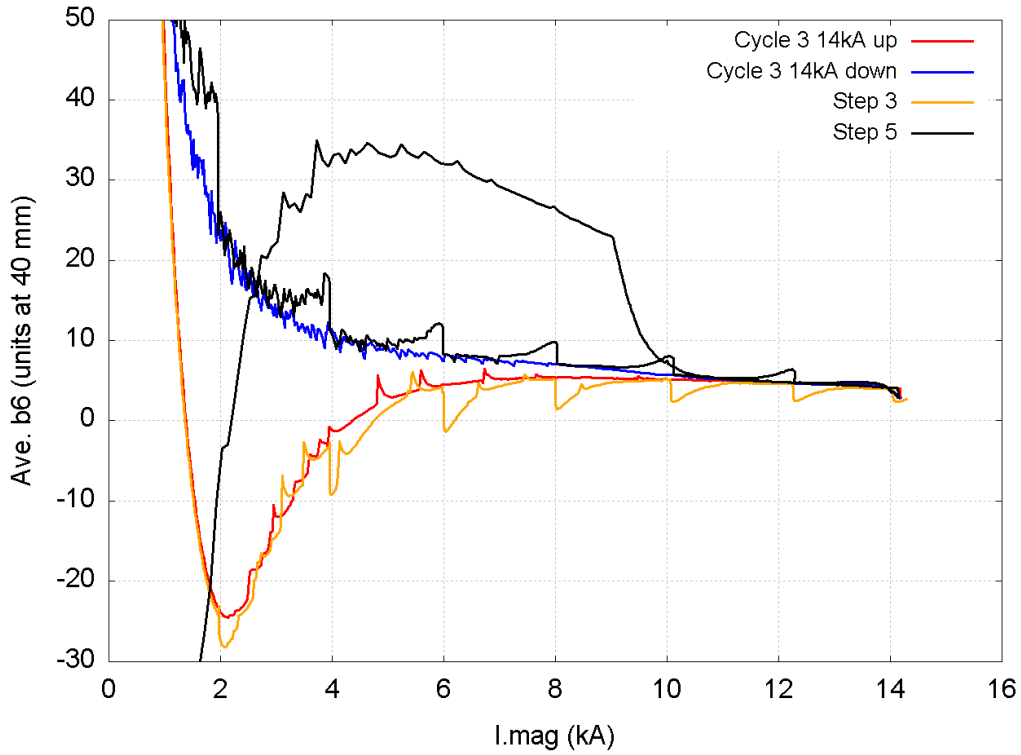

Figure 44 Comparison between the stair-step measurement (step 3 and step 5) and the magnetization measurement (cycle 3), all using the 250 mm probe.

The black line in Figure 44 corresponds to the b_6 of the down-ramp of the stair-step measurement (step 5). The ramp rate was reduced from 50 A/s to 10 A/s at 9 kA (Figure 42). About 300 s after the reduction of the ramp rate, i.e., at 12 kA, b_6 approached to the curve of the continuous ramping at 10 A/s from 880 A (cycle 3 red line). This indicates that the fast up-ramping to a lower current level followed by a slow ramping up to 14 kA may be equivalent to the continuous ramping from 880 A at 10 A/s.

7.3 Harmonics decay during the current holding

Once the current stopped ramping, harmonics decay was observed. An example of the measurement of b_6 at 8 kA during the up ramp (step 3) is shown in Figure 45. The decay started when the current ramping stopped. The level became stable at ~ 200 s after the current holding (the total holding time was 240 s). An exponential fit of the normalized decay yielded a time constant of 42 seconds (Figure 46). This long time constant was due to the inter-strand coupling currents with small crossover resistance [Verweij95, denOuden97].

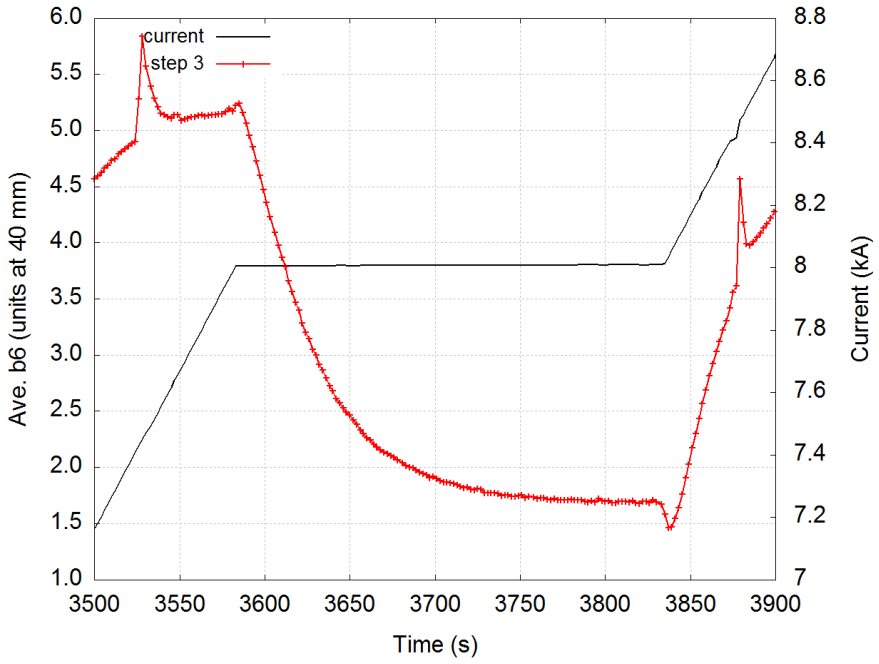

Figure 45 Decay of b_6 during the 8 kA holding (step 3, 250 mm probe).

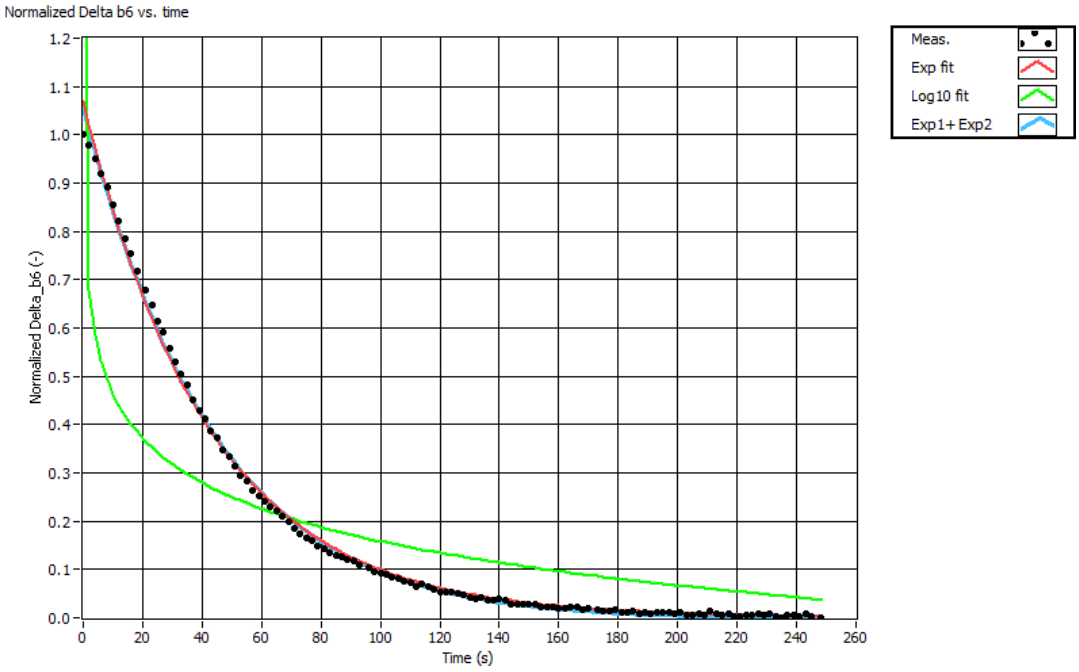

Figure 46 Exponential fit of the decay normalized from the data shown in Figure 45.

7.4 DC contribution to field errors

The multipole coefficients typically approached to a constant level at the end of 3 – 4 minute long holding of the current. The last 15 measurements at the end of current holding (acquired over 30 s) were averaged as the harmonics at the DC level. The choice of 15 was a compromise between the decay behavior (for the harmonics to reach a stable value) and a number of measurements for certain statistics. The DC harmonics are supposed to be contributed by mainly

the DC effect, e.g., geometric contribution, persistent current, iron saturation and etc. Note that the holding time for the current was 40 s in the load-line measurement of LHC NbTi dipole magnets [Bellisia04].

7.4.1 Main field

The B_2 transfer function at the DC level (up- and down- ramp) was shown in Figure 47. The data at the inject level was from cycle 3 measurements at the end of the 20-minute-long holding of the current at 880 A. Results of the 2D transfer function calculations using Opera and Roxie were also reported for comparison. For the 2D calculation, two cases were considered. The first case without the magnetization effect: red (Opera) and green (ROXIE) lines in Figure 47. The second case considered the magnetization effect in ROXIE assuming a 100 μm effective diameter of the Nb_3Sn subelement. The results are shown in blue (up-ramp) and orange (down-ramp) curves. Only one octant was considered in the calculation. All data (measurement and calculation) were obtained following the pre-cycle.

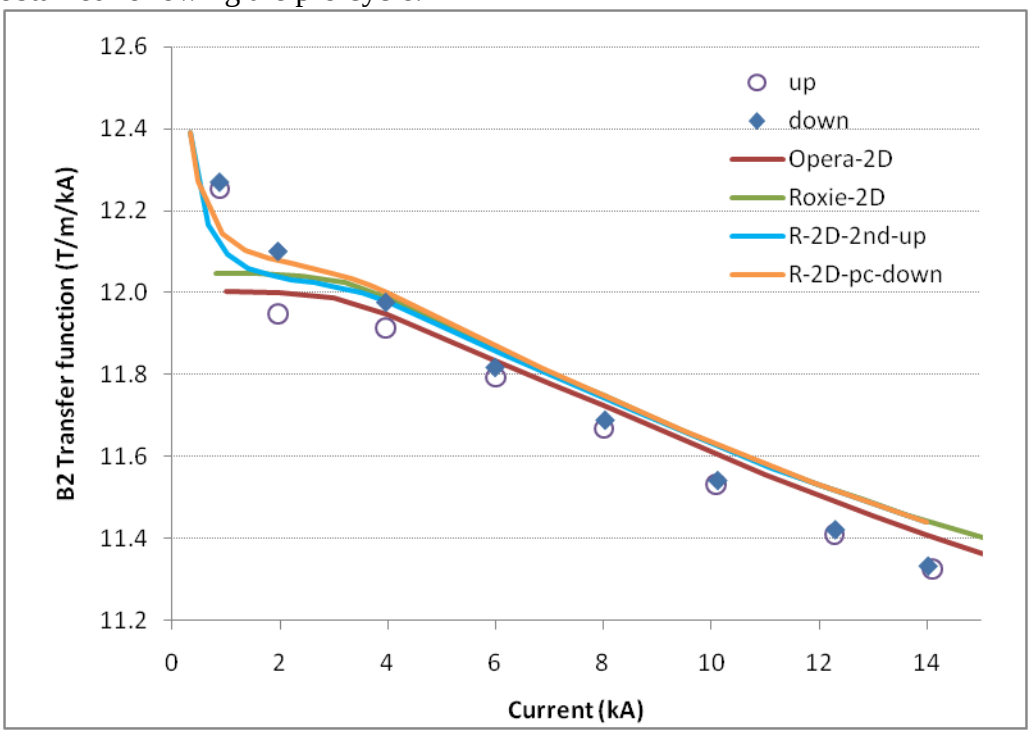

Figure 47 B_2 transfer function comparison between the measurement and calculation.

At the current level close to the injection, filament magnetization contributed significantly to the measured transfer function. The reason for the discrepancy (~ 0.8%) between the measured and calculated results at higher current levels is due to the conductor parameter used in the simulation. With a different set of conductor parameters, Auchmann *et al.* reproduced the measurement with an excellent agreement [Auchmann11].

7.4.2 Geometric multipoles

Figure 48 shows the b_6 data at different DC levels. The data at the inject level was again from cycle 3 measurement at the end of the 20-minute-long holding of the current at 880 A. The geometric contribution can be determined by the harmonic level averaged between the up- and down-ramp branches between 5 and 10 kA, where the persistent current effect became low and

iron saturation effect was insignificant. One evidence is that the $b_6(I)$ from the up-ramp in the pre-cycle and the following up-ramp started converging at ~ 5 kA (Figure 33). The geometric component of b_6 was determined to be 5.32 units at 6 kA at a reference radius of 40 mm, as indicated by the dashed line in Figure 48.

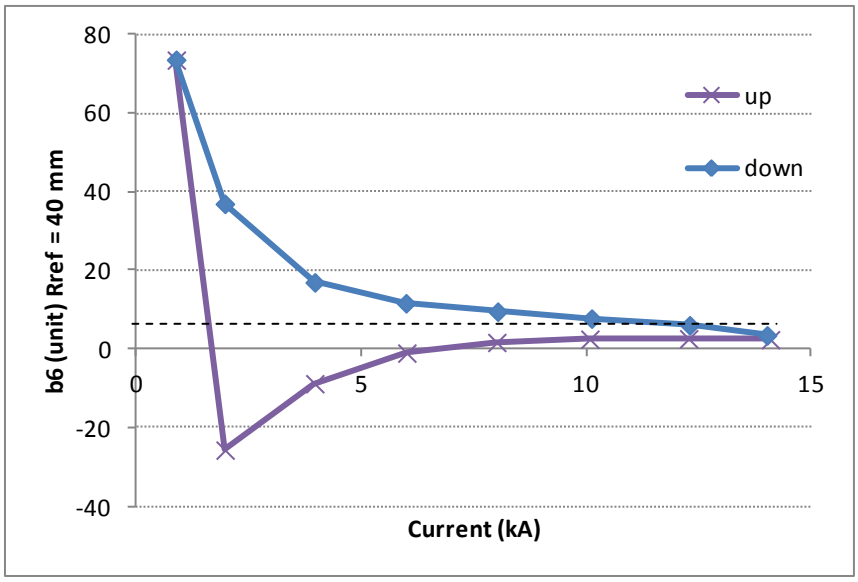

Figure 48 Current dependence of b_6 from the stair-step measurement (step 3 and step 5), 250 mm probe. The dashed line corresponds to the geometric component of 5.32 units determined at 6 kA.

The decreasing averaged harmonics above 12 kA, compared to the dashed line, may indicate the saturation effect of iron yoke.

The multipole coefficients at 6 kA, 8 kA and 10 kA are reported in Table 16 - Table 18, respectively. These may be considered as the geometric multipoles of the magnet. The coefficients were averaged from the last 15 measurements at each current level, including both up and down ramps. The error was given by $\sigma/\sqrt{N}$, where σ is the standard deviation and N = 15. The average between the mean coefficients at the up- and down-ramp was listed in the last column. Note that the current levels were not identical for the up and down ramps due to the power supply control at the up- and down-ramp; but the resulting error was believed to be negligible.

Since relative position of the probe with respect to the magnet was changed, a negative sign was applied to all harmonics of odd orders so that they have the same polarity as in the cycle measurements.

Table 16 Multipole coefficients at 6 kA during the stair-step measurement, 250 mm probe, reference radius = 40 mm.

	6006 A		5988 A		
	up		down		average
	mean	error	mean	error	
b3	3.85	0.00256	2.79	0.00267	3.32
b4	0.53	0.00158	0.06	0.00476	0.30
b5	-0.26	0.00135	0.27	0.00742	0.00

b6	-1.01	0.00378	11.66	0.01423	5.32
b7	0.59	0.00384	0.62	0.02000	0.60
b8	-0.01	0.00551	-0.13	0.01949	-0.07
b9	0.04	0.01195	0.35	0.08478	0.19
b10	0.71	0.01573	2.95	0.28445	1.83
a3	-4.30	0.00446	0.37	0.00619	-1.97
a4	1.94	0.00087	2.48	0.00164	2.21
a5	-3.14	0.00150	1.56	0.00282	-0.79
a6	-0.29	0.00265	-0.27	0.01146	-0.28
a7	0.66	0.00453	0.28	0.03537	0.47
a8	-0.14	0.00739	-0.57	0.08668	-0.36
a9	0.30	0.01164	-1.11	0.18309	-0.41
a10	-0.06	0.02271	-0.98	0.03692	-0.52

Table 17 Multipole coefficients at 8 kA during the stair-step measurement, 250 mm probe, reference radius = 40 mm.

	8009 A		8029 A		
	up		down		average
	mean	error	mean	error	
b3	3.89	0.00111	3.23	0.00122	3.56
b4	0.55	0.00082	0.14	0.00130	0.35
b5	-0.26	0.00114	-0.22	0.00161	-0.24
b6	1.69	0.00226	9.52	0.00165	5.61
b7	0.63	0.00424	0.78	0.00413	0.71
b8	0.03	0.00660	0.09	0.00824	0.06
b9	-0.02	0.01326	0.17	0.01987	0.08
b10	0.83	0.01163	1.62	0.01851	1.22
a3	-2.96	0.00253	-0.09	0.00168	-1.53
a4	2.10	0.00091	1.93	0.00127	2.02
a5	-2.12	0.00105	0.78	0.00109	-0.67
a6	-0.24	0.00211	-0.30	0.00326	-0.27
a7	0.59	0.00178	0.41	0.00376	0.50
a8	-0.06	0.00545	-0.19	0.00922	-0.12
a9	0.19	0.01177	-0.09	0.01118	0.05
a10	0.03	0.01747	-0.30	0.02627	-0.13

Table 18 Multipole coefficients at 10 kA during the stair-step measurement, 250 mm probe, reference radius = 40 mm.

	10079 A		10118 A		
	up		down		average
	mean	error	mean	error	
b3	3.88	0.00095	3.33	0.00349	3.60
b4	0.66	0.00079	0.29	0.00653	0.47

b5	-0.19	0.00136	-0.26	0.00746	-0.22
b6	2.52	0.00259	7.76	0.00619	5.14
b7	0.70	0.00368	0.97	0.01135	0.84
b8	-0.01	0.00514	0.27	0.04183	0.13
b9	0.05	0.01078	0.87	0.10792	0.46
b10	1.01	0.01730	2.52	0.07250	1.76
a3	-2.05	0.00326	-0.43	0.00312	-1.24
a4	2.09	0.00147	1.94	0.00131	2.01
a5	-1.48	0.00133	0.40	0.00519	-0.54
a6	-0.26	0.00152	-0.49	0.01447	-0.37
a7	0.60	0.00233	0.14	0.02959	0.37
a8	-0.01	0.00579	-0.45	0.04102	-0.23
a9	-0.01	0.01389	-0.53	0.04068	-0.27
a10	0.15	0.01974	0.12	0.12549	0.13

From Table 16- Table 18, one sees that HQ01e had about -3.50 units of b_3, 5.32 units of b_6, and 1.60 units of b_{10} over the 6 – 10 kA range. Low order skew harmonics a_3 and a_4, averaged between up and down ramps, were between 1 – 2 units. This indicates that top-bottom and left-right symmetries were broken for HD01e over this current range. All other harmonics (up to the 10^{th} order) were generally within 1 unit.

The multipole coefficients for the 14 kA step were reported in Table 13.

7.4.3 Persistent current effect

By subtracting the geometric contribution, the persistent current contribution is shown in Figure 49 (open symbols). The magnetization contribution was ~ 68 units at the injection level. The hysteresis width is ~ 50 units at 2 kA. The large persistent current contribution was due to the magnetization of the filaments with large diameter and high J_c at low field. The penetrating field for the filament radius of 25 μm (54/61) to 35 μm (108/127) ranged from 0.89 T to 1.1 T based on the extrapolation of the J_c at low field from the Summers fit of the measured J_c at 12 – 15 T.

Simulation using Opera 2D with $B(H)$ curve based on the measured magnetization of a single strand is being checked (black line in Figure 49) [Kashikhin99]. The magnetization data was for a 1 mm diameter strand [Kashikhin99], different from what was used for HQ01e. Magnetization data of HQ01e strand has to be found or measured for more accurate modeling results.

ROXIE 2D simulation considering the persistent current effect based on a filament (sub-element) diameter of 70 μm gives a much smaller effect compared to the measurement (Figure 49). Increasing filament (sub-element) diameter only increased the harmonics magnitude at low current without significant change of the hysteresis width. The J_c value at low field will be checked based on the magnetization data (right now it is based on the Summers fit from the measured $J_c(B)$ of HQ01e strand with B ranging from 10 – 12 T). With a different set of conductor parameters, Auchmann *et al.* reproduced the measurement with an excellent agreement [Auchmann11].

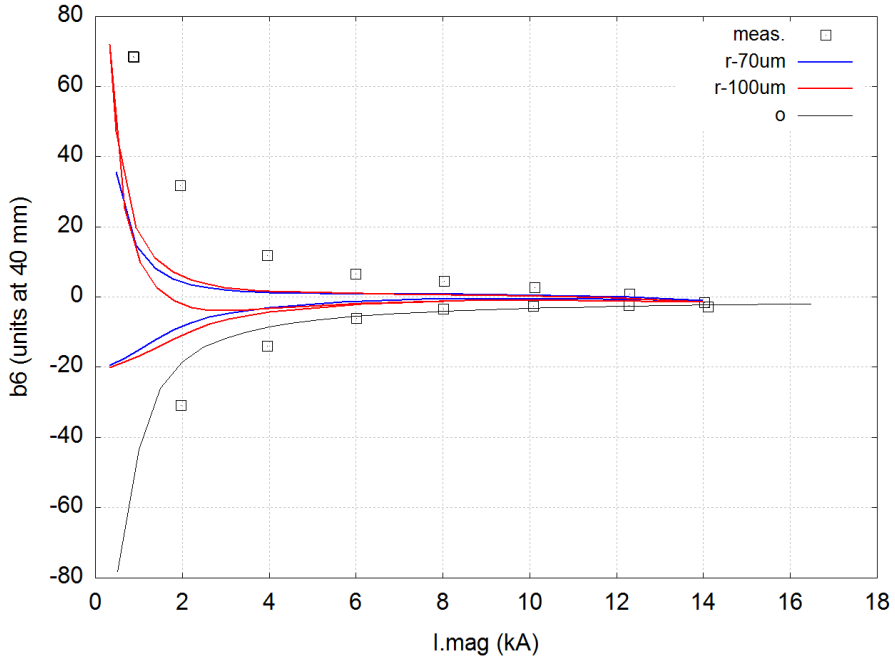

Figure 49 Calculated persistent current effect vs. measurement. Red and blue lines were from ROXIE 2D and black line was from Opera 2D. The measured data has the geometric contribution removed.

7.5 Stair-step measurement, 100 mm probe

Due to the limited LHe supply and time, measurement was done with the 100 mm probe only at 4 kA, 6 kA and 10 kA during the up ramp. The results will be included later.

7.6 Inverse analysis for the harmonics at nominal current

7.6.1 The allowed harmonics

Here we consider the possible rigid block movements to reconstruct the discrepancy between the measured and computed nominal multipoles [Redaelli00]. The allowed harmonics, b6 and b10, of HQ01e measured by the 250 mm probe at the center of the magnetic straight section at 14.096 kA were considered (Step 3). The multipoles were measured after holding the current for about 266 seconds to reduce the contribution from the dynamic effect. The computed multipoles with the cable aligned with the outer radius of the layer (ODFAC =1).

Table 19 Nominal and measured multipoles at 14 kA (R.ref = 40 mm).

	Nominal (ODFAC=1)	HQ01e	$\Delta b=b_{meas}-b_{comp}$
b_6 (unit)	-0.72	2.40	3.12
b_{10} (unit)	0.00	0.54	0.54

Only b_6 and b_{10} are considered because higher order harmonics are less sensitive to the rigid block movement (Table 44). Correspondingly, only two degrees of freedom are considered to ensure a unique solution of the linear system, $\mathbf{Jx} = \Delta\mathbf{b}$, where $\mathbf{J}$ is the matrix relating the displacement vector $\mathbf{x}$ and the resulted variation of multipole vector $\Delta\mathbf{b}$. J is determined based on the sensitivity matrix (Table 44) and

$$J_{i,j} = \frac{\Delta b_i}{\Delta x_j}.$$

We consider the following five displacement vectors.

1. (r4, φ3) – the most economic situation, i.e., the least movement with the largest multipole change. The **J** matrix is given by

   $$\mathbf{J} = \begin{bmatrix} 18.0 & -36.24 \\ -2.28 & -5.68 \end{bmatrix},$$

   where the numbers are in (unit/mm). Thus, the displacement vector corresponding to the **Δb** given in Table 19 is r4 = -10 μm and φ3 = -0.077 degree or -91 μm. We note that the maximum decrease for φ3 is 0.1337 degree or 158 μm towards the midplane.

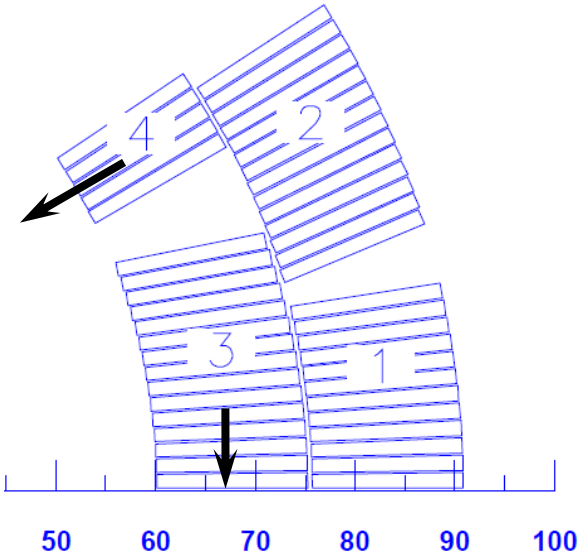

Figure 50 Qualitative representation of the displacement vector.

2. (r3, φ3) – the second economic situation.
   R3 = 11 μm, φ3=-89 μm or -0.0757 degree.
3. (φ3, φ4) – a movement can be relevant to the high Lorentz load at 14 kA.
   φ3= -0.07287364 degree and φ4= 0.01373292 degree or -86 μm and 16 μm.

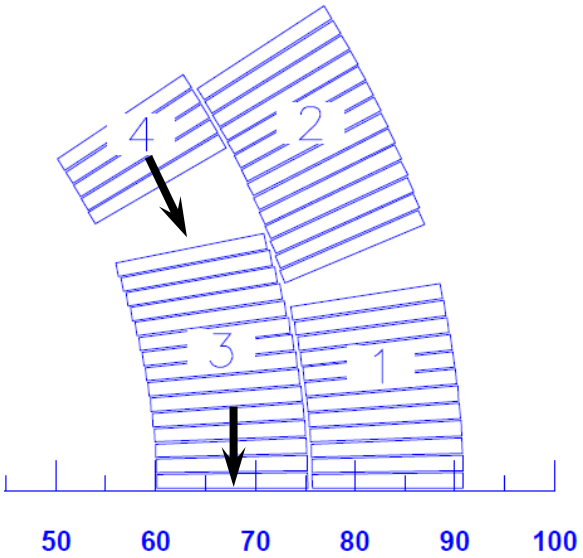

Figure 51 Qualitative representation of the displacement vector for phi3 and phi4.

4. (φ3, α3) – a movement can be relevant to the high Lorentz load at 14 kA. Due to the negative correlation between b_6 and $\alpha 3$, it can be concluded that to have positive b_6 increase, one would have negative α which is inconsistent to the trend due to the Lorentz load as shown in Figure 87. Thus, the vector displacement may not be a candidate for the measured discrepancy.
5. (r4, φ4) – a situation can be relevant to the cross section of the cut coil.
   r4=173 μm, φ4=296 μm or 0.25 degrees. The r4 was consistent with the visual check of the cross section of coil 6 which was cut after being burnout at the lead end. Show a picture of the cross section of the cut coil. The weak coupling between b_6 and φ4 has two implications, 1) the change of b_6 determines the change of r4 (or vice versa) and 2) the change of b_{10} will primarily affect φ4 given a fixed change of b_6. Thus, if the actual b_{10} was smaller than the measured one, then the change of φ4 will be smaller than 0.25 degree.

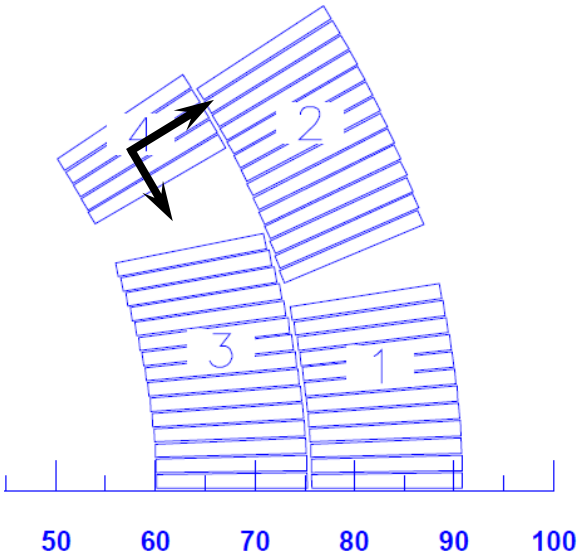

Figure 52 Qualitative representation of the displacement vector for r4 and phi4.

In conclusion, the discrepancy between the measured and computed multipoles at 14 kA can be explained by the deformation of the inner layer.

7.6.2 The non-allowed harmonics

Here we consider the non-allowed harmonics HQ01e at 14 kA measured using the 250 mm probe. Three low-order harmonics of HQ01e, a_3, b_3 and a_4, featured relevant values, similar to the LHC short straight section prototype quadrupole magnets (Table 20) [Redaelli00].

Table 20 Nominal and measured multipoles at 14 kA using the 250 mm probe (R.ref = 40 mm).

Multipole (unit)	Nominal	HQ01e	Δ=meas-comp
a3	0.00	-1.61	-1.61
b3	0.00	3.92	3.92
a4	0.00	2.13	2.13

The non-allowed harmonics can be induced by a certain asymmetry of the coil geometry. Based on the measured coil pole azimuthal strain during the current holding at 14.096 kA, one has a more pronounced left-right asymmetry (larger b_3) compared to the top-bottom asymmetry (Table 21).

Table 21 The measured coil pole azimuthal strain during the current holding at 14.096 kA (step 3).

	Coil 9	Coil 8	Coil 7	Coil 5	Distance to symmetry	
					Left-right	Top-bottom
Strain (1E-6)	-61	94	4	-159	10.2	6.1

Each of the 7 orthogonal asymmetry families listed in Table 49 induces a certain group of non-allowed harmonics. The inverse analysis of three non-allowed harmonics can be decomposed into three separate problems with each block displacement vector leading to only one harmonics. Then the vector sum of the three vectors gives the measured non-allowed harmonics.

Here two displacement vectors were identified from Table 49 inducing the non-allowed harmonics in the most economic way. The first is r3 and the second is φ3. Both are related to block 3, the inner layer block with the largest number of cables. These two parameters induce large variation of the relevant low-order harmonics.

The sensitivity is calculated as Δharmonics/Δr in unit/mm, which gives the expected radial displacement of the block given the discrepancy between the measured and nominal multipoles. The radial displacement Δr is then applied to each block based on the direction of the displacement determined by the symmetry configuration (+/-1 in Table 22). The sum of the Δr of each block derived from each harmonics is then summed up for the total Δr of each block (Table 23). Large radial displacement of 40 – 100 μm was observed for the calculated values.

Table 22 Change of r in different symmetry configuration.

	Δ	symmetry	Block #								Sensitivity	Δr
	(unit)		3	19	20	21	22	23	24	25	(unit/mm)	(μm)
a3	-1.61	2	1	1	1	1	-1	-1	-1	-1	78	-20.6
b3	3.92	3	1	1	-1	-1	-1	-1	1	1	-78	-50.3
a4	2.13	4	1	1	-1	-1	1	1	-1	-1	67.6	31.5

Table 23 Total radial displacement of each block.

	symmetry	Block #							
		3	19	20	21	22	23	24	25
a3	2	-20.6	-20.6	-20.6	-20.6	20.6	20.6	20.6	20.6
b3	3	-50.3	-50.3	50.3	50.3	50.3	50.3	-50.3	-50.3
a4	4	31.5	31.5	-31.5	-31.5	31.5	31.5	-31.5	-31.5
	∑ Δr (μm)	-39.4	-39.4	-1.9	-1.9	102.4	102.4	-61.1	-61.1
	r (mm)	59.9606	59.9606	59.9981	59.9981	60.1024	60.1024	59.9389	59.9389

Using the final radii of block 3 and the associated blocks for quadrupolar symmetry as listed in Table 23 and calculating the harmonics with ROXIE, one gets a_3 = -1.69 units, b_3 = 4.12 units and a_4 = 2.24 units (within 5% of the measured results).

Similarly, Table 24 and Table 25 show the variation in positioning angle in block 3 and other blocks satisfying the quadrupolar symmetry.

Table 24 Change of r in different symmetry configuration.

	Δ	symmetry	Block #								Sensitivity	Δφ
	(unit)		3	19	20	21	22	23	24	25	(unit/mm)	(μm)
a3	-1.61	6	1	-1	-1	1	-1	1	1	-1	-69.4	23.2
b3	3.92	7	1	-1	1	-1	-1	1	-1	1	-69.4	-56.5
a4	2.13	4	1	1	-1	-1	1	1	-1	-1	-56.4	-37.8

Table 25 Total radial displacement of each block.

	symmetry	Block #							
		3	19	20	21	22	23	24	25
a3	2	23.2	-23.2	-23.2	23.2	-23.2	23.2	23.2	-23.2

b3	3	-56.5	56.5	-56.5	56.5	56.5	-56.5	56.5	-56.5
a4	4	-37.8	-37.8	37.8	37.8	-37.8	-37.8	37.8	37.8
	∑Δφ (μm)	-71.1	-4.5	-41.9	117.4	-4.5	-71.1	117.4	-41.9
	∑Δφ (deg.)	-0.0602	-0.0038	-0.0355	0.0994	-0.0038	-0.0602	0.0994	-0.0355
	φ (deg.)	0.0735	0.1299	0.0982	0.2331	0.1299	0.0735	0.2331	0.0982

The negative Δφ means the block move towards the mid-plane and thus is subjected to the maximum azimuthal movement of 0.1337 degrees (or 158 μm). Given the geometry of the each blocks, ROXIE gives a_3 = -1.70 units, b_3=4.13 units, and a_4 = 2.24 units (within 5% of the measured results).

The two scenarios of displacement are shown in Figure 53.

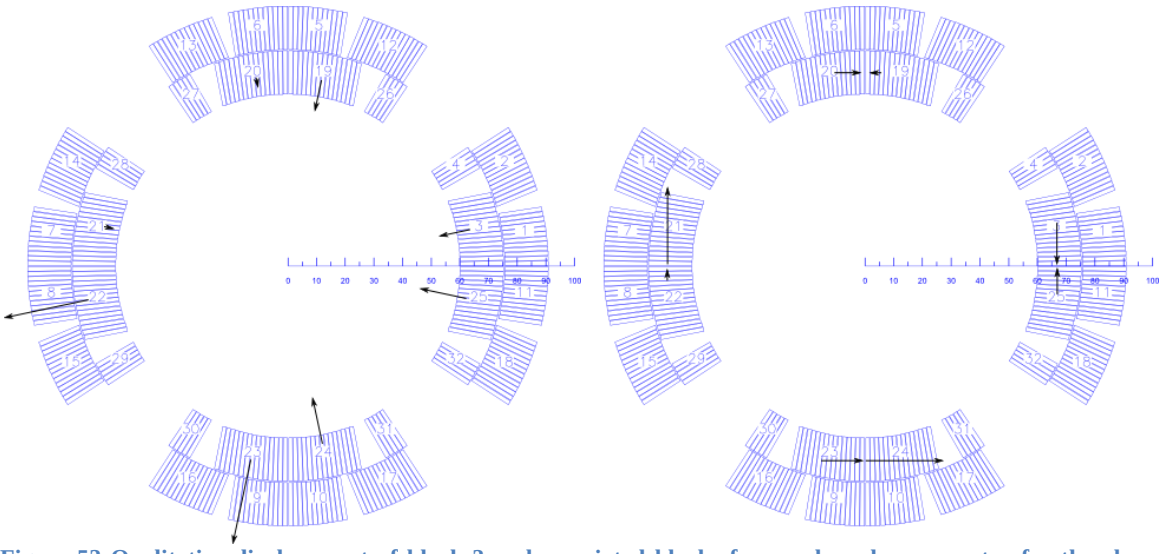

Figure 53 Qualitative displacement of block 3 and associated blocks for quadrupolar symmetry for the observed low-order harmonics. Left: radial displacement (r3). Right: positioning angle displacement (phi3).

8 Measurements with different ramp rates

Large dynamic effect was observed. This was a result of small crossover resistance and large cable width.

8.1 Measurements during training quenches

The probe was rotating at the center of the magnetic straight section (z = -75 mm) during the training ramps with a rotation speed of 0.5 Hz. This measurement in principle allowed us to study the dynamic effect with different ramp rates up to the quench current. The magnet quenched at the end, which can be considered as a cleansing quench before each measurement.

Figure 54 shows an example measured during training attempt A07. The ramp rate was 50 A/s below 7 kA, 20 A/s up to 12.2 kA, 10 A/s up to 14 kA and 5 A/s to quench. The magnet quenched at 14.84 kA. The change between the ramp rates was performed without any intermediate smoothing procedure.

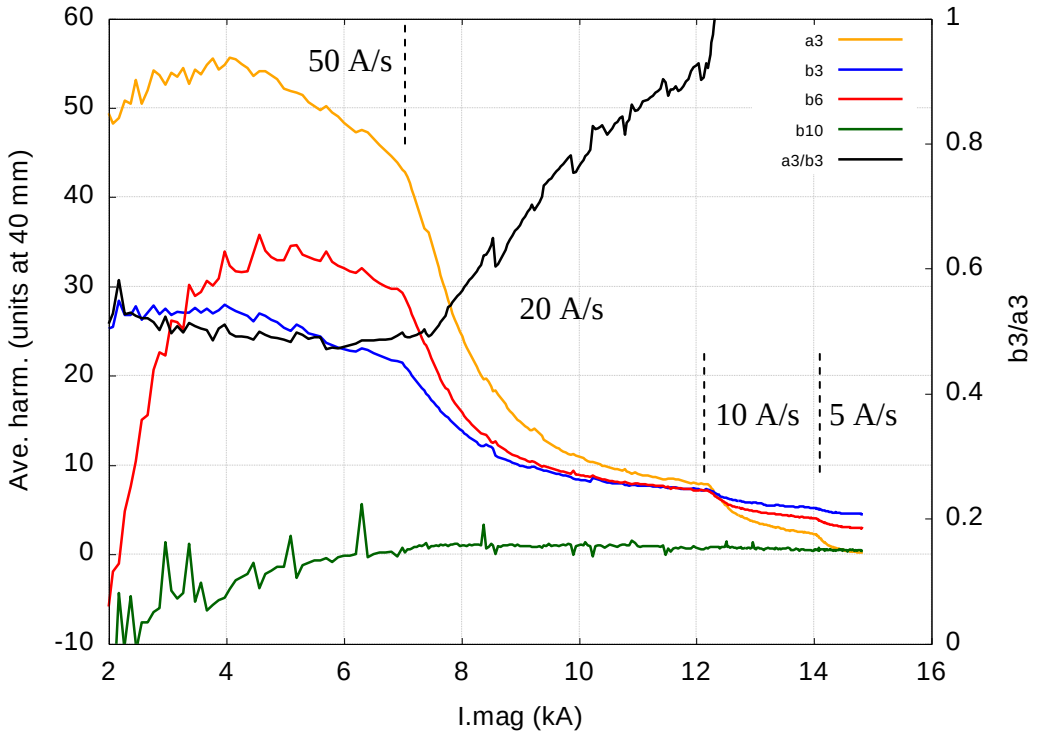

Figure 54 Normalized multipole coefficients during a training ramp (A07), 250 mm probe at z = -75 mm, reference radius 40 mm.

The behavior of a3 and b3 were contributed by at least two components, persistent current and inter-strand coupling current. Two different cables were used in HQ01d/e magnets (Table 1 and Figure 2). The top two coils (5 and 7) were wound cable 1 (108/127, effective filament diameter 50 um); the bottom two coils (8 and 9, effective filament diameter 70 um) were wound with cable 2 (54/61). Cable 1 also had a lower J_c than cable 2 at 12 T, 4.3 K (Table 1). Thus, the top two coils were expected to have a lower persistent current than that of the bottom two coils, leading to a top-bottom magnetization asymmetry. In this case, a negative a_3 was expected, consistent with the results from the stair-step measurements (Table 16 – Table 18). At high current (> 12 kA, 70% SSL), the persistent current effect is expected to be less pronounced and

the resulted a_3 should decrease with the magnet current. This was consistent with the measurement that a_3 approached to zero while b_3 and b_6 approached to a finite level (~ 4 units). The measured a_3 was positive, which may be explained by the contribution from the inter-strand coupling current.

As opposed to the persistent current, the field error due to the inter-strand current depends on the ramp rate. Ramp-rate dependence was most significant in a_3 but not obvious in b_{10}, over the entire measured current range. By dependence we mean the decay rate of the harmonics with respect to the ramp rate. For example, Δa_3 = -2.1 units and Δb_3 = -0.8 units over the same time period between 14.03 kA (81% SSL) and the quench current where the ramp rate was 5 A/s (neglecting the harmonics decay if the ramp rate was kept at 10 A/s). The stronger ramp-rate dependence of a_3 compared to b_3 may indicate that the cross-over resistance, a major source for the inter-strand coupling current, was more different between the top two and bottom two coils. This indicates that the cross-over resistance of cable 1 and 2 were different. On the other hand, coils made by the same cable had similar cross-over resistance, as indicated by the less pronounced ramp-rate dependence of b_3.

8.2 Loop measurement between 50 A and 10 kA

To study the dynamic contribution to the field quality, three loop measurements, 50 A – 10 kA – 50 A with 20 A/s, 40 A/s and 60 A/s, were performed. Prior to the 20 A/s measurement, step 5 (the down-ramp stair-step measurement) was performed without cleansing quench (Figure 55). No cleansing quench was performed at the end of the loop measurement at each ramp rate. After reaching 10 kA for each measurement, the magnet current was hold for 1 minute before ramping down. 250 mm long coil was rotating at the magnetic center during the measurements.

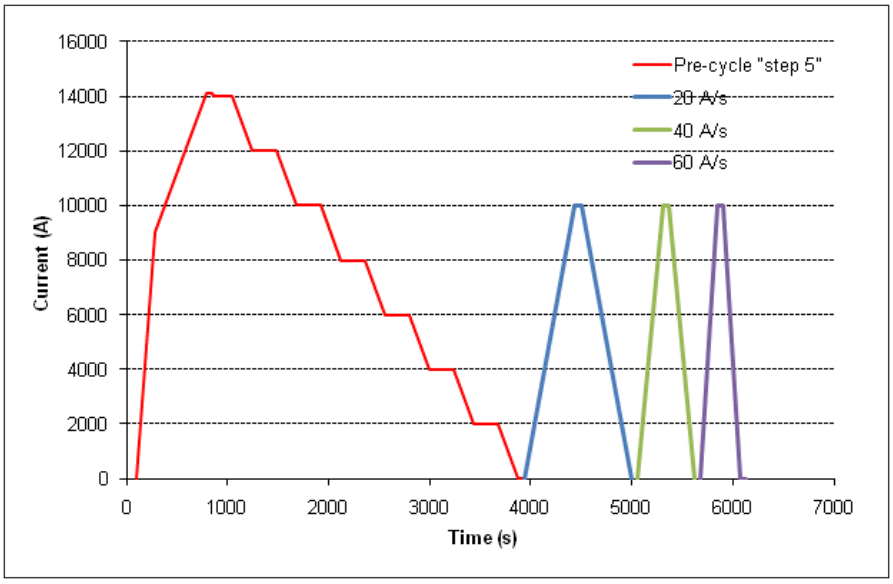

Figure 55 Current profile for the loop measurements with different ramp rates.

To be consistent with the measurements performed in HQ01d test, a peak current of 10 kA was used. As a result, the measurement with ramp rate of 80 A/s, as suggested by G. Chlachidze at the 16th LARP collaboration meeting, was not performed because the quench current at 80 A/s was expected to be slightly lower than10 kA.

Figure 56 compares the B_2 transfer function for different ramp rates. DC data were from the stair-step measurement (step 3, Figure 47). 10 A/s data were from the precycle of cycle 3 measurement. Note that there was no precycle for the 10 A/s data.

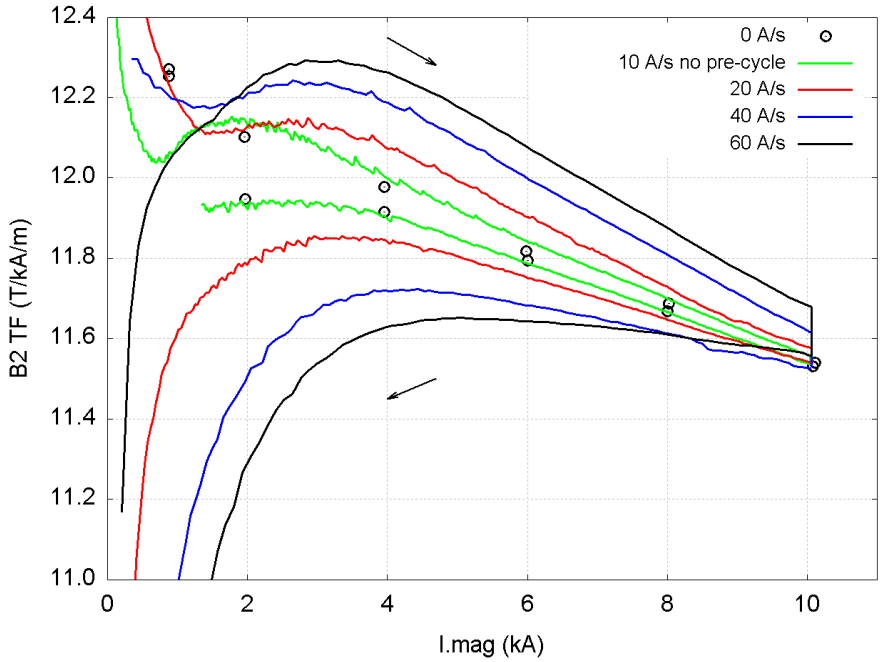

Figure 56 B_2 transfer function measured with different ramp rates. Arrows indicate the ramp sequence.

The DC result is close to that of 10 A/s. For higher ramp rates, the difference between the up- and down-ramp of the B_2 TF at the same current level becomes larger. This may be related to the field advance effect due to the inter-strand coupling currents.

Figure 57 compares the B_3 as a function of current and ramp rates and Figure 58 compares the A_3 data. DC results (black circles) were from the stair-step measurement (Step 3). To have the same polarity as the cycle measurement data (10 A/s), the polarities of the results from the other 4 ramp rates were reversed (only for the odd-order harmonics, e.g., B_3 and A_3).

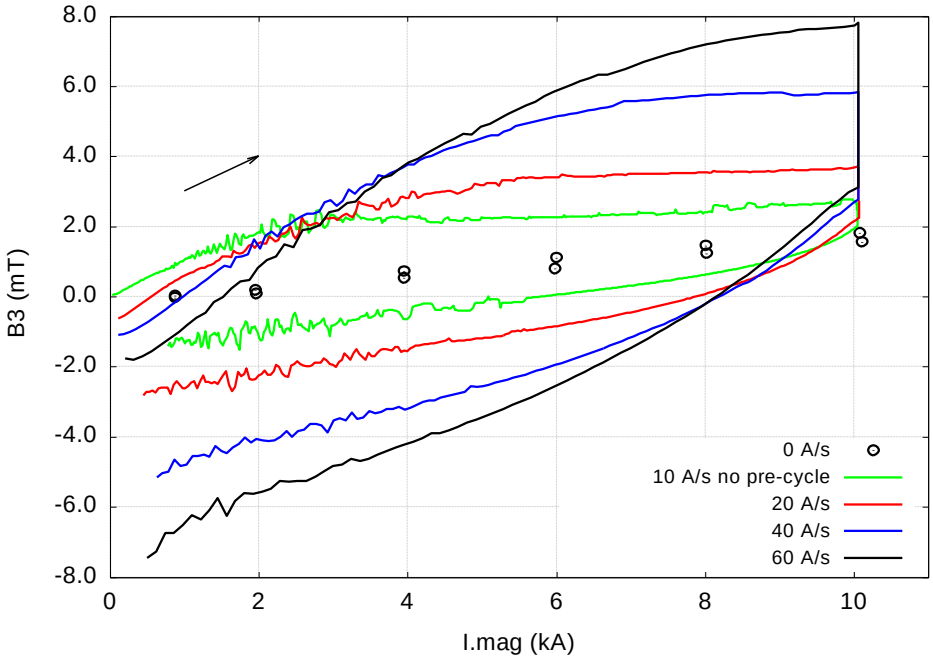

Figure 57 B_3 at different ramp rates. Arrow indicates the up-ramp branch. R_{ref} = 40 mm.

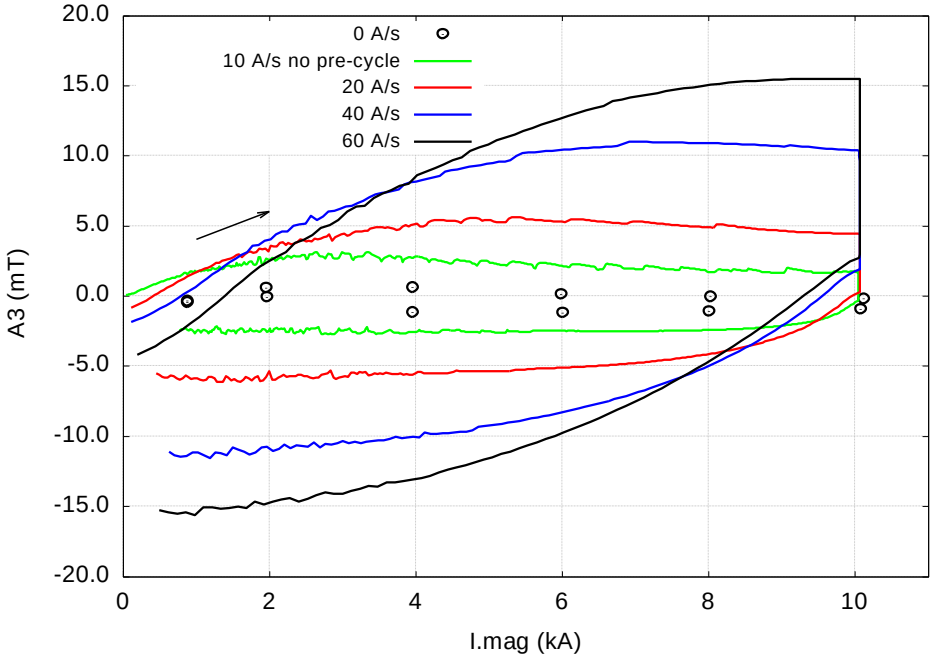

Figure 58 A_3 at different ramp rates. Arrow indicates the up-ramp branch. R_{ref} = 40 mm.

Figure 59 compares the B_6 as a function of current and ramp rates. DC results (orange) are from the stair-step measurement after the decay. Below 10 A/s, the flux density during the down-ramp was higher than that of the up-ramp for the same current, which was reversed for ramp rates higher than 20 A/s. This indicates strong effects of coupling current [denOuden97].

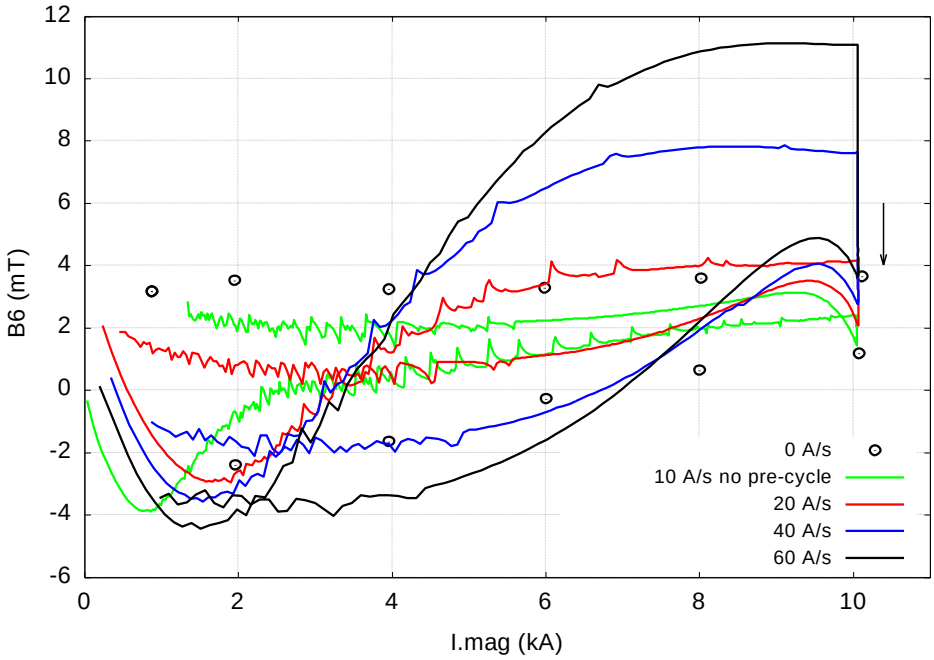

Figure 59 B_6 at different ramp rates. Arrow indicates the ramp sequence. R_{ref} = 40 mm.

The dynamic multipole, i.e., the field error due to the dynamic effect, is the difference between the multipole measured at a specific ramp rate and that measured at DC condition at the same current. Thus the DC component of the multipole, e.g., geometric and persistent current contribution, was minimized. A similar quantification of the dynamic contribution to multipole was the hysteresis width as discussed in [Ogitsu97, Velev11]. Here we consider only the up-ramp branch as the down-ramp branch was subject to the multipole decay and variation of the current holding time at 10 kA. Figure 60 shows an example of the B_3 and A_3 in mT due to ac contribution.

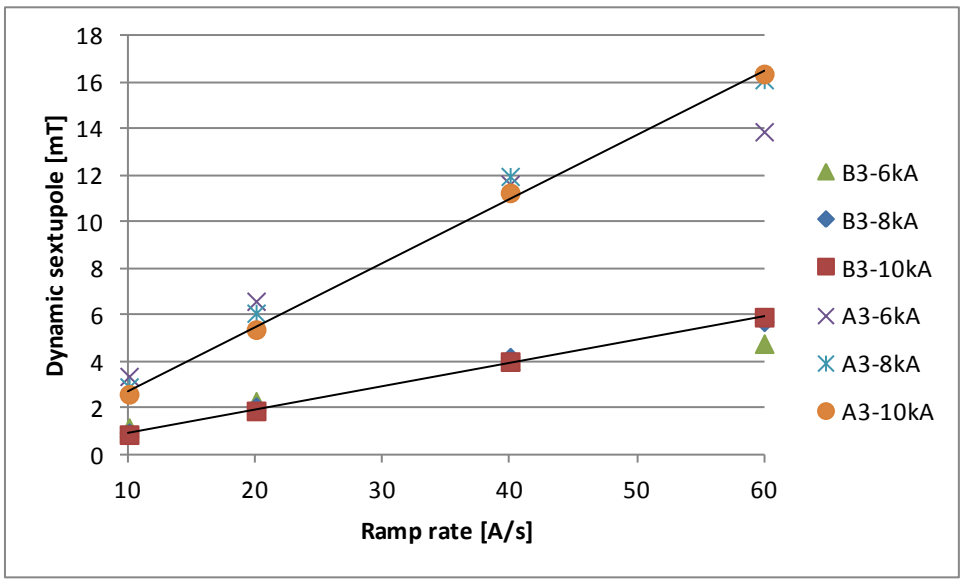

Figure 60 Dynamic B_3 and A_3 at various current levels and ramp rates. Up-ramp only. 250 mm probe at the magnetic straight section. Solid line is the linear fit of the data at 10 kA for various ramp rates. R_{ref} = 40 mm.

One sees that both the normal and skew dynamic sextupoles increase linearly with the increasing ramp rate over the measured range from 10 A/s to 60 A/s. The correlation coefficient increased typically from 0.95 at 6 kA to 1.0 at 10 kA. For multipoles of higher order, similar linear ramp-rate dependence was observed, indicating the primary source of the observed dynamic multipole was the inter-strand coupling current [Ogitsu97] which depends linearly on the ramp rate (sweep rate of $B \perp$ the cable wide surface) and the cross-over contact conductance ($G_c = 1/R_c$).

The dynamic multipole defined here is expected to vanish at 0 A/s by definition. In some cases, however, the linear fit of the measured data yielded a non-zero intercept at DC condition. One possible reason for this may be the error from the DC measurement where the time for decay was not long enough. To minimize this effect, the dynamic multipole was determined to have zero intercept at each ramp rate and current levels.

We also note from Figure 60 that at 10 kA, the amplitude of the skew sextupole tripled that of the normal sextupole for the same ramp-rate, indicating the top-bottom asymmetry in R_c was stronger than that of the left-right R_c asymmetry.

8.3 Analysis of the cross-over resistance distribution based on the measured field error

Following the idea of inverse analysis of the geometric field error [Redaelli00] and previous examples [Ogitsu97,Wolf97], we analyze the possible R_c of HQ01e based on the measured field error. The measured field error can be correlated to the cross-over conductance through **e** = **Sg**, where **e** is measured dynamic multipole vector; **S** is the sensitivity matrix; and **g** is the conductance vector in the coil on the scale of coil block or individual cable. Details of the calculation of sensitivity matrix **S** can be found in section 18. We attempt to determine the R_c based on the following scenarios.

1. Uniform R_c in a coil block.
    a. Same R_c for the coil blocks with quadrupole symmetry. Only the allowed multipoles were considered.
    b. R_c may varies from block to block. Both allowed and non-allowed multipoles were considered.
2. Uniform R_c in a cable.

For all the cases, the dynamic multipole measured at 10 kA was selected to form the vector **e** for the best measured linear dependence (Figure 60). As a result, the choice of ramp rate becomes less important as they lead to the same conductance distribution. Here 40 A/s was used, corresponding to a main-field sweep rate of 17.2 mT/s at a reference radius of 40 mm.

Table 26 lists the measured dynamic multipoles that were used to determine the R_c distribution. Due to the limited resolution, the measured normal 20-pole component was only used for the case of quadrupole symmetry. Typical uncertainty of the quoted amplitude was ± 0.05 mT – ± 0.1 mT.

Table 26 Measured dynamic multipoles (mT) at 40 A/s, 10 kA. R_{ref} = 40 mm.

B_2	B_3	B_4	B_5	B_6	B_{10}	A_3	A_4	A_5	A_6
34.85	4.3	1.06	0.51	7.47	0.18	11.54	0.47	1.06	-0.68

8.3.1 Uniform block R_c with quadrupole symmetry

Due to the small number of unknowns, the first attempt was to determine the R_c by solving the linear system **e** = **Sg**. The number of R_c that can be determined in this case is at most 3 as the dynamic multipole of only the first 3 allowed orders were used. The sensitivity matrix (section 18) indicates that the multipoles are less sensitive to the coil blocks in outer layers. Thus, we assumed $G_{c,1} = G_{c,2} = G_{c,o}$ where $G_{c,i}$ is the conductance of coil block i. The solution by solving the linear system does not always yield physically meaningful results. For example, when **e** = $\{B_2, B_6, B_{10}\}$ and **g** = $\{G_{c,o}, G_{c,3}, G_{c,4}\}$, $\mathbf{R_c}$ = {-0.01, -0.03, -0.02} $\mu\Omega$, indicating that the measured dynamic multipoles may not be explained by the R_c distribution that follows the quadrupole symmetry (for the first three allowed multipoles simultaneously).

The second attempt was to consider fewer measured dynamic multipoles and determine the R_c of the most sensitive blocks (block 3 and 4). Some physically meaningful results were obtained and listed in Table 27. In this case, the R_c averaged over a coil block (and the associated blocks for quadrupole symmetry) is ~ 0.70 $\mu\Omega$ or less. In particular, the measured dynamic B_6 can be explained by a uniform R_c of 0.30 $\mu\Omega$ in block 3 and the associated coil blocks for quadrupole symmetry. This was consistent with B. Auchmann's estimation [Auchmann11].

Table 27 Uniform R_c values ($\mu\Omega$) of coil block 3 and block 4 with quadrupole symmetry.

		Dynamic multipole vector **e**					
Number of unknowns		$\{B_2\}$	$\{B_6\}$	$\{B_{10}\}$	$\{B_2, B_6\}$	$\{B_2, B_{10}\}$	$\{B_6, B_{10}\}$
1	$R_{c,3}$	0.50	0.30	-			
	$R_{c,4}$	0.05	-	0.67			
2	$R_{c,3}$				-	0.68	-
	$R_{c,4}$				-	0.20	-

8.3.2 Uniform block R_c

Block R_c is again assumed to be uniform within one block but can vary between blocks. Accordingly, the number of Gc to be determined is 32, same as the number of coil block. The sensitivity matrix involving 32 coil blocks and their contribution to the selected multipoles was determined (see section x for more details). The number of the measured dynamic multipoles to be used here is less than the number of unknowns. We follow the same optimization procedure used in [Wolf97, Ogitsu97] to determine the possible distribution of R_c over the coil blocks. The general idea is to obtain the R_c distribution that minimizes the following two functions simultaneously: 1) the discrepancy between the measured and calculated dynamic multipoles; and 2) the variation between of R_c between the coil blocks. In addition, Gc is positive for all blocks.

The first function is given by $(\mathbf{e}_m - \mathbf{e}_c)^2$ where e is the measured or calculated dynamic multipole vector. The calculated dynamic multipoles is given by $\mathbf{e}_c$ = **Sg** where **S** is the sensitivity matrix and **g** the vector of the Gc distribution. The second function is given by the variance of G_i, i.e., $\frac{1}{N-1}\left(G_i - \frac{\sum G_i}{N}\right)^2$, where N is the number of unknown Gc. To simultaneously minimize both, we

minimize the sum of both functions as $F = (\mathbf{e}_m - \mathbf{e}_c)^2 + \frac{w}{N-1}\left(G_i - \frac{\sum G_i}{N}\right)^2$ where a weighing factor, w, is applied to the squared deviation term. By changing the weighing factor, the contribution of the two functions to the objective function F can be varied. For example, when w = 0, we obtain an R_c distribution that yields the dynamic multipoles closest to the measurement. We note function F can be formulated in a matrix form that fits for the quadratic programming.

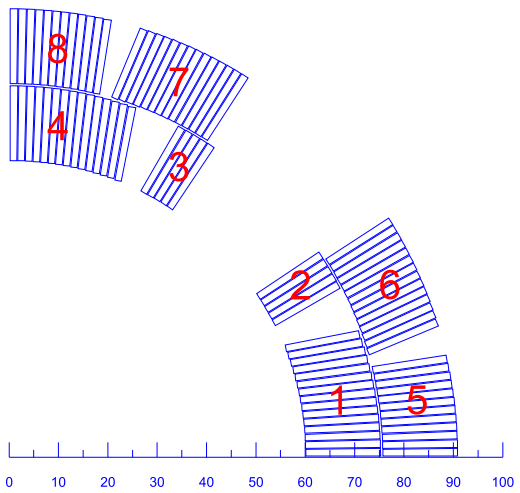

Figure 61 The block numbering (index) for G_c distribution in one coil (block level). Rotate anti-clockwise to obtain the indices for the other three coils.

We apply the constraint on G_c to be within 0.1 MS to 50 MS, corresponding to a R_c range between 0.02 $\mu\Omega$ to 10 $\mu\Omega$. Figure 62 shows the R_c of each block of each coil obtained by the optimization procedure. Except blocks 2 and 3 in each coil, all the other coil blocks have a R_c lower than 0.6 $\mu\Omega$ (Figure 63). In addition, blocks 1 and 4 in coils 5 and 7 have a higher R_c than those in coil 8 and 9 (Figure 63).

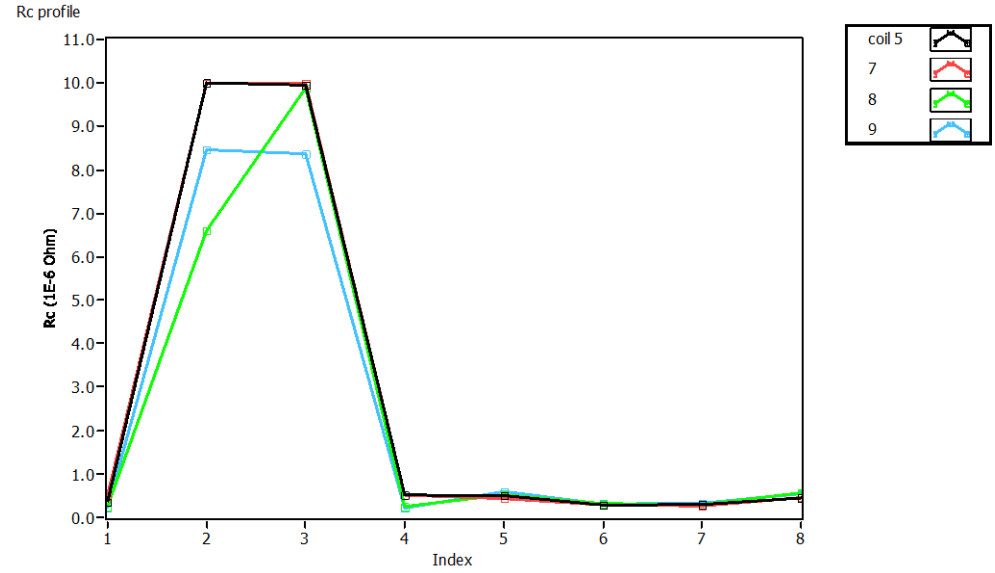

Figure 62 Coil block R_c value of each coil with w = 1. The index number is illustrated in Figure 61.

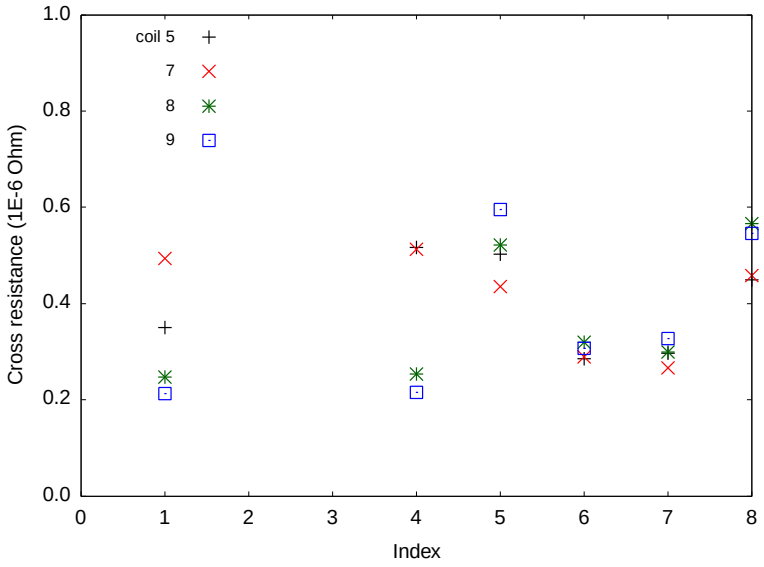

Figure 63 Zoom-in of case with w = 1.

The extreme R_c values shown in Figure 62 were due to the lower bounds set on G_c during the optimization. By increasing the weighting factor and minimizing the variation of G_c between coil blocks, a more uniform G_c profile can be obtained and Figure 64 shows the R_c profile with w = 10.

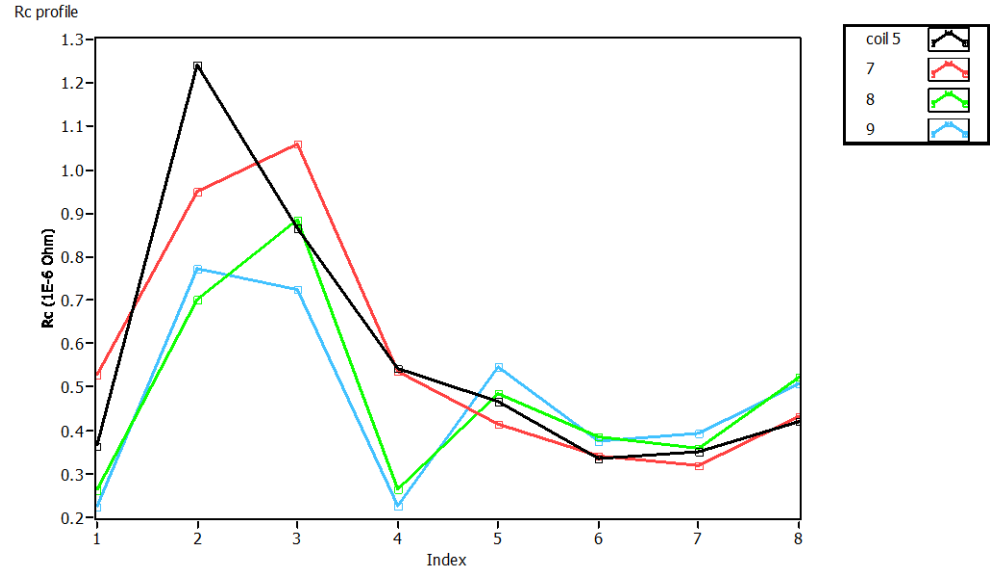

Figure 64 Coil block R_c value of each coil with w = 10.

Note that even though the numerical values of R_c in block 2 and 3 were reduced with higher value of weighting factor, as expected, the values of the other blocks did not change significantly between the cases of w =1 and w = 10 (Figure 63 and Figure 64). This is important as the multipoles are sensitive to coil blocks 1 and 4 of the inner layer and their values vary little with the weighting factor.

The cost of a larger weighting factor is the higher error between the measured and calculated dynamic multipoles. For example, the error of B6 increased from 7% to 30% when w increased from 1 to 10 (Table 28). The increase of the error in other multipoles was not as significant.

Table 28 Measured and calculated dynamic multipole with different weighting factors.

	Meas. (mT)	Calc. (mT)	
		w = 1	w = 10
B2	34.85	34.90	35.02
B3	4.30	4.29	4.23
B4	1.06	1.06	1.03
B5	0.51	0.51	0.49
B6	7.47	6.98	5.13
A3	11.54	11.51	11.29
A4	0.47	0.47	0.46
A5	1.06	1.06	1.04
A6	-0.68	-0.67	-0.61

8.3.3 Uniform cable R_c in block groups 3 and 4

As demonstrated by the sensitivity matrix calculation (section 18), the inner layer, especially coil block 3, impacts the dynamic multipole more than the outer layer, similar to the geometric multipole case. The outer layer generally sees less perpendicular field yielding less inter-strand coupling currents. Thus, we increase the resolution to the cable level for the inner layer while maintain the uniform block R_c in the outer layer. The same approach was also used in [Wolf97, Ogitsu97]. As a result, the number of variables increased from 8 to 44 per coil (Figure 65).

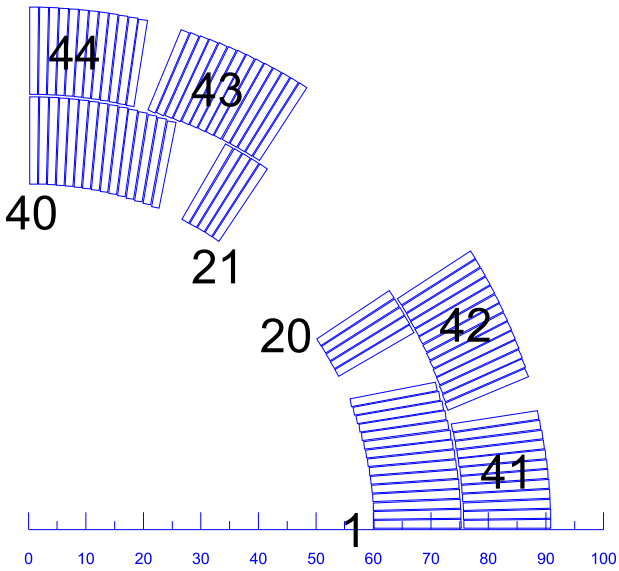

Figure 65 The block numbering (index) for G_c distribution in one coil (cable level). Rotate anti-clockwise to obtain the indices for the other three coils.

The dynamic multipoles measured by the 250 mm probe rotating at the magnetic straight section with a reference radius of 40 mm were used. The weighting factor was set to 1. Figure 66 shows

the calculated R_c values as a function block index. From the amplitude of the R_c values, one sees that the estimated R_c values fall between 0.2 $\mu\Omega$ and 0.7 $\mu\Omega$ in cables of the inner layer, much less than the 10 $\mu\Omega$ target for the LHC magnet cables [Verweij94]. Coil 5 and 7 showed a higher R_c than coil 8 and 9, consistent with the calculation results with uniform block R_c. This may be related to the fact that the coils were wound with two different cables (Table 1). In this case, the 108/127 cable used in coils 5 and 7 showed a higher R_c values than the 54/61 cables used in coils 8 and 9.

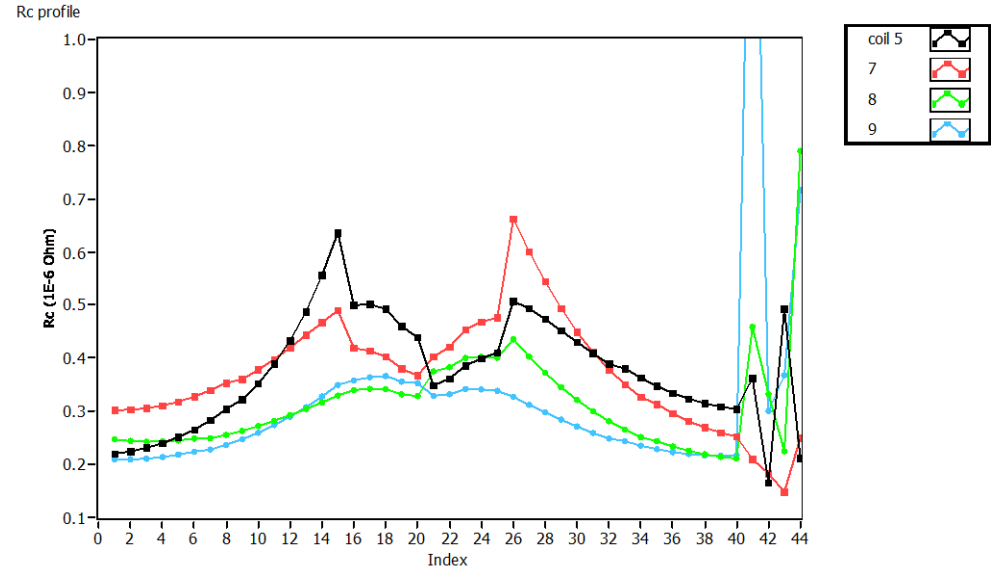

Figure 66 The estimated cross resistance ($\mu\Omega$) in each coil (1D index graph). 250 mm probe at the straight section. w = 1. R_{ref} = 40 mm.

Cable 1000R, winding the coil 5 and 7, had a stronger oxidization than cable 996CR after cable anneal (Figure 67). Oxidization was observed on both outside and inside of cable 1000R. The oxide layer increases R_c but the curing process and coil heat treatment following the magnet winding can significantly change the initial R_c contributed by the oxide layer [Richter97]. Thus, we point out the different oxidization condition of the cable without drawing any further conclusion regarding its role in R_c estimated based on the cold measurement data.

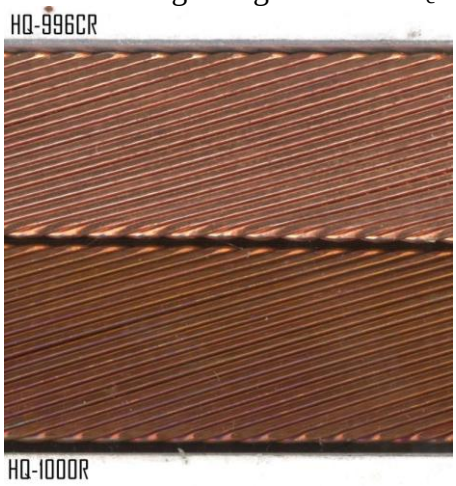

Figure 67 Outer surface of cable 996CR and 1000R after cable anneal. Cable 1000R (108/127, bottom) had a darker color due to the oxidization (picture taken by H. Higley and N. Liggins at LBNL).

The same R_c value can be plotted on the coil cross section, as shown in Figure 68 where a color code represents a R_c value in $\mu\Omega$. The inner layer R_c tends to decrease toward the mid-planes. The lower R_c yields higher AC loss during the ramping and may contribute to the observed mid-plane quenches during the test [Martchevsky11].

Meanwhile, the R_c values tend to increase toward the wedge and decrease again toward the pole island. The larger thermal contraction of the wedge compared to the Titanium pole island from room temperature to 4.4 K may pose less pressure perpendicular to the cable wide surface and lead to a higher R_c. A stronger top-bottom asymmetry compared to the left-right asymmetry was also observed from the R_c pattern on the coil cross section. This was consistent with stronger ramp-rate sensitivity in a_3 than b_3 as seen in Figure 54.

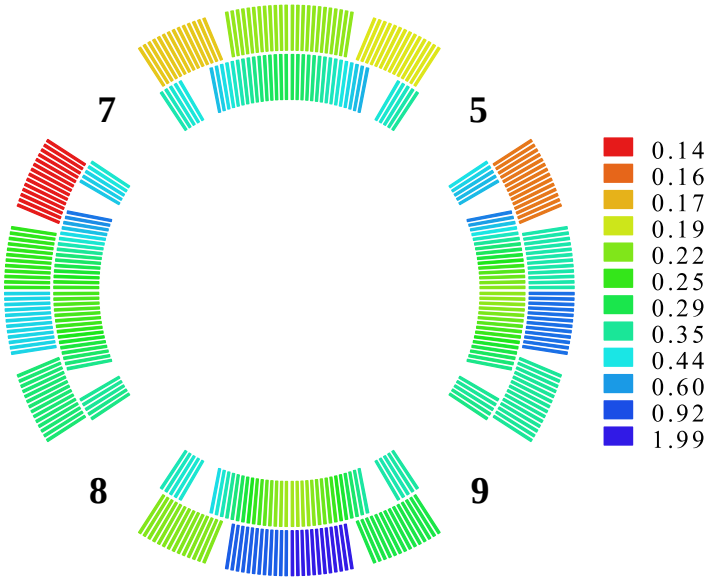

Figure 68 The estimated cross resistance ($\mu\Omega$) in each coil (2D color map). 250 mm probe at the straight section. w = 1. Rref = 40 mm.

The calculated dynamic multipole based on the estimated R_c and the sensitivity matrix agreed well (< 2% relative error) with the measured values (Table 29).

Table 29 The measured and calculated dynamic multipole (mT). 250 mm probe at the magnetic straight section, R.ref = 40 mm.

	Meas.	Calc.
B2	34.85	34.86
B3	4.30	4.29
B4	1.06	1.05
B5	0.51	0.51
B6	7.47	7.35
A3	11.54	11.51
A4	0.47	0.47
A5	1.06	1.06
A6	-0.68	-0.67

9 Rise-and-decay fluctuations

Rise-and-decay fluctuations of multipoles during the current ramping were observed in the results from both probes. It was also observed in the HQ01d magnetic measurement. Examples of the fluctuations during the up ramp of cycle 3 measurement are shown in Figure 69. About 10 to 25 data points were acquired for each fluctuation. The fluctuation was not only seen in the allowed multipole but also non-allowed normal and skew multipoles, even though their "rise-and-decay" patterns were not exactly the same. As an example, the fluctuation occurred 3820 s (Figure 69) showed that the time constant for the decay of the B_6 fluctuation (~ 9 s, blue line points) was less than that of A_3 (~ 30 s, black line). In general, the amplitude of the fluctuations decreased with increasing current.

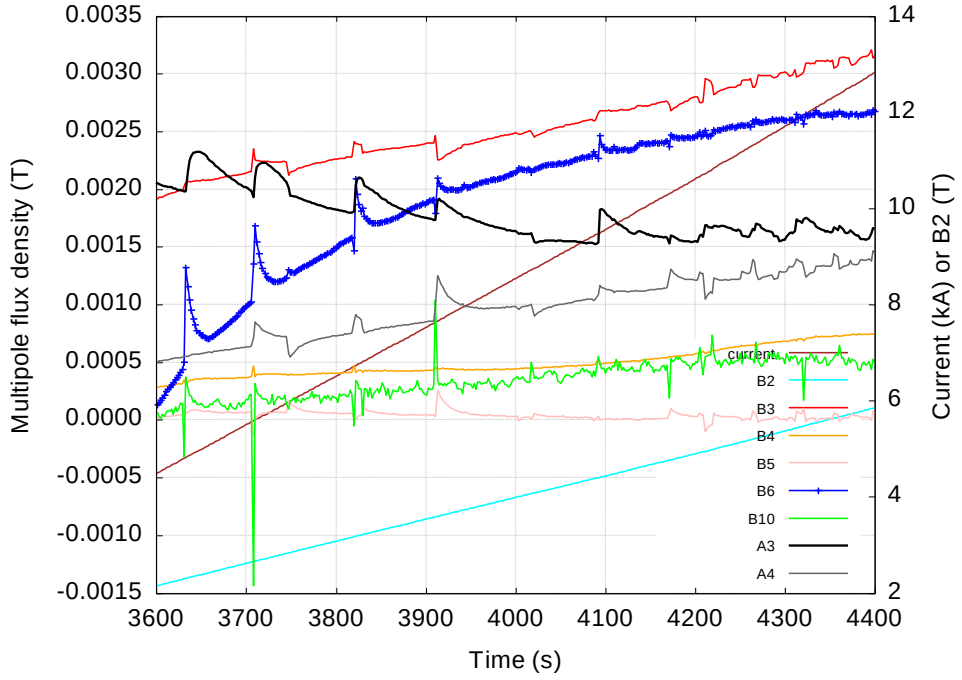

Figure 69 Rise-and-decay fluctuations of low-order normal and skew multipoles and normal B_6 and B_{10} during the up-ramp in cycle 3. Magnet current averaged every rotation and the main field are plotted at the secondary y-axis.

No obvious fluctuation was observed in the main field B_2. On the other hand, if fluctuations similar to those shown on the multipoles did occur in the main field, they may not be easily detectable as the amplitude of the main field was 3 orders larger than that of the fluctuation shown in the multipoles (secondary y-axis of Figure 69). As a result, the fluctuations of the multipoles still exist on the multipoles after being plotted against the main field B_2 (Figure 70).

It was firstly thought that the multipole fluctuation was related to the flux jump typically seen in Nb_3Sn magnet as both tend to occur at low field/current and become suppressed with increasing current. However, the flux jump may not explain the long period of the multipole fluctuation. P. Ferracin and L. Bottura, among others, first raised the power supply behavior as a possible cause for the observed multipole fluctuation. The current profile recorded during each probe rotation was checked and a correlation between the fluctuation and irregular current profile was identified.

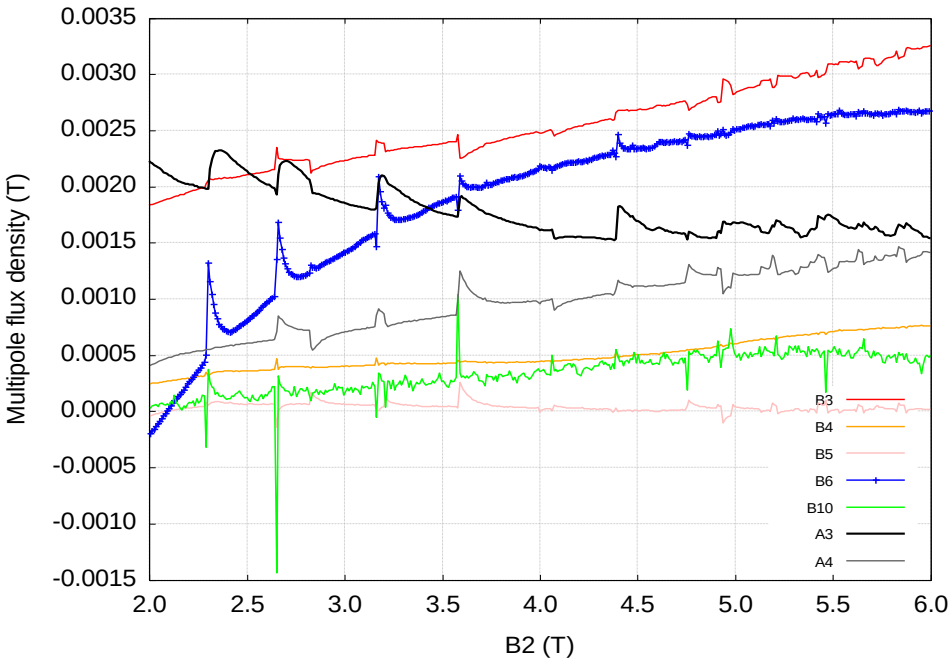

Figure 70 Fluctuation as a function of main field B_2. Same multipole data as shown in Figure 69.

Before showing a few examples of the current profile corresponding to the multipole fluctuation, we first remember that for each probe rotation, the magnet current was acquired with 4096 samples triggered by the encoder index signal. A typical rotation took 2 s. The shunt voltage, after being amplified, was digitized by an NI 6221 board with 16-bit of resolution. The recorded current was noisy (red curve in Figure 71) so a 3-moving average was used to filter the raw current data. The averaged data shown in Figure 71 (blue curve) was a result of 200 times of averaging. The ramp-rate based on the averaged data was ~ 10 A/s, as expected. Thus, the averaging was considered effective and the same procedure was used to generate the current profiles to be shown in the following discussion.

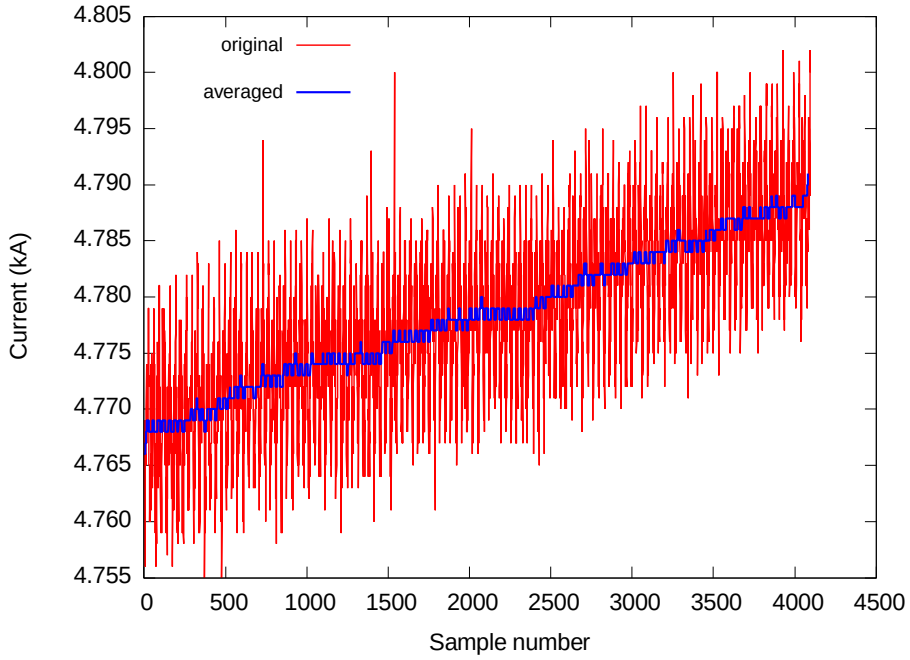

Figure 71 The recorded magnet current during one rotation of the probe (rotation 1804 of cycle 3). Red: raw data; blue: 3-moving averaged data for 200 times.

Figure 72 shows the first fluctuation of B_6 (between 3600 s and 3700 s in Figure 69) as a function of probe rotation number. The fluctuation started from rotation 1805, peaked at rotation 1806, and decayed in the following 15 rotations.

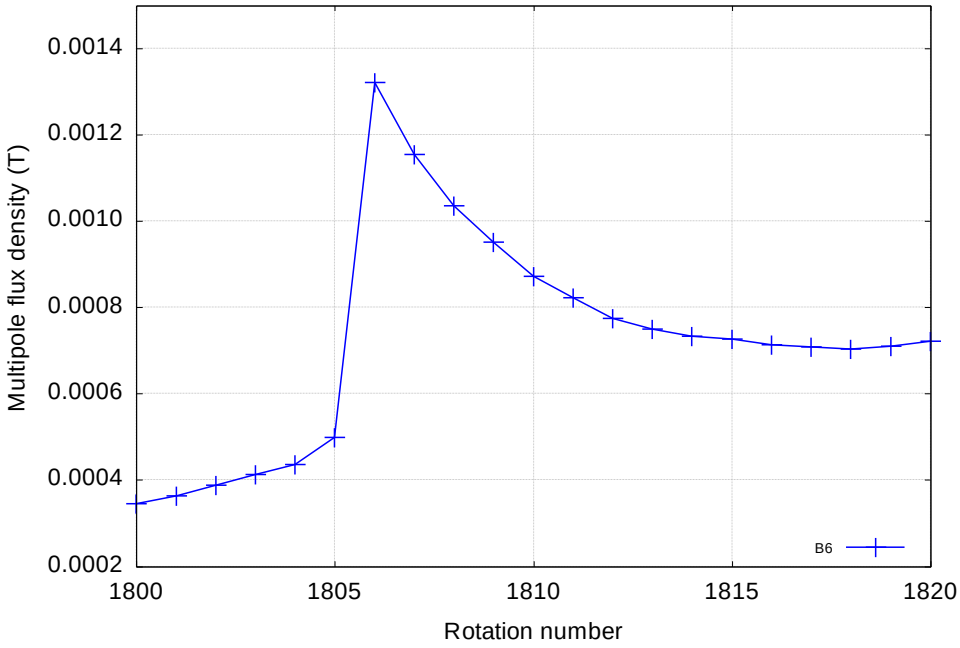

Figure 72 A fluctuation of B6 recorded during Cycle 3.

Table 30 lists the four rotations with respect to the fluctuation. We compare the current profiles and associated induced voltage from the windings of the rotating probe.

Table 30 Four rotations for fluctuation study.

	Rotation #	Remarks	Ramp rate
1	1802	before the fluctuation	~ constant, 10 A/s
2	1805	initial fluctuation	-100 A/s at the end of rotation
3	1806	fluctuation peak	varying
4	1808	fluctuation decay	~ constant, 10 A/s

Figure 73 – Figure 76 show the current profiles of the selected rotations (after being averaged for 200 times). Constant ramp rates ~ 10 A/s over the whole rotation were observed for the rotations before the multipole fluctuation (Figure 73) and during the decay of the fluctuation (Figure 76). The current at the end of rotation 1805 dropped with a rate over -100 A/s (Figure 74), followed by varying ramp rates in the next rotation (1806) when the multipole fluctuation peaked (Figure 75). After the fluctuation peaked, the ramp rate recovered to the constant 10 A/s over the entire rotation (Figure 76). A sudden change of the instantaneous ramp rate of the magnet current was observed when the B_6 rose.

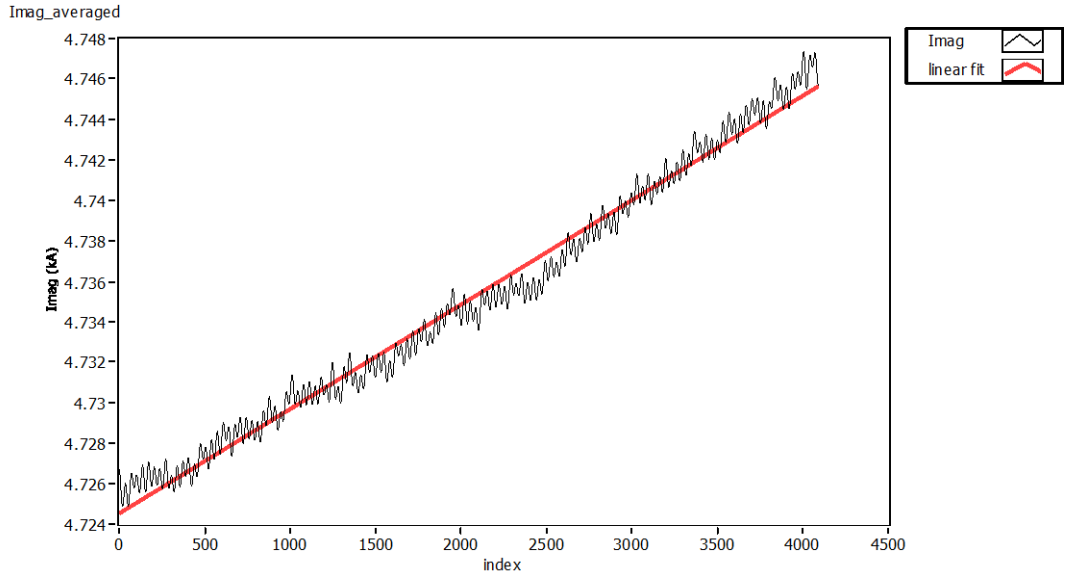

Figure 73 Current profile of rotation 1802, Cycle 3, no multipole fluctuation observed during this rotation. Red line is the linear fit of the averaged measurement (black line).

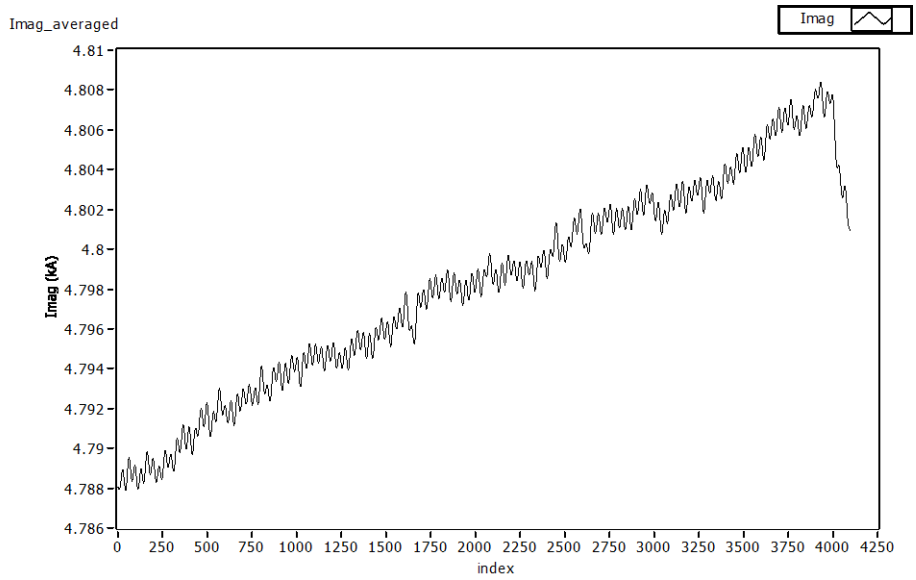

Figure 74 Current profile during rotation 1805, Cycle 3, initial fluctuation.

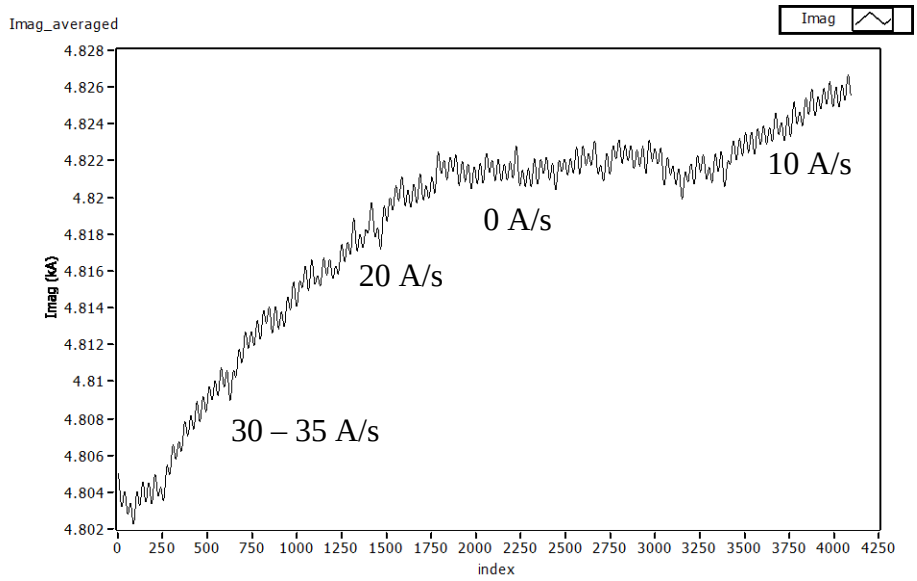

Figure 75 Current profile of rotation 1806, Cycle 3, fluctuation peaked during this rotation. Varying ramp-rates observed.

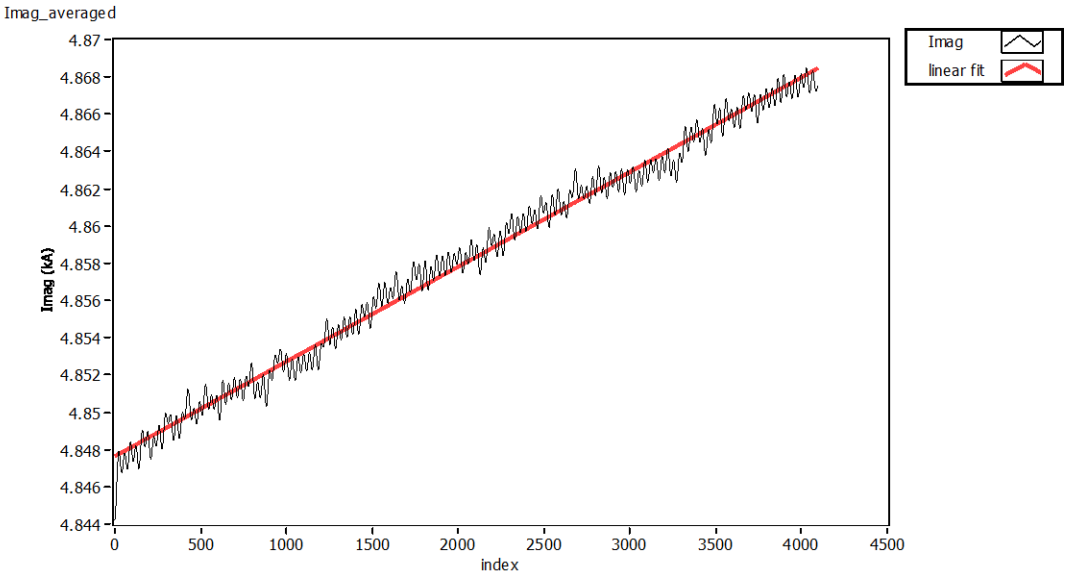

Figure 76 Current profile of rotation 1808, Cycle 3, fluctuation decayed during this rotation.

The relationship between the irregular ramp rates and the fluctuation of multipoles also was observed for other fluctuations. If irregular ramp rates occurred during one probe rotation, the multipole of the same rotation and neighboring rotations in general formed a fluctuation. Thus, the multipole fluctuation during the ramping was not an intrinsic or independent magnet behavior but was at least coupled to the current source. The multipole fluctuation always occurred during the current ramping. One explanation is that the fluctuation of the multipoles was due to the additional coupling currents induced by the sudden change of ramp rate.

A fluctuation was observed in the induced voltage of both the unbucked and the dipole-quadrupole-bucked windings of the rotating probe at the same time for rotation 1805 (Figure 77 and zoom-in in Figure 78). The time of the voltage spike was similar to when the current drop started. No similar voltage spike was observed in other multipole fluctuation cases.

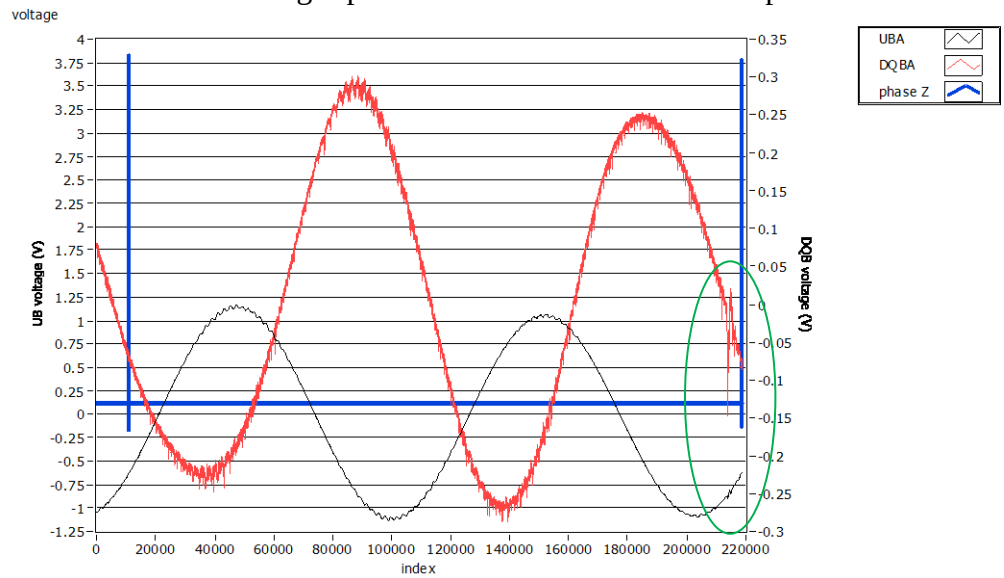

Figure 77 Induced voltage from the Unbucked and Dipole-Quadrupole-bucked windings. Rotation 1805 Cycle 3. A voltage fluctuation occurred at the end of the rotation.

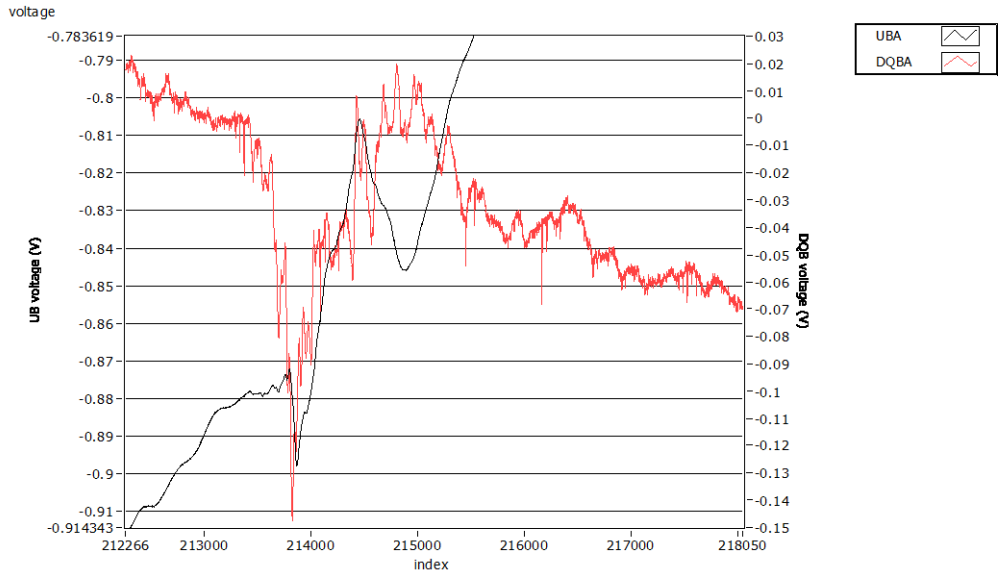

Figure 78 Zoom in of the fluctuation in the rotating coil. Rotation 1805, Cycle 3.

The voltage fluctuation of the unbucked signal was ~ 10 mV peak to peak (gain of 10 considered) and was ~ 5% of the peak-to-peak amplitude of the UB signal. The fluctuation for the DQB signal was 0.16 mV peak to peak (gain of 1000 considered) and was ~ 25% of the peak-to-peak amplitude of the DQB signal.

10 Comparison with HQ01d

10.1 Multipoles at nominal current

In HQ01d, a stair-step measurement was performed with the 250 mm probe (A37). A few differences between the HQ01d and HQ01e (step 3) measurements:

1. HQ01d: The peak current was 13.4 kA (77% I_{ss} at 4.4 K). The ramp rate between the current levels was 20 A/s. HQ01e: 14096 A, 10 A/s between the steps.
2. The 250 mm probe was rotating at z = -70 mm in HQ01d instead of z = -75 mm in HQ01e.

Table 31 Mulitpole coefficients at the end of the current holding at ~14 kA for HQ01e and 13.4 kA for HQ01d, 250 mm probe, reference radius = 40 mm.

250 mm probe		order	3	4	5	6	7	8	9	10
Normal	HQ01e	266 s	3.92	0.85	-0.11	2.40	0.78	-0.09	0.01	0.54
	HQ01d	252 s	2.31	0.77	0.33	2.28	0.51	-0.28	0.48	-0.02
	b(e)-b(d)		**1.61**	0.08	-0.44	0.12	0.27	0.19	-0.47	0.56
Skew	HQ01e	266 s	-1.61	2.13	-0.84	-0.33	0.47	0.05	-0.16	0.07
	HQ01d	252 s	0.04	4.56	-0.71	-0.30	0.61	-0.16	0.46	0.56
	a(e)-a(d)		**-1.65**	**-2.43**	-0.13	-0.03	-0.14	0.21	-0.62	-0.49

A stair-step measurement was also performed with the 100 mm probe (PQ13). A few differences between the HQ01d and HQ01e (cycle 5) measurements:

1. The peak current was 13.4 kA (77% I_{ss} at 4.4 K) for HQ01d measurement. The ramp rate between the current levels was 20 A/s. HQ01e: 14169 A.
2. The 100 mm probe was rotating at z = -70 mm in HQ01d instead of z = -75 mm in HQ01e.
3. HQ01d holding time was ~ 370 s at z = -70 mm while for the HQ01e data here it was ~ 72 s.

Table 32 Mulitpole coefficients at the end of the current holding at ~14 kA for HQ01e and 13.4 kA for HQ01d, 100 mm probe, reference radius = 40 mm.

100 mm probe		order	3	4	5	6	7	8	9	10
Normal	HQ01e	72 s	5.25	1.19	-0.01	3.17	0.63	-0.29	-0.11	0.97
	HQ01d	370 s	3.18	0.80	0.25	3.76	0.61	-0.27	-0.12	1.73
	b(e)-b(d)		2.07	0.39	-0.26	-0.59	0.02	-0.02	0.01	-0.76
Skew	HQ01e	72 s	-0.80	2.08	-1.38	-0.20	1.05	0.02	0.13	0.53
	HQ01d	370 s	-0.23	4.24	-1.46	-0.12	0.82	0.12	0.44	4.28
	a(e)-a(d)		-0.57	-2.16	0.08	-0.08	0.23	-0.10	-0.31	-3.75

The normal and skew multipole coefficients, as listed in Table 31 and Table 32, were reported in Figure 79 and Figure 80, respectively. In general, the harmonics agreed between HQ01d and HQ01e, except that

1. $|b_3|$ in HQ01e was ~ 2 units higher than that of HQ01d.
2. $|a_3|$ in HQ01e was 1 – 1.5 units higher than that of HQ01d.
3. $|a_4|$ in HQ01e was ~ 2 units lower than that of HQ01d.

The difference may be related to change of shim thickness introduced to HQ01e.

In addition, the results from the 100 mm probe generally agreed with those from the 250 mm probe within 1 unit, except in b_6, b_{10} for the HQ01d case. The a_{10} of 4.28 units in HQ01d was an outlier, which is not understood.

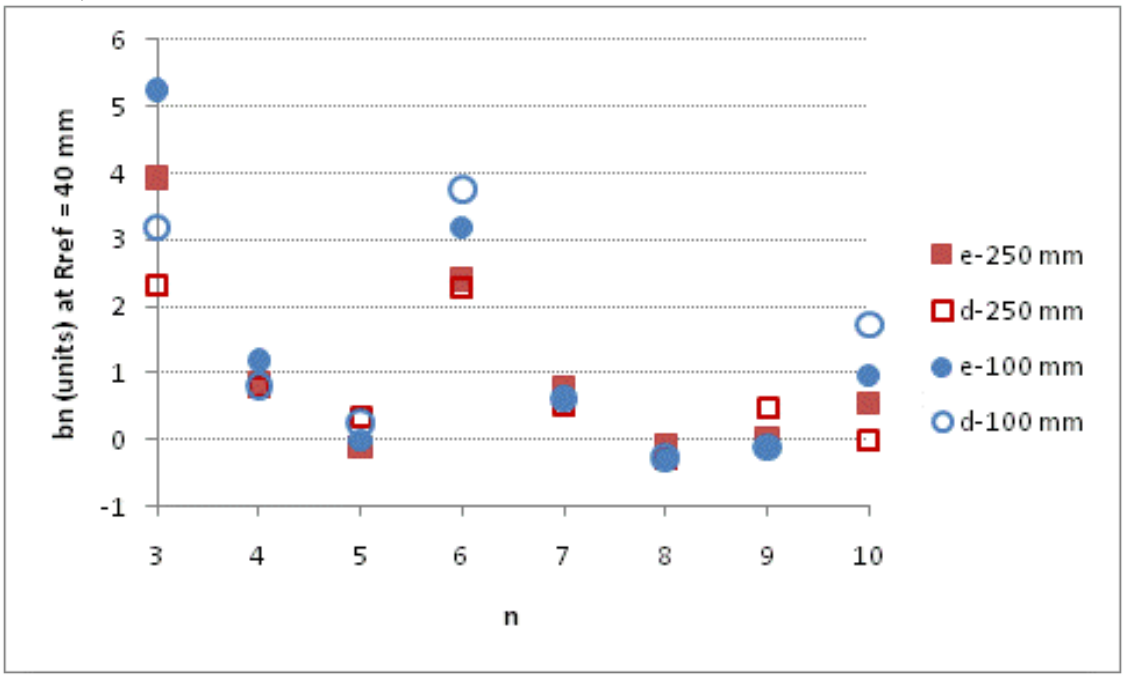

Figure 79 Normal multipole coefficients for HQ01d (13.4 kA) and HQ01e (14.2 kA), both probes, reference radius = 40 mm.

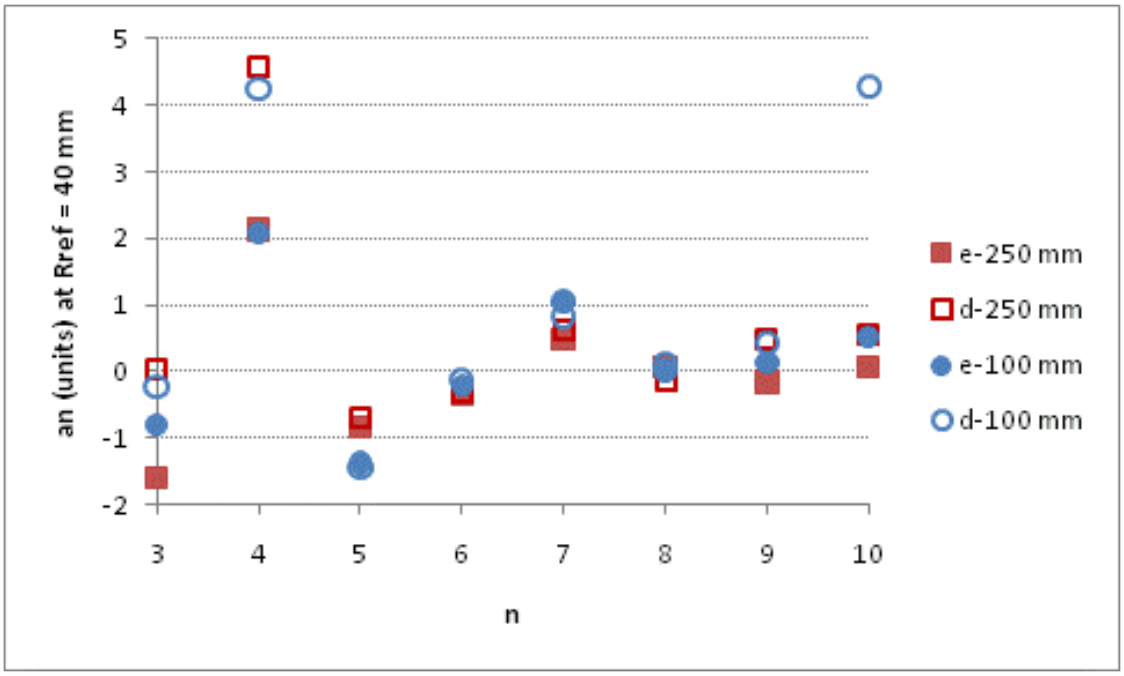

Figure 80 Skew multipole coefficients for HQ01d (13.4 kA) and HQ01e (14.2 kA), both probes, reference radius = 40 mm.

10.2 Non-allowed harmonics

Different low-order harmonics, a_3, b_3 and b_4, were observed between HQ01d at 13.4 kA and HQ01e at 14 kA. The change of these harmonics may point to the change in the coil symmetry at the nominal current level. One of the major changes from HQ01d to HQ01e is the 1) increase of the overall pre-stress of 25 MPa and 2) different shimming configuration to reduce spread in the pre-stress [Ferracin11]. To understand if the variation of the low-order harmonics was related to this mechanical change, we compare the displacement vector that is possible for the measured low-order harmonics between the two magnets. First we make the following two assumptions for the magnetic measurements yielding the harmonics to be compared: 1) Similar pre-stress applied during the cooldown and Lorentz load during the excitation on both magnets and hence the coil symmetry can be traced back to the room-temperature loading and shimming procedure 2) the effect of different quench history on the coil block before the magnetic measurements between these two magnets quenches are neglected.

Similar inverse analysis was performed on the low-order non-allowed harmonics observed for HQ01d [HQ01d]. We focus on the rigid radial block displacement and compare them in Table 33 because the radial displacement seems to be a more possible result of the shims of different thickness.

Table 33 Total radial displacement in μm of each block: HQ01e vs. HQ01d.

Magnet	Block #							
	3	19	20	21	22	23	24	25
HQ01d	37.8	37.8	-37.8	-37.8	97.1	97.1	-97.1	-97.1
HQ01e	-39.4	-39.4	-1.9	-1.9	102.4	102.4	-61.1	-61.1

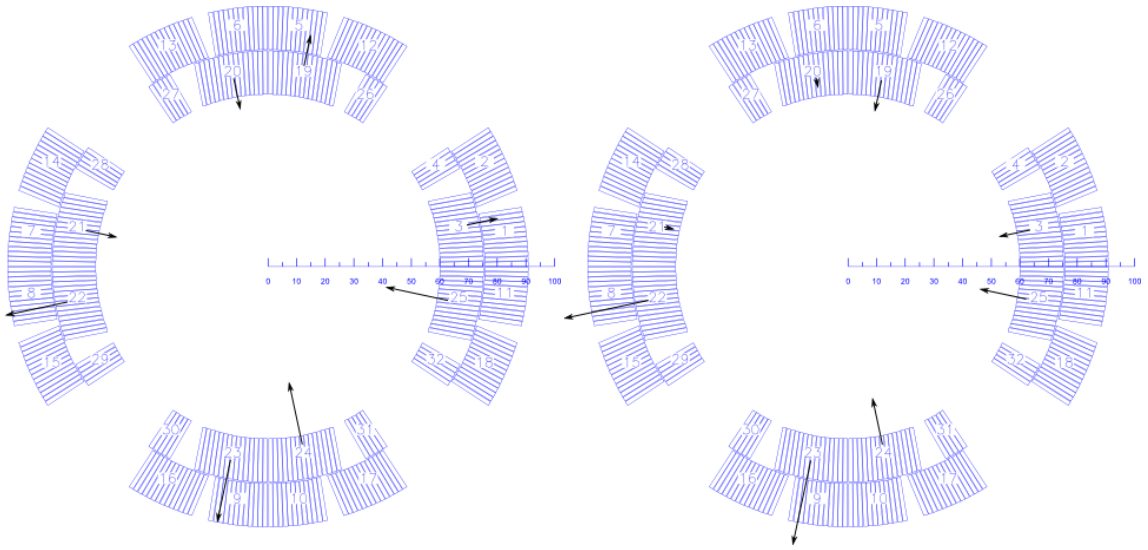

Figure 81 Qualitative radial displacement of block 3 and associated blocks for quadrupolar symmetry for the observed low-order harmonics at 13.4 kA for HQ01d (left) and 14 kA for HQ01e (right).

11 Issues and future improvements

1. Improve the signal/noise ratio for the measurements above 40 K. Probe with a larger diameter will be helpful with the limited field. The measurement with the phase lock technique should be investigated.
2. Rubbing issue.
3. Unexpected quenches and power supply stability. Symptoms of these unexpected quenches were summarized. A real quench after holding in step 3. Cu rods monitoring.
4. Helium evaporation during the current holding.
5. Measurement plan and coordination during the measurement.
6. Future measurements.
    a. Z-scan of both probes during warm measurements.

12 Summary

Magnetic measurements of HQ01e were performed at the magnet test facility at LBNL at 4.4 K during the HQ01e test in July 2011. The magnet was able to be ramped with 10 A/s from 50 A to 14.2 kA and back to 50 A, proceeded with a 10 kA precycle with the same ramp rate. The measurements and major observations were summarized. Large persistent current contribution and strong dynamic effect was observed. Control over the crossover resistance is necessary to reduce the dynamic effect.

13 Appendix – list of the measurements

Table 34 Z scan using the 100 mm PCB probe during the cooldown.

#	Date (MM/DD/YY)	Temp. (K)	Current (A)	Z range (mm)
Scan 1	06/27/11	295 K	± 15	0 – 1050
Scan 2	06/28/11	95 K	± 30	
Scan 3	06/28/11	50 K	± 30	

Table 35 Magnetic measurements performed at 4.4 K.

#	ID	Date (MM/DD/YY)	Probe	Test	Remarks
1	RR01	07/01/11	250 mm	Ramp-rate quench	300 A/s, Z = 40 mm
2	RR02				100 A/s
3	A01			Training quench	20 A/s, hybrid system
4	Scan 4			Z scan at 30 A	To align the 250 mm probe
5	Cycle 1	07/05/11		Magnetization	Feasibility test
6	Cycle 2				
7	Cycle 3				10 kA precycle, I. max = 14 kA
8	Cycle 4				Rubbing noise
9	RR03	07/07/11		Ramp-rate quench	100 A/s, Iq = 8013 A.
10	Cycle 5	07/07/11	100 mm	Magnetization	
11	A02			Training quench	Hybrid system
12	A03				Iq = 2252 A
13	A04				
14	Cycle 6			Magnetization	Rubbing noise
15	Step 1	07/08/11	250 mm	Stair-step	Tripped at 2 kA (PS issue)
16	Step 2				Tripped at 6 kA (mystery)
17	Step 3				Up ramp steps. Quenched at 14.3 kA after holding
18	Step 4				Down ramp attempt. Quenched at 13 kA.
19	A06	07/11/11		Training quench	
20	A07				50/7k, 20/12k, 10/14k, 5/Q
21	RR04			Ramp-rate quench	Fast down ramping
22	RR05				-200 A/s from 14 kA
23	RR06				Unexpected quench at 13 kA
24	RR07				
25	PHQ02			Protection heater test (50 A/s to 8 kA and hold for ~ 3 minutes)	
26	PHQ03				
27	PHQ04				
28	PHQ05				
29	PHQ06				
30	PHQ07				
31	PHQ08				
32	PHQ14				

33	Step 5	07/12/11		Stair-step	Down ramp. No cleansing quench followed.
34	Loop 1			Dynamic effect (x A/s round trip from 50 A to 10 kA. Hold at 10 kA for 1 minute)	20 A/s
35	Loop 2				40 A/s
36	Loop 3				60 A/s
37	RR08			Ramp-rate quench	50 A/s, hybrid system
38	RR09				75 A/s, hybrid system
39	RR10				200 A/s, hybrid system
40	RR11				225 A/s down ramp
41	PHQ15	07/13/11	100 mm	Protection heater test	Z = 290 mm
42	PHQ16				Hybrid system
43	PHQ18				Z = 228 mm
44	PHQ19				Z = 352 mm
45	PHQ20				
46	PHQ21				
47	PHQ22			Protection heater test, 10 kA	Z = 290 mm
48	PHQ23				Z = 228 mm
49	PHQ25				Z = 352 mm
50	PHQ26				Z = 290 mm
51	PHQ27			Protection heater test, 12 kA	Z = 290 mm
52	Step 6			Stair-step measurement (50 A/s for precycle up to 10 kA, 10 A/s between steps)	Tripped at 5 kA in the pre-cycle
53	Step 7				PS control program crashed at 8 kA. Provoked a quench.
54	Step 8				4 kA, 6 kA and 10 kA, up ramp.
55	A08			Training quench	z = -75 mm
56	A09	07/14/11			Hybrid system
57	A10				z = 352 mm, hybrid system

Table 36 Z scan using the 100 mm PCB probe during the warmup.

#	Date (MM/DD/YY)	Temp. (K)	Current (A)	Z range (mm)
Scan 5	07/15/11	~ 40 K	± 30	0 – 950
Scan 6	07/18/11	~ 90 K	± 30	
Scan 7	07/21/11	~ 130 K	± 20	
Scan 8	07/26/11	~ 180 K	± 20	
Scan 9	08/09/11	~ 285 K	± 15	

14 Appendix – average of the multipoles from different current polarities

To reduce the contribution of the residual magnetization, the multipoles from the measurements with two current polarities were averaged. Suppose *n* measurements were performed for the positive current (P) and negative current (N) at a certain location of the magnet bore, then the averaged angular flux at the location is given by $A = \frac{\sum_1^n (P_i - N_i)}{2n}$.

Each data file contains flux data points of *k* angular positions and can be considered a vector of *k* elements. The drift possibly due to the electronics is removed for each data file. The summation of different files follows the rule of the vector summation. Now for each location, there is only one averaged flux data file, which is analyzed following the same procedure as discussed in [Bottura01], i.e., feed-down correction, main field rotation and normalization.

For a quadrupole, the change of the current polarity corresponds to the rotation of the quadrupole for $\pi/2$ in the direction of either clockwise or anti-clockwise. Consider an anti-clockwise rotation for $\theta = \pi/2$, and denote the superscript of "-" for the harmonics measured for the negative current and "+" the harmonics for the positive current polarity, we have

$$C^- = C^+ \mathrm{e}^{in\theta}$$

and the following table.

n	2	3	4	5	6	7	8	9	10
$e^{in\theta}$, $\theta = \pi/2$	-1	i	1	-i	-1	i	1	-i	-1
$e^{in\theta}$, $\theta = -\pi/2$	-1	-i	1	i	-1	-i	1	i	-1

Thus, we have $B_2^- + iA_2^- = -B_2^+ - iA_2^+$, i.e., $B_2^- = -B_2^+$ and $A_2^- = -A_2^+$. Similarly, we have $B_3^- + iA_3^- = A_3^+ - iB_3^+$, i.e., $B_3^- = A_3^+$ and $A_3^- = -B_3^+$. Thus, for the normalized coefficient we have $b_3^- = -a_3^+$ and $a_3^- = b_3^+$ if there is no other contribution to bore field, e.g., residual magnetization or Earth field. One can repeat this for all the harmonics and obtain the following,

$$b_n^- = b_n^+ \text{ and } a_n^- = a_n^+ \text{ for } n = 2k \text{ and } k = 1,3,5,7, \ldots$$
$$b_n^- = -b_n^+ \text{ and } a_n^- = -a_n^+ \text{ for } n = 2k \text{ and } k = 2,4,6,8, \ldots$$
$$b_n^- = -a_n^+ \text{ and } a_n^- = b_n^+ \text{ for } \theta = \frac{\pi}{2}, n = 2k+1 \text{ and } k = 1,3,5,7, \ldots$$
$$b_n^- = a_n^+ \text{ and } a_n^- = -b_n^+ \text{ for } \theta = \frac{\pi}{2}, n = 2k+1 \text{ and } k = 2,4,6,8, \ldots$$
$$b_n^- = a_n^+ \text{ and } a_n^- = -b_n^+ \text{ for } \theta = -\frac{\pi}{2}, n = 2k+1 \text{ and } k = 1,3,5,7, \ldots$$
$$b_n^- = -a_n^+ \text{ and } a_n^- = b_n^+ \text{ for } \theta = -\frac{\pi}{2}, n = 2k+1 \text{ and } k = 2,4,6,8, \ldots$$

Figure 82 shows an example of a_3 in the frame of nominal powering polarity (positive current). The harmonics from the averaged flux data can be considered an average of the a_3 from the a_3 of the +15 A measurement and the $\underline{-b_3}$ of the -15 A measurement (for $z < 580$ mm, which can be contributed to the current leads effect). The difference between $-b_3^-$ ("n 15 A $-b_3$" in Figure 82) and a_3^+ ("p 15 A" in Figure 82) is from the residual magnetization from the iron parts in the magnet.

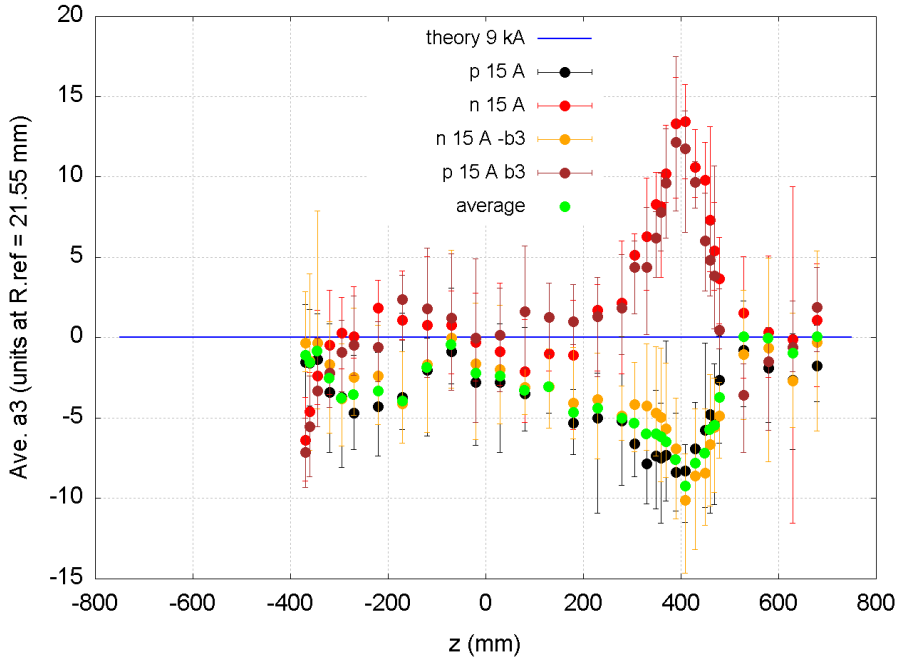

Figure 82 a_3 along the bore at 295 K, measured with +/- 15 A. The polarity of the harmonics was reversed to be consistent with the measurements performed at lower temperatures.

15 Appendix – harmonics of the magnetic straight section at different temperatures

Table 37 Multipoles in unit at three locations of the magnetic straight section. Averaged from +/- 30 A measurements at 50 K with the 100 mm probe. R.ref = 40 mm.

50 K	-215 mm	-115 mm	-15 mm	average	σ	σ/√N
b3	4.60	3.75	4.12	4.16	0.43	0.25
b4	-0.31	0.35	-0.09	-0.02	0.33	0.19
b5	0.25	-0.68	-1.22	-0.55	0.74	0.43
b6	3.14	3.15	4.55	3.61	0.81	0.47
b7	1.54	3.21	-1.66	1.03	2.47	1.43
b8	-4.56	1.35	-4.87	-2.69	3.50	2.02
b9	-1.82	-4.19	4.44	-0.52	4.46	2.57
b10	-3.28	-2.01	-1.73	-2.34	0.83	0.48
a3	-19.95	-17.33	-18.10	-18.46	1.35	0.78
a4	1.88	2.87	5.12	3.29	1.66	0.96
a5	-5.50	-5.51	-4.60	-5.20	0.53	0.30
a6	0.08	-0.20	-0.28	-0.13	0.19	0.11
a7	0.89	-4.02	3.57	0.15	3.85	2.22
a8	0.81	2.46	-4.09	-0.27	3.41	1.97
a9	-4.94	1.83	1.27	-0.61	3.76	2.17
a10	-1.06	-4.33	-0.39	-1.93	2.11	1.22

Table 38 Multipoles in unit at three locations of the magnetic straight section. Averaged from +/- 30 A measurements at 90 K with the 100 mm probe. R.ref = 40 mm.

95 K	-220 mm	-120 mm	-20 mm	average	σ	σ/√N
b3	4.29	3.86	2.14	3.43	1.14	0.66
b4	0.44	0.63	-0.22	0.28	0.44	0.26
b5	0.02	-0.61	0.46	-0.04	0.54	0.31
b6	2.05	3.90	2.21	2.72	1.02	0.59
b7	0.76	2.25	0.77	1.26	0.85	0.49
b8	-4.35	0.56	-4.24	-2.68	2.81	1.62
b9	8.24	3.04	3.76	5.01	2.82	1.63
b10	-7.71	-9.81	3.63	-4.63	7.23	4.17
a3	-10.19	-7.46	-7.27	-8.31	1.63	0.94
a4	0.68	1.13	2.69	1.50	1.06	0.61
a5	-1.92	-2.10	-2.80	-2.28	0.47	0.27
a6	-0.03	-1.13	-0.04	-0.40	0.63	0.36
a7	2.53	-1.78	2.86	1.20	2.59	1.49
a8	-1.95	3.27	-2.95	-0.54	3.34	1.93
a9	2.41	0.63	3.66	2.24	1.52	0.88

a10	3.34	-1.43	-10.64	-2.91	7.11	4.11

Table 39 Multipoles in unit at three locations of the magnetic straight section. Averaged from +/- 20 A measurements at 135 K with the 100 mm probe. R.ref = 40 mm.

135 K	-220 mm	-120 mm	-20 mm	average	σ	σ/√N
b3	0.41	3.66	-0.03	1.35	2.01	1.16
b4	0.87	-0.17	-0.26	0.15	0.63	0.36
b5	-0.49	0.60	1.05	0.39	0.79	0.46
b6	5.34	3.11	4.20	4.22	1.12	0.64
b7	2.34	0.64	-1.32	0.56	1.83	1.06
b8	1.71	-4.25	-4.03	-2.19	3.38	1.95
b9	5.15	9.12	1.28	5.18	3.92	2.26
b10	3.01	-6.21	18.25	5.02	12.35	7.13
a3	-10.20	-5.98	-6.23	-7.47	2.37	1.37
a4	0.37	0.38	1.86	0.87	0.85	0.49
a5	-2.95	-3.25	-2.22	-2.81	0.53	0.31
a6	1.18	-0.23	2.53	1.16	1.38	0.80
a7	1.13	-2.26	-0.05	-0.39	1.72	0.99
a8	-6.47	0.09	-1.74	-2.71	3.39	1.96
a9	10.02	-5.56	-11.58	-2.37	11.15	6.44
a10	6.96	14.16	-0.77	6.78	7.47	4.31

Table 40 Multipoles in unit at three locations of the magnetic straight section. Averaged from +/- 20 A measurements at 180 K with the 100 mm probe. R.ref = 40 mm.

180 K	-220 mm	-120 mm	-20 mm	average	σ	σ/√N
b3	2.66	5.40	-0.51	2.51	2.96	1.71
b4	0.25	1.36	-0.26	0.45	0.82	0.48
b5	0.71	0.31	-0.38	0.22	0.55	0.32
b6	0.80	3.18	5.50	3.16	2.35	1.35
b7	-1.93	3.90	0.15	0.71	2.96	1.71
b8	-0.93	1.60	-5.61	-1.65	3.66	2.11
b9	6.61	-7.21	11.97	3.79	9.89	5.71
b10	8.49	-6.63	11.55	4.47	9.73	5.62
a3	-9.62	-4.88	-3.87	-6.12	3.07	1.77
a4	0.34	1.10	1.54	0.99	0.61	0.35
a5	-1.31	-2.39	-1.60	-1.77	0.56	0.32
a6	0.45	3.15	2.08	1.89	1.36	0.79
a7	-1.77	1.44	2.98	0.88	2.43	1.40
a8	-5.79	2.26	-4.64	-2.72	4.35	2.51
a9	-11.30	5.75	-4.25	-3.27	8.57	4.95
a10	-3.71	-10.19	7.29	-2.20	8.84	5.10

Table 41 Multipoles in unit at three locations of the magnetic straight section. Averaged from +/- 15 A measurements at 285 K with the 100 mm probe. R.ref = 40 mm.

285 K	-220 mm	-120 mm	-20 mm	average	σ	σ/√N
b3	3.25	3.34	0.00	2.20	1.90	1.10
b4	1.02	0.61	-1.35	0.09	1.27	0.73
b5	-0.33	-0.11	-0.30	-0.25	0.12	0.07
b6	1.61	3.22	2.27	2.37	0.81	0.47
b7	-2.03	-4.34	0.90	-1.82	2.63	1.52
b8	-5.35	1.75	1.79	-0.60	4.11	2.37
b9	7.07	9.94	-1.54	5.16	5.97	3.45
b10	-0.64	-19.31	-3.43	-7.79	10.07	5.81
a3	-6.36	-4.63	-3.09	-4.69	1.63	0.94
a4	-0.83	1.37	1.96	0.83	1.47	0.85
a5	-0.84	-1.73	-1.18	-1.25	0.45	0.26
a6	1.62	4.43	-2.19	1.29	3.32	1.92
a7	-0.02	-3.59	-0.21	-1.27	2.01	1.16
a8	-1.87	-4.01	2.90	-1.00	3.54	2.05
a9	-0.42	0.07	-5.53	-1.96	3.10	1.79
a10	-10.26	-1.19	16.80	1.78	13.77	7.95

16 Appendix – harmonics sensitivity matrices

16.1 Current dependence of the geometric multipoles

The geometric multipoles as a function of current ranging from 20 A to 15 kA is calculated using Roxie 10.1 (Figure 83). Below 2 kA, b_6 is -1.63 units and was optimized to be about 0 at 120 T/m (10.5 kA) [Felice09]. The b_{10} was insensitive to the current and was within 0.02 units over the entire current range. With the option ODFAC disabled, a shift of about -0.4 units and -0.2 units were observed for b_6 and b_{10}, respectively over the entire current range. The calculation was consistent with that posted at the reference parameters folder at plone [3].

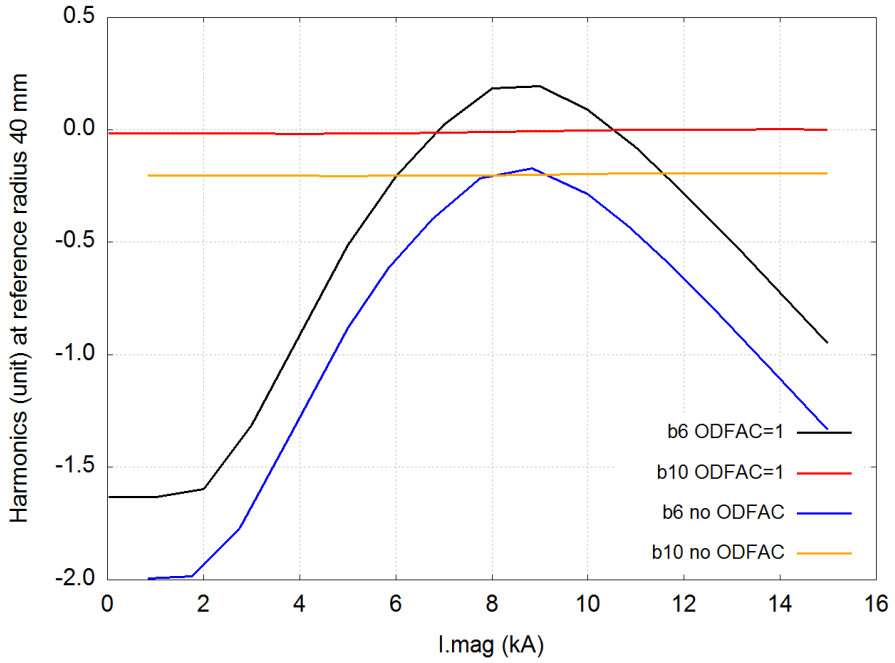

Figure 83 Roxie-calculated current dependence of geometric multipoles of HQ01 with and without ODFAC option activated in Roxie.

16.2 Cable alignment effect

The HQ cable has a nominal keystone angle of 0.75 degrees. Due to the small keystone angle, the cable may not be well constrained by the inner and outer radii of a coil layer. For example, the cables may slide away from the winding mandrel especially for those with increasing positioning angle, e.g., the cables in block 4 (Figure 9) [Gleis99] [Redaelli00]. The keystone angle effect on the field quality can be studied by adjusting the ODFAC parameter in ROXIE. The ODFAC was applied to all blocks of the coil simultaneously and thus only the allowed harmonics were affected. Table 42 presents the results with ODFAC ranging from 0 to 1, representing the cable aligned with from the inner to the out radius of the layer. The same results are plotted in Figure 84. A linear dependence of the ODFAC was observed. About 0.4 units of change was observed for b6 and 0.2 units for b10. The impact on the higher order harmonics, b_{14} and b_{18}, was negligible.

[3] https://plone.uslarp.org/MagnetRD/ModelMagnets/HQ/ReferenceParameters/120mmAperture/Roxie/

Table 42 Multipoles for the HQ with the conductor aligned with from the inner to the outer radius at 14 kA (R.ref = 40 mm).

ODFAC	0.0	0.2	0.4	0.6	0.8	1.0	Slope	RSQ
b6 (unit)	-1.11	-1.03	-0.95	-0.88	-0.80	-0.72	0.383	1
b10 (unit)	-0.19	-0.16	-0.12	-0.08	-0.04	0.00	0.196	1
b14 (unit)	-0.01	-0.01	-0.01	-0.01	-0.01	-0.01	0.00	1
b18 (unit)	-0.40	-0.40	-0.41	-0.41	-0.41	-0.41	-0.01	1

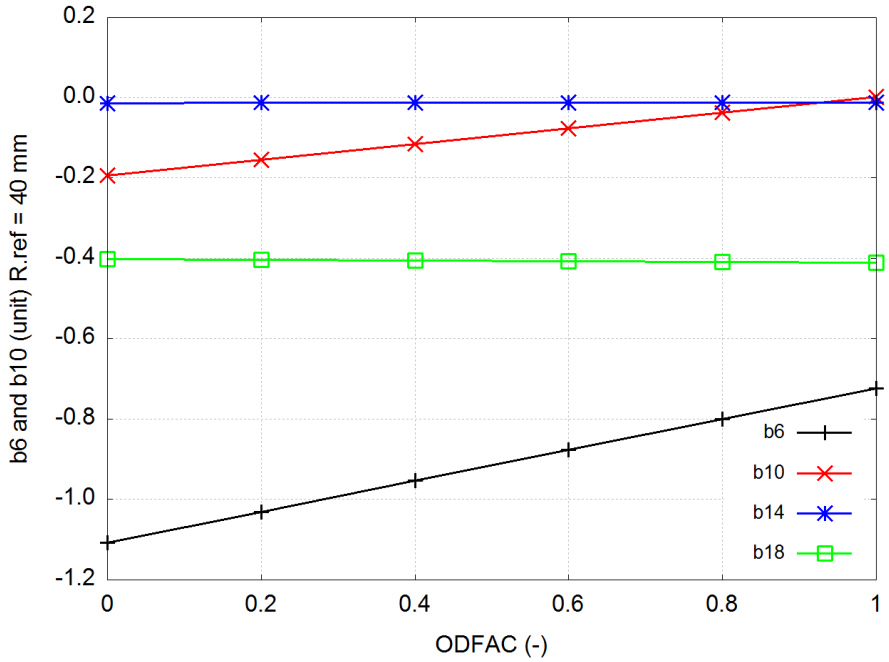

Figure 84 Allowed harmonics as a function of ODFAC variable in Roxie at 14 kA (R.ref = 40 mm).

16.3 Sensitivity on rigid block displacements for the allowed harmonics

According to the v8 ROXIE data file [Felice11], the nominal block positions in terms of winding radius, positioning and inclination angles are given in Table 43.

Table 43 Nominal block positions in the Roxie data file.

Block	Radius	Positioning angle (φ)	Inclination angle (α)	Cable
	[mm]	[degree]	[degree]	#
1	75.604	0.1061	0.0	12
2	75.604	15.7867	22.5778	14
3	60.000	0.1337	0.0	15
4	60.000	26.2084	30.0090	4

Sensitivity matrix was calculated to study the multipole sensitivity on geometrical displacements of the blocks [Redaelli00]. First, the effect of a rigid displacement of mandrel radius for each

block was calculated, i.e., $\delta r_i = 50\ \mu\text{m}$, where i = 1, 2, 3 and 4 (Figure 85)[4]. Second, the positioning angle change was considered, i.e., $\delta\varphi\_i = 50\mu\text{m}/(r\_i + r\_cond/2)$, where r_{cond} is the insulated conductor height (radial length, 15.35 mm). Thus, $\delta\varphi_1 = \delta\varphi_2 = 0.0344$ degree and $\delta\varphi_3 = \delta\varphi_4 = 0.0423$ degre , given the data in Table 43. Third, the inclination angle change was considered, i.e., $\_i = 50\mu\text{m}/(r\_cond/2)$, which gives $\delta\alpha = 0.373262$ degrees for all four blocks. Each block displacement was applied to all four poles (eight octants) and thus only the allowed harmonics are affected.

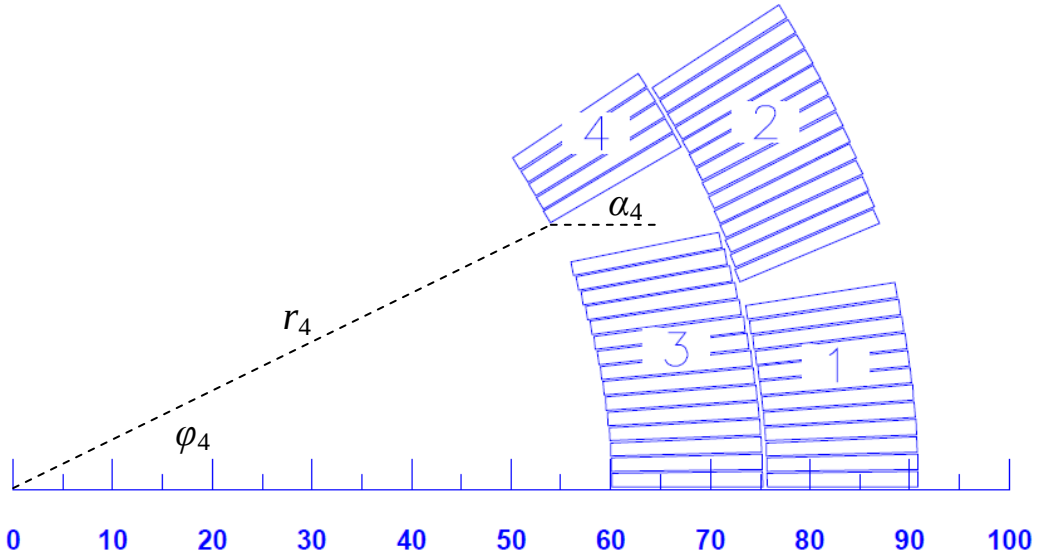

Figure 85 HQ01 coil block (x-axis dimension in mm). The winding radius, positioning and inclination angles for block 4 are shown.

The sensitivity matrix was calculated for current ranging from 20 A to 15 kA, with ODFAC option activated and inactivated. We only mention the current dependence of δb_6 because δb_6 has higher amplitude than higher order harmonics; the dependence of current was less than 8%. Below 2 kA, the change was constant as the iron was not saturated (Figure 86).

[4] In "Design variables" option of Roxie, we set the Xl = Xu = Xs = 75.604+0.05 = 75.654 mm and set String = Radius, Act = 3 for specified blocks only, and put 1 5-11 in the field for block number when moving block 1 and the corresponding blocks for quadrupole symmetry.

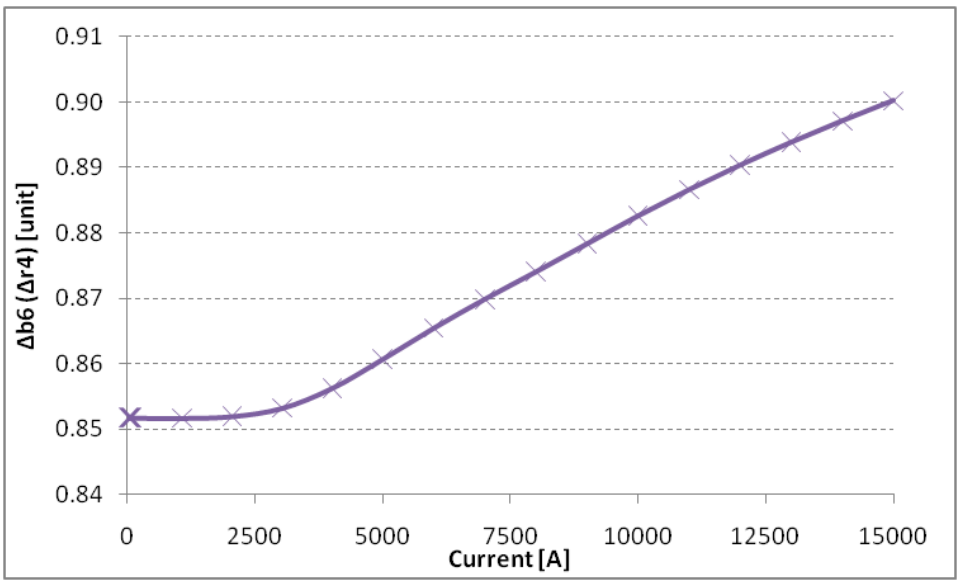

Figure 86 The change of b_6 due to 50 μm of r4 increase as a function of current with ODFAC option activated (reference radius 40 mm).

Table 44 and Table 45 list the sensitivity matrices at 20 A and 15 kA, respectively. The induced harmonics change decreases with the harmonics order: up to 1.8 units of change in b_6 and a few tenth of units change in b_{10} and negligible change in higher order harmonics. There is one exception: for the displacement of positioning and inclination angles for block 4, larger variation in b_{10} (up to 0.16 units) than in b_6 (up to 0.04 units) was observed. b_{10} was more sensitive to the change of azimuthal and tilt change of the position of block 4 than b_6. The significant change in b_6 results from φ3, α3 and r4. The angular change (φ or α) of block 3 affects more in b_6 than those of block 4. All harmonics are more sensitive to the movement of inner layers (block 3 and 4) than that of the outer layer (block 1 and 2).

Table 44 Sensitivity matrix for the allowed harmonics at 20 A (ODFAC=1, reference radius = 40 mm) .

	δr1	δr2	δr3	δr4
δ *b*6	-0.28	0.43	-0.51	0.85
δ *b*10	-0.01	0.01	0.13	-0.11
δ *b*14	0.00	0.00	0.01	-0.02
δ *b*18	0.00	0.00	0.00	0.01
	δφ1	δφ2	δφ3	δφ4
δ *b*6	-0.27	-0.26	-1.72	0.00
δ *b*10	-0.03	0.03	-0.27	0.15
δ *b*14	0.00	0.00	-0.01	-0.03
δ *b*18	0.00	0.00	0.00	0.00
	δα1	δα2	δα3	δα4
δ *b*6	-0.21	-0.23	-1.28	0.04
δ *b*10	-0.02	0.03	-0.23	0.11
δ *b*14	0.00	0.00	-0.02	-0.02
δ *b*18	0.00	0.00	0.00	0.00

Table 45 Sensitivity matrix for the allowed harmonics at 15 kA (ODFAC=1, reference radius = 40 mm).

	Δr1	Δr2	Δr3	Δr4
Δ*b*6	-0.30	0.45	-0.54	0.90
Δ*b*10	-0.01	0.01	0.14	-0.11
Δ*b*14	0.00	0.00	0.02	-0.02
Δ*b*18	0.00	0.00	0.00	0.01
	Δφ1	Δφ2	Δφ3	Δφ4
Δ*b*6	-0.28	-0.27	-1.81	0.00
Δ*b*10	-0.03	0.03	-0.28	0.16
Δ*b*14	0.00	0.00	-0.01	-0.03
Δ*b*18	0.00	0.00	0.00	0.00
	Δα1	Δα2	Δα3	Δα4
Δ*b*6	-0.22	-0.24	-1.35	0.04
Δ*b*10	-0.02	0.03	-0.24	0.11
Δ*b*14	0.00	0.00	-0.02	-0.02
Δ*b*18	0.00	0.00	0.00	0.00

The sensitivity matrix for allowed harmonics with ODFAC option deactivated are given in Table 46 and Table 47. They are practically identical to those calculated with ODFAC=1.

Table 46 Sensitivity matrix for the allowed harmonics at 20 A (ODFAC deactivated, reference radius = 40 mm) .

	δr1	δr2	δr3	δr4
δ *b*6	-0.28	0.43	-0.50	0.85
δ *b*10	-0.01	0.01	0.14	-0.11
δ *b*14	0.00	0.00	0.01	-0.02
δ *b*18	0.00	0.00	0.00	0.01
	δφ1	δφ2	δφ3	Δφ4
δ *b*6	-0.27	-0.26	-1.73	0.00
δ *b*10	-0.03	0.03	-0.27	0.15
δ *b*14	0.00	0.00	-0.01	-0.03
δ *b*18	0.00	0.00	0.00	0.00
	δα1	δα2	δα3	δα4
δ *b*6	-0.20	-0.23	-1.20	0.07
δ *b*10	-0.02	0.03	-0.19	0.10
δ *b*14	0.00	0.00	-0.01	-0.02
δ *b*18	0.00	0.00	0.00	0.00

Table 47 Sensitivity matrix for the allowed harmonics at 15 kA (ODFAC deactivated, reference radius = 40 mm).

	δr1	δr2	δr3	δr4
δ *b*6	-0.30	0.45	-0.53	0.90

δ *b*10	-0.01	0.01	0.14	-0.11
δ *b*14	0.00	0.00	0.02	-0.02
δ *b*18	0.00	0.00	0.00	0.01
	δφ1	δφ2	δφ3	Δφ4
δ *b*6	-0.28	-0.27	-1.82	0.00
δ *b*10	-0.03	0.03	-0.29	0.16
δ *b*14	0.00	0.00	-0.01	-0.03
δ *b*18	0.00	0.00	0.00	0.00
	δα1	δα2	δα3	δα4
δ *b*6	-0.21	-0.23	-1.26	0.08
δ *b*10	-0.02	0.03	-0.20	0.11
δ *b*14	0.00	0.00	-0.01	-0.02
δ *b*18	0.00	0.00	0.00	0.00

16.4 Sensitivity on rigid block displacements for the non-allowed harmonics

The example settings for block 1 and its quadrupolar symmetric blocks for different symmetry configurations in Roxie calculation was shown in Table 48. Positive radial movement correspond to outward movement; positive angle move towards the bisector of each Cartesian quadrant.

Table 48 Displacement direction for each block.

Configuration	direction	Block group	r [mm]	φ [degree]	α [degree]
2	+	1, 5-7	75.604+0.050	0.1061+0.0344	0+0.373262
	-	8-11	75.604-0.050	0.1061-0.0344	0-0.373262
3	+	1, 5, 10-11			
	-	6-9			
4	+	1, 5, 8-9			
	-	6-7, 10-11			
5	+	1, 7-8, 11			
	-	5-6, 9-10			
6	+	1, 7, 9-10			
	-	5-6, 8, 11			
7	+	1, 6, 9, 11			
	-	5, 7-8, 10			
8	+	1, 6, 8, 10			
	-	5, 7, 9, 11			

Eight configurations for the symmetry can be found in [Redaelli00]. Two important notes: 1) Orthogonal configurations, i.e., a change in one configuration does not affect the harmonics induced by another configuration; and 2) the linear dependence of the harmonics variation on the small geometry variation. These two features form the basis for the inverse analysis of the non-allowed harmonics.

Table 49 Sensitivity matrix for the non-allowed harmonics at 20 A (ODFAC=1, reference radius = 40 mm).

Sym		Δr1	Δr2	Δr3	Δr4	Δφ1	Δφ2	Δφ3	Δφ4	Δα1	Δα2	Δα3	Δα4
2	Δa3	1.34	1.31	**3.90**	0.91	-0.52	0.68	-0.76	0.87	-0.56	0.88	-1.16	0.90
	Δa5	-0.03	0.60	0.70	0.79	-0.48	-0.13	-1.94	0.19	-0.42	-0.09	-1.69	0.21
	Δa7	0.16	-0.13	0.68	-0.42	0.01	0.14	0.45	0.10	0.00	0.13	0.21	0.06
	Δa9	0.02	0.00	0.30	-0.15	-0.04	0.05	-0.21	0.13	-0.03	0.05	-0.22	0.09
3	Δb3	-1.34	-1.31	**-3.90**	-0.91	0.52	-0.68	0.76	-0.87	0.56	-0.88	1.16	-0.90
	Δb5	-0.03	0.60	0.70	0.79	-0.48	-0.13	-1.94	0.19	-0.42	-0.09	-1.69	0.21
	Δb7	-0.16	0.13	-0.68	0.42	-0.01	-0.14	-0.45	-0.10	0.00	-0.13	-0.21	-0.06
	Δb9	0.02	0.00	0.30	-0.15	-0.04	0.05	-0.21	0.13	-0.03	0.05	-0.22	0.09
4	Δa4	0.71	1.39	**3.38**	1.30	-1.03	0.15	**-2.82**	0.70	-0.98	0.29	-2.86	0.72
	Δa8	0.11	-0.05	0.79	-0.38	-0.07	0.13	-0.05	0.19	-0.06	0.12	-0.20	0.13
	Δa12	0.01	-0.01	0.05	0.01	0.00	0.00	0.06	-0.08	0.00	0.00	0.02	-0.05
	Δa16	0.00	0.00	0.00	0.01	0.00	0.00	0.00	0.01	0.00	0.00	0.00	0.01
5	Δb4	-0.97	0.39	-2.46	0.88	-0.57	-1.37	-2.68	-1.21	-0.47	-1.50	-1.93	-1.13
	Δb8	-0.06	0.13	0.10	0.18	-0.10	0.03	-0.78	0.32	-0.07	0.05	-0.60	0.27
	Δb12	0.00	0.00	0.06	-0.09	-0.01	0.01	-0.07	0.00	-0.01	0.01	-0.07	0.00
	Δb16	0.00	0.00	0.00	0.01	0.00	0.00	0.00	-0.01	0.00	0.00	0.00	-0.01
6	Δa3	-0.42	0.96	-0.16	1.05	-1.17	-1.30	**-3.47**	-0.87	-1.08	-1.40	-3.03	-0.83
	Δa5	0.53	0.05	1.98	-0.27	-0.09	0.53	0.31	0.72	-0.11	0.58	-0.05	0.65
	Δa7	0.03	0.13	0.60	0.08	-0.16	0.10	-0.75	0.37	-0.13	0.11	-0.69	0.32
	Δa9	0.04	-0.05	0.15	-0.13	0.01	0.01	0.27	-0.13	0.01	0.00	0.16	-0.11
7	Δb3	-0.42	0.96	-0.16	1.05	-1.17	-1.30	**-3.47**	-0.87	-1.08	-1.40	-3.03	-0.83
	Δb5	-0.53	-0.05	-1.98	0.27	0.09	-0.53	-0.31	-0.72	0.11	-0.58	0.05	-0.65
	Δb7	0.03	0.13	0.60	0.08	-0.16	0.10	-0.75	0.37	-0.13	0.11	-0.69	0.32
	Δb9	-0.04	0.05	-0.15	0.13	-0.01	-0.01	-0.27	0.13	-0.01	0.00	-0.16	0.11
8	Δa6	0.32	0.21	1.93	-0.06	-0.30	0.36	-0.80	0.76	-0.27	0.40	-0.96	0.67
	Δa10	0.03	-0.03	0.24	-0.16	-0.01	0.02	0.09	-0.09	-0.01	0.01	0.00	-0.07
	Δa14	0.00	0.00	0.00	0.03	0.00	0.00	0.02	-0.02	0.00	0.00	0.01	-0.01
	Δa18	0.00	0.00	0.00	0.00	0.00	0.00	0.00	0.01	0.00	0.00	0.00	0.00

16.5 Lorentz load at 15 kA

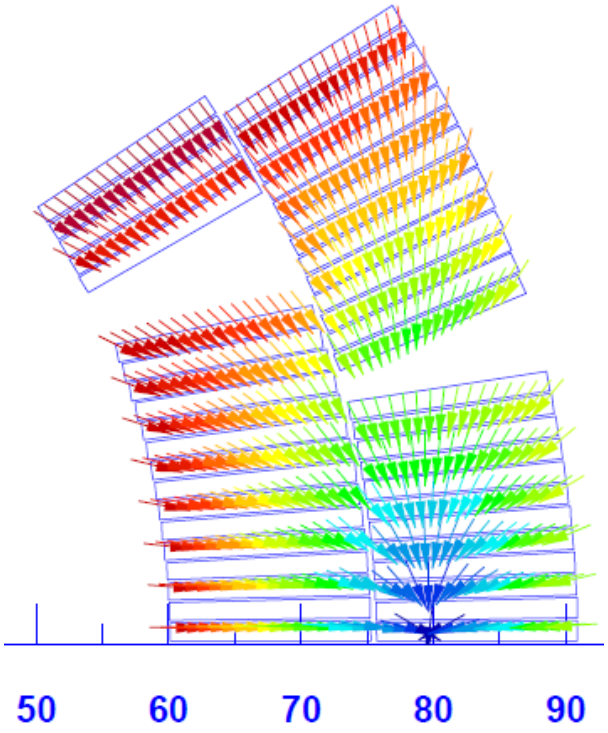

Figure 87 Lorentz force on the coil block at 15 kA (red → blue, 5000 N/m to 15 N/m).

17 Appendix – symmetry and coil pole strain

Here we try to quantify the asymmetry based on the measured azimuthal coil pole strain. A necessary condition for geometric symmetries may be related to the azimuthal pole strain as the following in HQ01e

$$\epsilon(\text{coil } 7) = \epsilon(\text{coil } 8) \text{ and } \epsilon(\text{coil } 5) = \epsilon(\text{coil } 9) \text{ for the top-bottom symmetry;}$$
$$\epsilon(\text{coil } 7) = \epsilon(\text{coil } 5) \text{ and } \epsilon(\text{coil } 8) = \epsilon(\text{coil } 9) \text{ for the left-right symmetry.}$$

One may use the ratio between the coil pole azimuthal strain to describe the coil asymmetry. The difference between the measured ratio and a unit ratio of 1 characterize the asymmetry, where the unit ratio of 1 means equal strain of two coils. The larger the difference, the more asymmetry may exist between the two coils. Table 50 shows the ratios of pole strain for each symmetry case at the end of loading of HQ01e.

Table 50 The measured azimuthal pole strain ratio for two symmetry cases.

Symmetry	Coil pair	Pole strain ratio	Distance to symmetry
Top-bottom	7 : 8	1.15 or 0.87	0.19
	5 : 9	1.14 or 0.88	
Left-right	7 : 5	0.92 or 1.09	0.12
	8 : 9	0.91 or 1.10	

For a $\cos 2\theta$ quadrupole, each symmetry case involves two coil pairs. In this case, we characterize the asymmetry on a 2D Cartesian plane by calculating the "distance" between the measured point and the symmetry point. Four measured points are available for one symmetry case because both the strain ratio and its reciprocal can be used. The geometric mean of four distances is defined as the "distance to symmetry" or the degree of asymmetry. Figure 88 shows an example of the top-bottom symmetry case. The x-axis is the pole azimuthal strain ratio between coil 7 and 8; the y-axis is the ratio between coil 5 and 9. The two measured ratios yield four red points; the symmetry case corresponds to the black point.

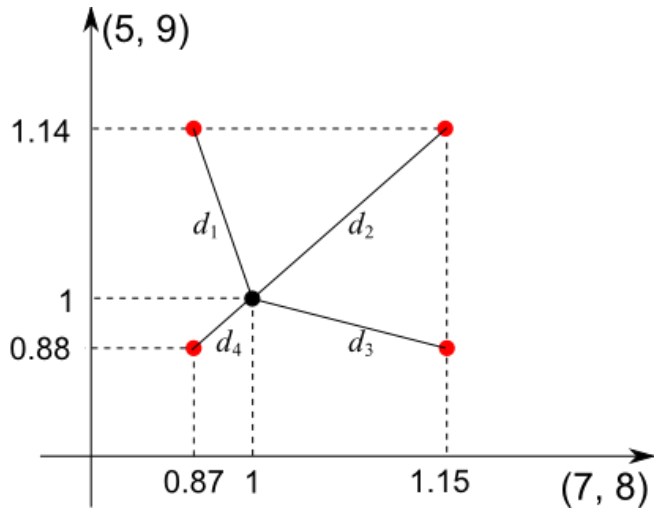

Figure 88 The top-bottom asymmetry of HQ01e based on the distance between the measured pole strain ratios (red points) and the symmetric case (black point).

A distance of 0 indicates symmetry. Table 50 gives the distance for two symmetries of HQ01e at the end of room-temperature loading. We see both asymmetries, with the top-bottom asymmetry

more pronounced than the left-right asymmetry. This was consistent with the observed $a_3 > b_3$. We note that the consistency can be a coincident as during the warmup the consistency did not occur. It will be interesting to compare the measured harmonics to the measured pole azimuthal strain if there is any correlation between these two objects.

18 Appendix – sensitivity matrix of the dynamic multipole on the cross-over conductance

We determine the sensitivity matrix on the following scales. First, block groups that satisfying the quadrupole symmetry. In this case, the cross-over conductance is uniform and constant in each coil block that belongs to the same group. Second, the cross-over conductance is uniform for each individual block but may vary between blocks. Third, the cross-over conductance is uniform for each individual cable but may vary between cables. Nominal coil block geometry is used.

The strand parameters relevant to the inter-strand coupling current simulation are given in Table 51.

Table 51 Strand transient parameters used in ROXIE.

R_c (Ω)	R_a (Ω)	Filament twist pitch (m)
0.001	0.001	0.014

We note that with the R_c and R_a values in Table 51 lead to negligible inter-strand coupling current with the ramp rates used in the measurement. To determine the contribution due to a specific coil block or cable, its R_c value was set to a specific value using the Design Variable option in ROXIE. Figure 90 shows a numerical example given by ROXIE during a ramp to 10 kA at 40 A/s for block 3 and the associated coil blocks for quadrupole symmetry. Various R_c values ranging from 0.5 $\mu\Omega$ to 10 $\mu\Omega$ were calculated. The multipole amplitude increases with the decreasing R_c.

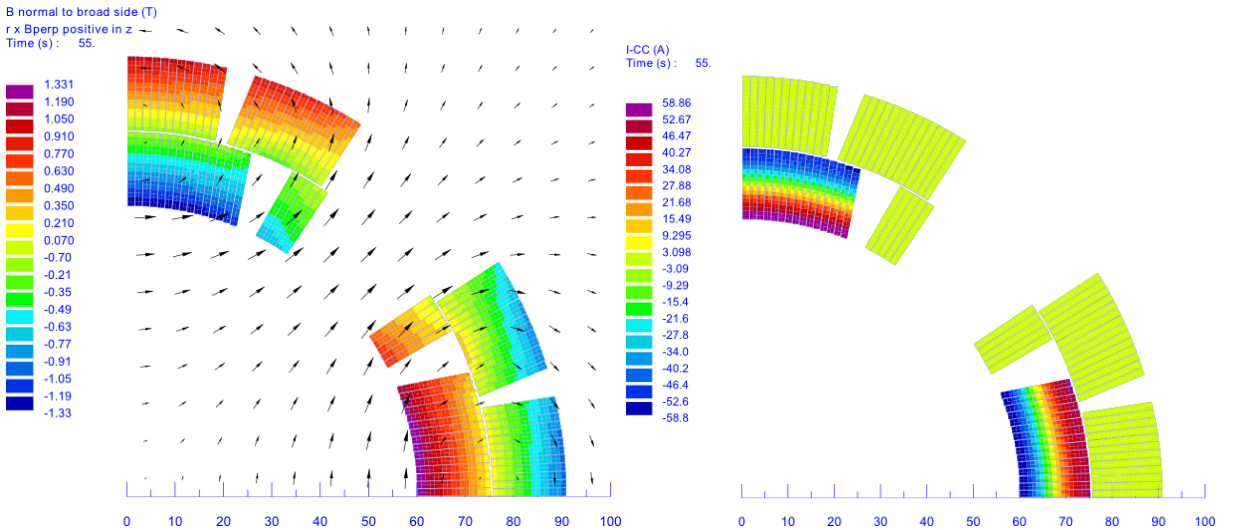

Figure 89 Inter-strand coupling current with R_c = 0.5 $\mu\Omega$ in block 3 and the associated blocks for quadrupole symmetry (one quadrant shown). Left: flux density perpendicular to the cable wide surface. Right: Amplitude of the induced inter-strand coupling currents. Note that the blocks with the default R_c = 1 mΩ have only negligible induced current (blocks with the light green color).

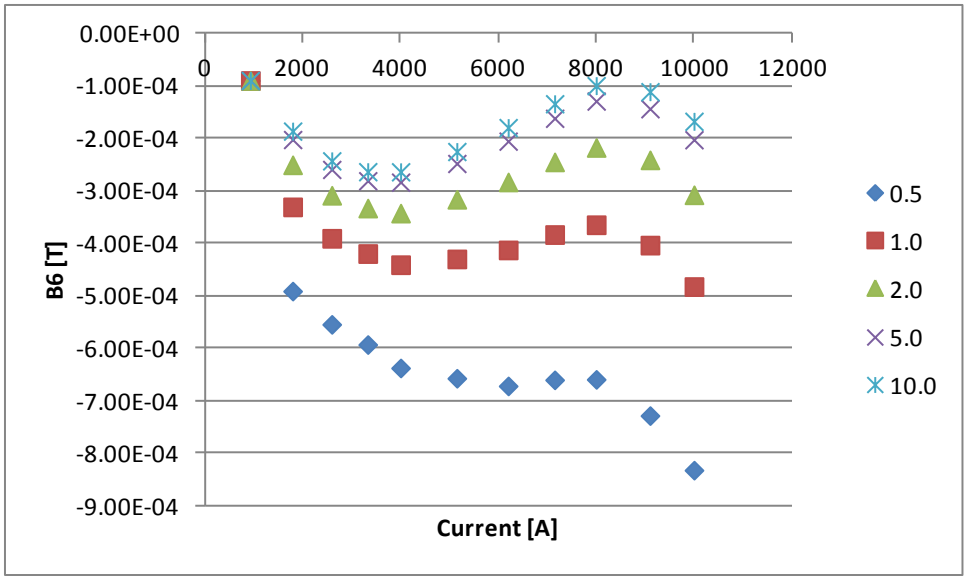

Figure 90 Calculated B_6 in T during the up ramp to 10 kA at 40 A/s. R_c ranges from 0.5 $\mu\Omega$ to 10 $\mu\Omega$. R.ref = 40 mm.

The linear dependence of B_6 on G_c can be seen at each current levels and Figure 91 gives an example of the contribution of each of the four blocks at 10 kA, 40 A/s. The slope is defined as the sensitivity of multipole to the change of cable cross-over conductance G_c. In general, the multipoles are most sensitive to the G_c of coil block 3 and the associated blocks leading to the quadrupole symmetry. The next important block is 4. The multipoles are less sensitive to the conductance in coil blocks 1 and 2. This block-dependent behavior can be explained by the higher flux density perpendicular to the cable wide surface in the inner layer and thus higher inter-strand coupling current was induced. This block-dependent sensitivity was similar to the sensitivity of the geometric errors on each coil block. Due to the linear dependence, only three R_c values (0.5 $\mu\Omega$, 1.0 $\mu\Omega$ and 10 $\mu\Omega$) were used to determine the slope.

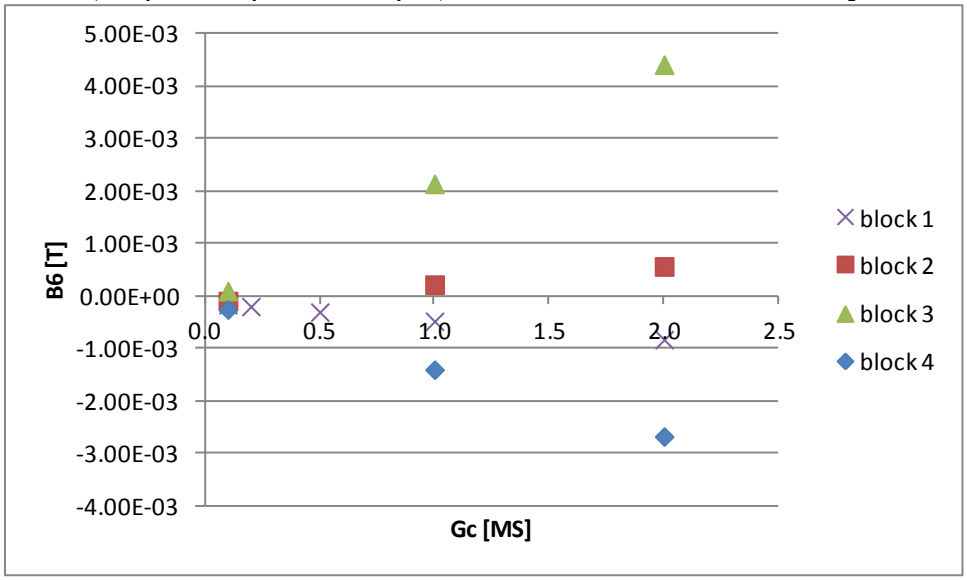

Figure 91 Calculated B_6 in T as a function of cross-over conductance at 10 kA, 40 A/s. R.ref = 40 mm.

18.1 Block groups for quadrupole symmetry

In this case, R_c is uniform in each of the four block groups satisfying the quadrupole symmetry. As a result, only allowed multipoles will be affected by the inter-strand coupling currents and no non-allowed multipole appears in the calculation with the nominal coil geometry.

In addition to the linear relationship between the multipole and cross-over conductance, a non-zero intercept was also observed with B_{all} selected as the field source for the multipole calculation in ROXIE. By definition, the intercept multipoles correspond to an infinite R_c (G_c = 0). As a result, the calculated intercepts for the quadrupole symmetry case are the geometric error at different current levels (Figure 83). Subtracting the intercept from the calculated multipoles, one obtains the multipole contribution from the inter-strand coupling currents, identical to the results when specifying B_{iscc} as the field source in ROXIE. This is why only the slope matters here. Table 52 gives the sensitivity matrix for the quadrupole symmetry case at 10 kA, 40 A/s with R.ref = 40 mm. The unit for the slopes is mT/MS. One sees that 1) the contribution to the multipole decreases as the multipole order increases. 2) The first three allowed multipoles are more sensitive to the inter-strand coupling current in block 3 than to the other three blocks. 3) The inter-strand current in block 1 always reduces the allowed multipoles.

Table 52 Sensitivity matrix (in mT/MS) for the block groups with quadrupole symmetry. 10 kA, 40 A/s. R.ref = 40 mm.

Block group	1	2	3	4
B_2	-3.06	-2.37	17.53	1.79
B_6	-0.35	0.35	2.27	-1.28
B_{10}	-0.01	0.02	-0.29	0.12

18.2 Individual block

Here we consider the contribution to the dynamic multipole from each block with uniform R_c. HQ magnet has 32 coil blocks. As before, a sensitivity matrix can be calculated using ROXIE. Table 53 lists the sensitivity for the selected normal multipoles. Table 54 lists the sensitivity for the skew multipoles. Again, multipoles are more sensitive to the contribution from block 3 and the associated blocks. The sensitivities for the blocks satisfying the quadrupole symmetry, e.g., blocks 3 and 19 – 25, have similar but not identical amplitude.

Table 53 Sensitivity matrix (in mT/MS) for each of the 32 coil blocks. Normal multipoles. 10 kA, 40 A/s. R.ref = 40 mm.

		B2	B3	B4	B5	B6	B10
	block1	-4.21E-01	-3.12E-01	-1.87E-01	-1.03E-01	-5.29E-02	-2.08E-03
	block2	-3.17E-01	-1.26E-01	-1.05E-03	4.51E-02	4.67E-02	3.15E-03
	block3	2.05E+00	1.60E+00	1.04E+00	5.74E-01	2.66E-01	-3.50E-02
	block4	2.10E-01	1.58E-02	-1.32E-01	-1.80E-01	-1.54E-01	1.46E-02
Block 1 group	block5	-4.21E-01	-1.25E-01	1.87E-01	7.25E-02	-5.29E-02	-2.08E-03
	block6	-4.74E-01	1.32E-01	1.93E-01	-7.58E-02	-5.44E-02	-2.07E-03
	block7	-5.26E-01	3.66E-01	-2.19E-01	1.20E-01	-6.20E-02	-2.40E-03
	block8	-5.26E-01	3.66E-01	-2.19E-01	1.20E-01	-6.20E-02	-2.40E-03
	block9	-5.26E-01	1.48E-01	2.19E-01	-8.58E-02	-6.20E-02	-2.40E-03

	block10	-5.26E-01	-1.48E-01	2.19E-01	8.57E-02	-6.20E-02	-2.40E-03
	block11	-4.74E-01	-3.22E-01	-1.93E-01	-1.06E-01	-5.44E-02	-2.07E-03
Block 2 group	block12	-3.17E-01	-2.87E-01	1.05E-03	1.06E-01	4.67E-02	3.15E-03
	block13	-3.15E-01	2.98E-01	1.54E-03	-1.11E-01	4.84E-02	3.30E-03
	block14	-3.69E-01	1.43E-01	-1.39E-03	-5.09E-02	5.27E-02	3.58E-03
	block15	-3.15E-01	1.41E-01	-1.64E-03	-5.00E-02	5.19E-02	3.54E-03
	block16	-3.15E-01	3.19E-01	1.64E-03	-1.19E-01	5.19E-02	3.54E-03
	block17	-3.69E-01	-3.25E-01	1.39E-03	1.20E-01	5.27E-02	3.58E-03
	block18	-3.15E-01	-1.32E-01	-1.54E-03	4.66E-02	4.84E-02	3.30E-03
Block 3 group	block19	2.05E+00	1.18E+00	-1.04E+00	-9.07E-01	2.66E-01	-3.50E-02
	block20	2.05E+00	-1.17E+00	-1.03E+00	8.97E-01	2.66E-01	-3.41E-02
	block21	1.89E+00	-1.50E+00	9.68E-01	-5.37E-01	2.48E-01	-3.29E-02
	block22	1.89E+00	-1.50E+00	9.68E-01	-5.37E-01	2.48E-01	-3.29E-02
	block23	1.89E+00	-1.11E+00	-9.68E-01	8.49E-01	2.48E-01	-3.29E-02
	block24	1.89E+00	1.11E+00	-9.68E-01	-8.49E-01	2.48E-01	-3.29E-02
	block25	2.05E+00	1.59E+00	1.03E+00	5.71E-01	2.66E-01	-3.41E-02
Block 4 group	block26	2.10E-01	3.62E-01	1.32E-01	-1.16E-01	-1.54E-01	1.46E-02
	block27	2.10E-01	-3.62E-01	1.33E-01	1.16E-01	-1.54E-01	1.47E-02
	block28	2.10E-01	-1.42E-02	-1.22E-01	1.67E-01	-1.42E-01	1.35E-02
	block29	2.10E-01	-1.42E-02	-1.25E-01	1.71E-01	-1.45E-01	1.38E-02
	block30	2.10E-01	-3.42E-01	1.25E-01	1.10E-01	-1.45E-01	1.38E-02
	block31	2.10E-01	3.35E-01	1.22E-01	-1.08E-01	-1.42E-01	1.35E-02
	block32	2.10E-01	1.58E-02	-1.33E-01	-1.81E-01	-1.54E-01	1.47E-02

Table 54 Sensitivity matrix (in mT/MS) for each of the 32 coil blocks. Skew multipoles. 10 kA, 40 A/s. R.ref = 40 mm.

		A3	A4	A5	A6	A10
	block1	1.26E-01	1.02E-01	7.25E-02	4.74E-02	5.21E-03
	block2	2.87E-01	1.97E-01	1.06E-01	4.46E-02	-3.58E-03
	block3	-1.18E+00	-1.11E+00	-9.07E-01	-6.68E-01	-9.29E-02
	block4	-3.62E-01	-2.55E-01	-1.16E-01	-7.83E-03	2.95E-02
Block 1 group	block5	3.12E-01	1.02E-01	-1.03E-01	-4.74E-02	-5.21E-03
	block6	3.22E-01	-1.06E-01	-1.06E-01	4.95E-02	5.43E-03
	block7	1.49E-01	-1.21E-01	8.57E-02	-5.61E-02	-6.16E-03
	block8	-1.49E-01	1.20E-01	-8.57E-02	5.61E-02	6.16E-03
	block9	-3.66E-01	1.20E-01	1.20E-01	-5.61E-02	-6.16E-03
	block10	-3.66E-01	-1.21E-01	1.20E-01	5.61E-02	6.16E-03
	block11	-1.31E-01	-1.06E-01	-7.57E-02	-4.95E-02	-5.43E-03
Block 2 group	block12	1.26E-01	1.97E-01	4.51E-02	-4.46E-02	3.58E-03
	block13	1.32E-01	-2.05E-01	4.66E-02	4.65E-02	-3.71E-03
	block14	3.24E-01	-2.23E-01	1.20E-01	-5.05E-02	4.05E-03
	block15	-3.20E-01	2.20E-01	-1.19E-01	4.99E-02	-3.98E-03

	block16	-1.41E-01	2.20E-01	-5.00E-02	-4.99E-02	3.98E-03
	block17	-1.43E-01	-2.23E-01	-5.09E-02	5.05E-02	-4.05E-03
	block18	-2.98E-01	-2.05E-01	-1.11E-01	-4.65E-02	3.71E-03
Block 3 group	block19	-1.60E+00	-1.11E+00	5.74E-01	6.68E-01	9.29E-02
	block20	-1.59E+00	1.10E+00	5.71E-01	-6.61E-01	-9.22E-02
	block21	-1.11E+00	1.04E+00	-8.49E-01	6.25E-01	8.68E-02
	block22	1.11E+00	-1.04E+00	8.49E-01	-6.26E-01	-8.68E-02
	block23	1.50E+00	-1.04E+00	-5.37E-01	6.26E-01	8.68E-02
	block24	1.50E+00	1.04E+00	-5.37E-01	-6.25E-01	-8.68E-02
	block25	1.17E+00	1.10E+00	8.97E-01	6.61E-01	9.22E-02
Block 4 group	block26	-1.58E-02	-2.55E-01	-1.80E-01	7.83E-03	-2.95E-02
	block27	-1.53E-02	2.56E-01	-1.81E-01	-7.74E-03	2.95E-02
	block28	-3.34E-01	2.36E-01	-1.08E-01	7.35E-03	-2.73E-02
	block29	3.42E-01	-2.42E-01	1.10E-01	-7.42E-03	2.79E-02
	block30	1.47E-02	-2.42E-01	1.71E-01	7.42E-03	-2.79E-02
	block31	1.42E-02	2.36E-01	1.67E-01	-7.35E-03	2.73E-02
	block32	3.62E-01	2.56E-01	1.16E-01	7.74E-03	-2.95E-02

To compare with the sensitivity obtained from the quadrupole symmetry (Table 52), Table 55 lists the same multipole sensitivity by summing the contribution from each individual block (within one block group). When the sensitivity amplitude is small, the relative error can be large, e.g., the sensitivity of B_{10} to block groups 1 and 2. For larger sensitivity amplitude, the relative error is within 10%, e.g., the sensitivity of multipoles to block groups 3 and 4. Thus, the difference between two cases can be partially due to numerical calculation. However, 27% of relative error was observed in the sensitivity of B_2 to coil block 1, which may not be explained by the numerical error.

Table 55 Sensitivity of the allowed multipole (in mT/MS) based on the calculation of each individual block. 10 kA, 40 A/s. R.ref = 40 mm.

Block group	1	2	3	4
B_2	-3.89	-2.63	15.79	1.68
B_6	-0.46	0.4	2.06	-1.19
B_{10}	-0.02	0.03	-0.27	0.11

Table 56 lists the sensitivity of allowed and non-allowed multipoles to each coil block group assuming the uniform G_c in each coil block. This will be compared to the sensitivity matrix determined on the level of individual cable.

Table 56 Sensitivity (mT/MS) of allowed and non-allowed multipoles to each block group.

Block group	1	2	3	4
B_2	-3.89E+00	-2.63E+00	1.58E+01	1.68E+00
B_3	1.05E-01	3.26E-02	2.08E-01	-4.70E-03

B_4	-4.00E-06	-9.20E-07	5.00E-06	-2.00E-06
B_5	2.92E-02	-1.19E-02	6.28E-02	-2.13E-02
B_6	-4.63E-01	3.99E-01	2.06E+00	-1.19E+00
B_{10}	-1.79E-02	2.71E-02	-2.70E-01	1.13E-01
A_3	-1.04E-01	-3.37E-02	-2.06E-01	6.33E-03
A_4	-9.98E-03	-2.08E-02	-2.56E-02	-9.48E-03
A_5	2.93E-02	-1.20E-02	6.28E-02	-2.13E-02
A_6	-1.00E-06	2.90E-06	7.00E-06	-4.20E-07
A_{10}	3.30E-07	1.00E-08	-3.50E-06	1.00E-06

18.3 Individual cable in block 3 and 4

To calculate the sensitivity of multipole on the individual cable level, we input the information of each cable in the block 2D widget. For the case of individual cable in block 3 and 4, we have 44 blocks (40 cables + 4 blocks) per coil and 176 blocks (160 cables in the inner layer and 16 outer layer blocks) of the whole quadrupole magnet. The calculation was performed the same way as the previous two cases. The only difference was ROXIE was used in batch mode with a shell script for efficiency. The whole sensitivity matrix is too large to be included here. Instead, we compare the multipole sensitivity to each block group between the case here and the previous case of uniform G_c in each coil block.

Table 57 Sensitivity (mT/MS) of multipoles to each block group (individual cable in block 3 and 4).

Block group	1	2	3	4
B_2	-3.89E+00	-2.63E+00	1.56E+01	1.28E+00
B_3	1.05E-01	3.26E-02	2.04E-01	-5.68E-03
B_4	-4.00E-06	-9.60E-07	1.72E-06	-1.70E-06
B_5	2.92E-02	-1.19E-02	6.29E-02	-2.12E-02
B_6	-4.63E-01	4.00E-01	2.06E+00	-1.19E+00
B_{10}	-1.79E-02	2.71E-02	-2.70E-01	1.13E-01
A_3	-1.04E-01	-3.37E-02	-2.10E-01	6.35E-03
A_4	-9.98E-03	-2.08E-02	-2.32E-02	-7.45E-03
A_5	2.93E-02	-1.20E-02	6.28E-02	-2.13E-02
A_6	-5.00E-07	2.90E-06	5.10E-06	-1.46E-07
A_{10}	3.30E-07	1.00E-08	-1.90E-07	-4.70E-07

The sensitivities of the multipoles to block group 1 and 2 shown in Table 57 agree well with those calculated with the uniform block Gc except a 50% relative error in the sensitivity of A6 which has a small amplitude and the difference does not lead to significant difference in Gc estimation. For block groups 3 and 4, large relative error was observed in the multipoles whose sensitivity has small amplitude, e.g., B4, A6 and A10. For multipoles with relevant amplitude, the relative error with respect to Table 56 was less than 1% expect for the sensitivity B2 and B3 to block group 4, which reached 20%.

18.4 Comparison of the sensitivity matrices with and without iron considered

On p. 77 of the ROXIE 9.3 manual, it was mentioned that the network model for inter-strand coupling current calculation cannot work with the non-linear iron. The previous cases were all calculated with iron yoke. Thus, the sensitivity matrix without iron was calculated for comparison. With iron considered, the sensitivity of block group 1 and 2 was about 85% to 90% of the sensitivity without considering iron. For block group 3 and 4, the sensitivity of the iron case was about 105% of the no-iron case. Since sensitivities of block 3 and 4 have higher amplitude than those of block 1 and 2, the sensitivity matrix of the no-iron case leads to lower R_c distribution than those of the case considering the iron.

19 Acknowledgment

The authors thank the technical staff of three labs for their expertise of the magnet fabrication and quality control. The cabling effort and documentation of H. Higley and N. Liggins are greatly appreciated. The indispensible support from P. Bish, S. King, C. Kozy, and J. Swanson during the magnetic measurements are greatly appreciated. We also thank B. Richter of GMW Associates and P. Keller of Metrolab for the loan of two fast digital integrators and their help during the system setup. The discussion of the test results with A. Jain of BNL is also greatly appreciated. This work was supported by the Director, Office of Science, High Energy Physics, U.S. Department of Energy under contract No. DE-AC02-05CH11231.

20 References

[Auchmann11] Expected field quality in the 11-T dipole. private communication, 11/2011.

[Bellesia04] Spread in Dipole Cable magnetization and Consequences on the Spread of DC Persistent Currents in the Main Dipole of the Large Hadron Collider. CERN Project Note 365.

[Bottura01] Standard analysis procedures for field quality measurement of the LHC magnets — part I: harmonics. Technical Report LHC-MTA-IN-97-007, LHC/MTA, 2001.

[Caspi10] Design of a 120 mm Bore 15 T Quadrupole for the LHC Upgrade Phase II. http://dx.doi.org/10.1109/TASC.2010.2040147

[Corato11] Measurement of the Transverse Resistivity of NbTi and Internal-Tin Nb_3Sn Strands. http://dx.doi.org/10.1109/TASC.2010.2093097

[denOuden97] Application of Nb_3Sn Superconductors in High-Field Accelerator Magnets. http://dx.doi.org/10.1109/77.614608

[DiMarco07] Rotating circuit board probes for magnetic measurements. The 15th Internal Magnetic Measurement Workshop, Fermilab, August 2007. http://tdserver1.fnal.gov/immw15/

[HQ01d] Summary of the HQ01d magnetic measurement. Superconducting Magnet Program report, in preparation.

[HQ01e_mm_plan] HQ01e magnetic measurement plan.

[Hybrid_system] A hybrid data acquisition system for magnetic measurement of accelerator magnets. Superconducting Magnet Program report. LBNL-4857E.

[Joseph08] Magnetic measurement DAQ system specification. Document # 40Y570, Superconducting Magnet Program, LBNL, December 2008.

[Felice09] Design of HQ—A High Field Large Bore Nb_3Sn Quadrupole Magnet for LARP. http://dx.doi.org/10.1109/TASC.2009.2019105

[Ferracin11] HQ01e mechanical performance. LARP-CERN video-meeting. August 10, 2011. https://plone.uslarp.org/MagnetRD/ModelMagnets/HQ/Meetings/2011/2011-08-10/Presentations/2-MechanicalPerformance.pdf

[Ferracin11a] HQ01d strain gauge data analysis. LARP Collaboration Meeting 16. May 17, 2011. https://indico.fnal.gov/getFile.py/access?contribId=58&sessionId=7&resId=0&materialId=slides&confId=4041

[Ferracin11b] Mechanical behavior of HQ01, a Nb_3Sn accelerator-quality quadrupole magnet for the LHC luminosity upgrade. MT-22.

[Fischer01] Beam-based measurements of persistent current decay in the Relativistic Heavy Ion Collider. http://link.aps.org/doi/10.1103/PhysRevSTAB.4.041002

[Gleis99] Field quality in the LHC main quadrupole prototype before the cold tests. CERN Project Note 209.

[Kashikhin99] Correction of Coil Magnetization Effect in Nb_3Sn High Field Dipole Magnet Using Thin Iron Strips. FNAL report TD-99-048.

[Martchevsky11] HQ01e quench performance. https://plone.uslarp.org/MagnetRD/ModelMagnets/HQ/Meetings/2011/2011-08-10/Presentations/3-HQ01e-quench-performance.pdf

[Ogitsu97] Influence of inter-strand coupling current on field quality of superconducting accelerator magnets.

[Redaelli00] Analysis of the magnetic field perturbations in dipoles and quadrupoles of the Large Hadron Collider (LHC). PhD thesis.

[Richter97] DC Measurement of Electrical Contacts between Strands in Superconducting Cables for the LHC Main Magnets. http://dx.doi.org/10.1109/77.614621

[Sabbi11] Progress in high field accelerator magnet development by the US LHC Accelerator Research Program. http://arxiv.org/abs/arXiv:1108.1625

[Sammut06] Mathematical formulation to predict the harmonics of the superconducting Large Hadron Collider magnets. http://link.aps.org/doi/10.1103/PhysRevSTAB.9.012402

[Velev11] Field Quality of the First LARP Nb3Sn 3.7 m-Long Quadrupole Model of LQ Series. http://dx.doi.org/10.1109/TASC.2010.2100797

[Verweij94] Field errors due to inter-strand coupling currents in the LHC dipole and quadrupole. http://cern-verweij.web.cern.ch/CERN-Verweij/Papers/CEINT7_v3.pdf

[Verweij95] Electrodynamics of Superconducting Cables in Accelerator Magnets. PhD thesis.

[Wolf97] Determination of Interstrand Contact Resistance from Loss and Field Measurements in LHC Dipole Prototypes and Correlation with Measurements on Cable Samples. http://dx.doi.org/10.1109/77.614623

Change log

Version 0c

1. 11/25/11, added the cable oxidization condition after anneal. Picture provided by D. Dietderich.
2. 11/3/11 – 11/15/11, sensitivity of multipole to Rc values at block and cable levels. Rc estimation based on the optimization.
3. 10/28/11, discussion on the measurement during the training quench added.
4. 10/28/11, contact resistance study.
5. 10/26/11 – 10/27/11, rise-and-decay issue. Multipoles plotted against the main field, as suggested by M. Marchevsky. Current profile of each rotation related to the multipole fluctuation included.
6. 10/26/11, 11:14 am, created from version 0b.

Version 0b

1. 10/2/11 – 10/7/11, H. Felice and P. Ferracin provided and explained the coil pole azimuthal strain data during the loading and warmup. Compared with the measured a3 and b3.
2. 9/23/11 – 10/3/11, averaged harmonics from the current of different polarities. Room-temperature measurement results before cooldown.
3. 9/21/11, 3:12 pm, inverse analysis on the non-allowed harmonics at 14 kA.
4. 9/20/11, 5:43 pm, inverse analysis on the allowed harmonics at 14 kA.
5. 9/19/11, 2:54 pm, corrected the sign of the odd skew harmonics of HQ01d 100 mm probe results (Table 32).
6. 9/16/11, added the harmonics sensitivity matrices for the allowed harmonics and non-allowed harmonics.

Version 0a: initial version.